In Situ Spectroscopy at Electrified Catalytic Interfaces: Understanding the Molecular Factors During CO_2 Reduction on Metal Electrodes

Vincent John Ovalle

A dissertation
submitted to the Faculty of
the Department of Chemistry
in partial fulfillment
of the requirements for the degree of
Doctor of Philosophy

Boston College
Morrissey College of Arts and Sciences
Graduate School
Advisor: Professor Matthias M. Waegele

December 2021

Copyright © 2022 by Vincent John Ovalle

In Situ Spectroscopy at Electrified Catalytic Interfaces: Understanding the Molecular Factors During CO_2 Reduction on Metal Electrodes

Vincent John Ovalle

Advisor: Matthias M. Waegele, Associate Professor of Chemistry

The electrocatalytic interface between a metal electrode and its electrolyte constitutes a complex reaction environment involving binding sites on the electrode surface and various molecular components on the liquid side of the interface. To add to the complexity, this environment can evolve during catalysis as a function of the applied potential, pH, supporting electrolyte identity and current density. Therefore, breaking down the impact of the individual components on the catalytic interface requires *in-situ* techniques. In this thesis, employing *in-situ* surface-enhanced infrared absorption spectroscopy (SEIRAS), we elucidated some of the molecular components of the electrocatalytic interface that influence CO_2 reduction. We applied this technique to study the reaction on polycrystalline Cu and Au electrodes. In the first part of this thesis, using surface-adsorbed CO, CO_{ads}, a reaction intermediate during the reduction of CO_2 to hydrocarbons, as a vibrational probe to study the evolution and speciation of the Cu electrode surface under alkaline pH conditions. We showed that the electrolyte pH and the applied potential drive irreversible reconstruction of the Cu surface to favor the binding of multiply bonded CO (CO_{bridge}). We found CO_{bridge} to be electrochemically inert. Instead, the singly bound CO_{atop} is the primary on-pathway CO intermediate for further reduction to hydrocarbons. In another study, we analyzed the vibrational band of the CO_{atop} intermediate to observe how the presence of molecular additives in the form of N-arylpyridinium-derived films impacts the selectivity for CO_2 reduction. We found that certain types of N-arylpyridinium-derived films block adsorption of CO_{atop} on undercoordinated Cu sites, thereby halting hydrocarbon formation.

Other N-arylpyridinium-derived films do not impact the CO_{atop} population, but provide a porous barrier between the electrode and electrolyte that increases the interfacial pH. We found that the increase in interfacial pH is likely responsible for the observed suppression of H_2 and CH_4 formation in comparison with the respective formation rates of these products on unmodified Cu electrodes. In Chapter 5 of this thesis, we investigated to what extent anions of the supporting electrolyte control the adsorption of CO_{atop}. This intermediate plays a central role in the mechanisms of CO_2 reduction. Under 1 M anion concentration, we found that specifically adsorbed Cl^- destabilizes CO binding through ligand effects. Hydrated SO_4^{2-} and ClO_4^- block a fraction of CO_{atop} sites. Under 10 mM anion concentration, the identity of the anion did not affect CO_{atop} adsorption. This study demonstrates that the identity and concentration of anions can affect CO_{atop} adsorption in complex ways. In the final part of this work, we focused on the effects of alkali metal cations on CO_2 reduction. We determined the surface concentration of alkali metal cations on Au electrodes (that is, the population of specifically adsorbed alkali metal cations). We probed the surface concentrations by using the CH_3 deformation band of the organic cation tetramethylammonium ($methyl_4N^+$) as a vibrational probe of the electrochemical double layer. We found that the concentration of the alkali cations at the electrode surface is dependent on the cation's free energy of hydration. The rate of CO_2-to-CO correlates with the measured surface concentration of the alkali metal cation. The ability of a cation to undergo partial dehydration therefore is a critical factor in the cationic promotion CO_2 reduction.

Contents

List of Figures

List of Tables

Acknowledgements

I would like to first thank my advisor during my time in graduate school, Prof. Matthias M. Waegele, and his financial support to allow me freedom to pursue many different scientific projects. Dr. Waegele's standards for scientific excellence are without exception of the highest quality. He instills these standards into his student's scientific pursuits and leads by example. Of the broad skills I have learned and developed in graduate school, the important ones that will stick with me throughout my professional career I owe to his tutelage. Whenever I felt demoralized or frustrated by research results, meeting with Matthias always provided encouragement and guidance through some great projects. He is a true role model as a scientist, father, and professor.

I would like to acknowledge my committee members, Prof. Dunwei Wang and Prof. Udayan Mohanty, for generously offering their time and energy. These professors have been the rock-solid foundation of our department. Their genuine curiosity in Chemistry and scientific rigor has always held my admiration. I want to thank and acknowledge Prof. Michael J. Janik from Pennsylvania State University, his post-doctoral student, Dr. Yawei Li, and his graduate student, Naveen Agrawal for providing unique theoretical insights, helpful discussion, and ultimately successful collaborations.

I have been fortunate to meet and interact with many amazing people at Boston College. Some of these moments have sadly ended far too soon. I feel lucky to have spent time hanging out at James Thorne's house and having the honor of presenting my research to Prof. Frank Tsung. You were both bright souls in our department and will be forever missed.

With the many countless hours spent the lab, it was always worthwhile because my lab mates felt like another family. Jingyi Li, Xiang, Li, and Charuni Gunathunge, who started the excellent science in the Waegele lab, are like my older siblings. They always persisted with a smile and are truly kind individuals. Paul Robert Hicks, whom I joined

the lab with and shared much merriment, is a true lifelong friend. I have always felt that our lab is a safe place to share both research ideas and feelings. I would like to also thank acknowledge the current and former members Yu-Shen Hsu, Honga Zhang, Sammi Wu, Kevin Ye, Julie Hong, and Jingchen Yang, who are all wonderful scientists and people.

This journey through graduate school would not have been possible without the love and support of my family. My five older siblings, Andre, Simone, Dominique, and Genevieve are such talented, motivated, and beautiful people that I constantly look up to. My parents, Mary Clare and Tomas, have always been there when I needed them and are a source of joy and unconditional love. Gerard and Sandy have been incredibly supportive, kind, and loving; I feel fortunate to have gotten to know them and call them my family. The friends I have made along the way made the last 5 years zoom by, and I am grateful for all the laughter and commiseration we have shared. Finally, I would like to acknowledge my partner, Sarah. Sarah has been the most understanding, encouraging, and loving partner I could ever wish for. She is truly an amazing person. With her at my side, I know we can get through anything.

Dedication

To my siblings, Andre, Simone, Dominique, and Genevieve, my parents Mary Clare and Tomas, and my partner Sarah.

Chapter 1

Introduction

1.1 Introduction

In 2019, 38 gigatons of CO_2 was emitted into the atmosphere in the consumption of fossil fuels [1]. According to the most recent report from the International Panel on Climate Change, in 2019, the amount of CO_2 in the atmosphere was at its highest point in the last 2 million years and the amount of N_2O and CH_4 were at their highest in the last 800,000 years [2]. With these alarming estimates, it is no debate that the global average temperature is rapidly rising due to greenhouse gas emissions from human civilization. Further, the fossil fuel resources that civilization relies on for chemical feedstocks and as an energy source exists in a finite quantity. Therefore, renewable energy sources and low-emission chemical feed stocks need to be rapidly implemented to keep pace with human energy demands and prevent a climate disaster of apocalyptic proportions: at current global emission rates, worst case-scenario estimates predict a 4.4° C increase in the global average temperature at the turn of the century [2]. As the amount of wind and solar energy sources increases to curb the consumption of fossil fuels and meet increased energy demands, technologies that can store or use the energy during peak production hours need to be developed. Further, the fossil fuel emissions from the production and use of petrochemical feedstocks in the chemical industry continues to grow as the world-wide demand increases [3]. These chal-

lenges need to be approached from a wide range of sectors with manifold technologies. A critical component to address these challenges will involve electrocatalysis. Electrocatalysis powered by renewable energy resources can provide a sustainable strategy to convert abundant small molecules like H_2O, N_2, and CO_2 into fuels for long-term energy storage and commodity chemical usage. This environmentally sustainable approach can be further translated to synthetic organic chemistry of larger molecules, providing even higher levels of regio- and chemoselectivity [4, 5]. These later stage electrochemical transformations have been successfully used on the industrial scale, such as in the production of the fragrant molecule lysmeral, which is produced through electrochemical oxidation on a $>$10,000 ton per year scale[6]. Further, electrochemistry has been implemented in the splitting of water to produce hydrogen [7, 8], the conversion of biomass to value-added products [9, 10] and the reduction of CO_2 [11–13]. Even with these successes, electrocatalytic conversions can still suffer from a myriad of issues, such as limited selectivity, high overpotentials, and catalyst deactivation [14–18]. With the promise of both mitigating greenhouse gas emissions and providing a carbon-neutral or carbon-negative source of fuels and feedstock chemicals, the aim of this work is to study the fundamentals of CO and CO_2 electrochemical reduction on prototypical Cu and Au electrodes to understand its mechanisms and ultimately optimize this process.

While the electrode material and morphology play a fundamental role in electrocatalysis, it is the entirety of the electrochemical double layer that ultimately drives the catalysis. The electrochemical double layer is a complex landscape that can be broken down into fundamental molecular components, each with multifaceted impacts on electrocatalytic reactions. As depicted in Figure 1.1, some of these key molecular components on the liquid side of the interface are adsorbed ions, interfacial water, and co-catalyst additives. These individual components can result in modulation of the electric field, blocking of surface sites, changes in reactive partners, interfacial pH buffering, proton donor effects,

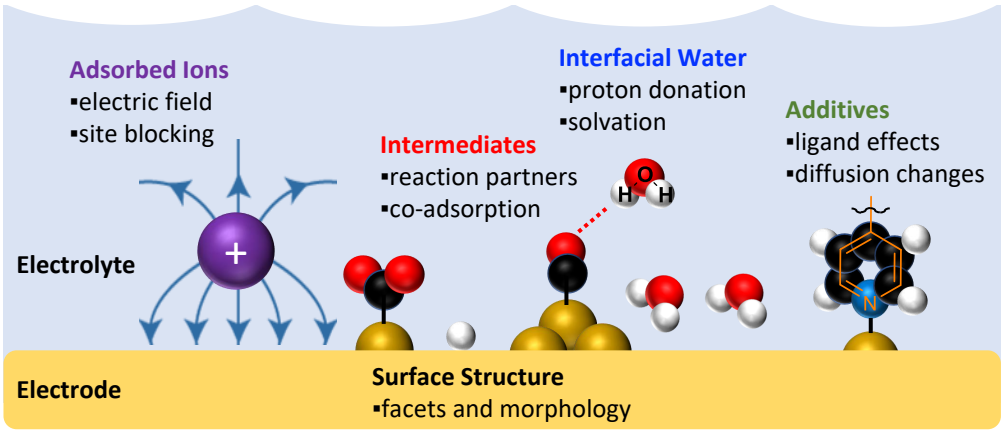

Figure 1.1: Depiction of the molecular components of the electrode/electrolyte interface, including the surface structure of the electrode, adsorbed ions, intermediates, interfacial water, and co-catalyst additives.

electronic structure changes of the electrode, and mass transport limitations to and from the surface [19–30]. Further, the electrochemical double layer is a dynamic environment and subject to evolve during catalysis [31–33]. Therefore, it is of great importance to understand how these components combine under *operando* conditions to form the complex active site. With this understanding, the active site can be tailored to optimize catalytic efficiency and product selectivity.

Understanding the electrocatalytic interface during the reduction of CO_2 and CO is a formidable challenge. Starting with the electrode side of the catalyst, the rate of reduction is highly dependent on the nature of the active site [34–37]. Even when employing a single-crystal Cu electrode that supposedly contains primarily one distinct surface facet, different surface preparations result in drastically different selectivity for CO_2 reduction to hydrocarbons [38]. With a polycrystalline or nanostructured electrode surface, many different surface facets coexist, making it extremely difficult to pinpoint the most catalytically active sites. This is further complicated by the dynamic nature of the electrode surface. For example, Cu can undergo reversible reconstruction that is a function of surface adsorbed

CO coverage and the applied potential [31]. As other irreversible changes can occur as a reaction proceeds, particularly with Cu surfaces [39–42], real-time characterization of the surface, detection of reaction intermediates, and product determination is crucial to optimize CO_2 reduction and better understand its complex mechanism.

A multitude of *in situ* techniques have been employed and developed to study the electrochemcial reduction of CO and CO_2 [43, 44]. For probing the catalyst structure during catalysis, *in situ* X-ray techniques, including X-ray Diffraction (XRD) [45], X-ray Photoelectron Spectroscopy (XPS) [46], and X-Ray Absorption Spectroscopy (XAS) [47], have become powerful tools. While these techniques can provide vital catalyst structure information, they can be very challenging to interface with electrochemical cells and use expensive X-ray sources. Direct imaging techniques like electrochemical scanning tunneling microscopy may offer a way to probe both the surface structure and detect adsorbed intermediates [48], however its application is limited by disturbances from the large currents that are associated with CO_2 reduction. Alternatively, vibrational spectroscopic methods such as Fourier Transform Infrared (FTIR) and Raman spectroscopy can simultaneously provide structural information of the catalyst, detection of critical intermediates, and molecular structure of the electric double layer under real CO_2 reduction conditions [49]. However, under real reaction conditions, the detection of surface intermediates and species of interest in the electric double is still challenging: they are often only present in sub-monolayer quantities or obfuscated by the bulk electrolyte. Surface enhanced infrared (IR) absorption spectroscopy (SEIRAS) in the attenuated total internal reflection configuration (ATR) provides a convenient and powerful method to overcome these issues [50].

SEIRAS is fundamentally a surface sensitive technique. In order to successfully carry out SEIRAS, a nanoscopically rough metal film is deposited onto an ATR crystal. The nanoscopic roughness results in a wide plasmonic resonance in the mid-infrared spec-

trum. This gives rise to an enhancement in the infrared absorption signals within 5 nm of the surface [51], allowing the detection of sub-monolayer quantities of surface adsorbed species. Coupled with the surface selection rule, only molecular vibrations with dipole changes normal to the surface result in absorption, reducing strong absorption from the randomly ordered bulk electrolyte solution [52]. To fully take advantage of this technique, the species of interest need to be vibrationally active. For CO_2 and CO reduction on Cu electrodes, the principal intermediate for all hydrocarbon products, surface adsorbed CO (CO_{ads}), is a powerful vibrational probe [50]. As a vibrational probe, the C≡O stretch frequency of CO_{ads} provides insight into the local reaction environment of the electrochemical double layer: it is sensitive to the coordination to the metal surface, the relative CO population, local electric fields, and the presence of co-adsorbates [50]. As an on-pathway intermediate for CO_2 and CO oxidation, the information gleaned from a SEIRAS analysis of CO_{ads} is extremely valuable. To have a complete understanding of the electrochemical interface, intermediate detection is just one part of the overall picture. Beyond surface adsorbed intermediates, evidence for how cations and anions impact CO_2 reduction has been severely lacking. It has been demonstrated that both the choice of cations and anions can play a significant role in tuning the rate and selectivity of CO_2 reduction [53–55]. The analysis of cations and anions in the electrochemical double layer during CO_2 reduction is challenging for many *in situ* techinques, including SEIRAS. This is fundamentally due to the choice of cations and anions that modulate CO_2 reduction: much of this research has employed IR-inactive alkali metal cations or halide anions [55–61]. The work in this thesis challenges these hurdles by taking novel approaches in the analysis of vibrational modes in the hydration shell of anions, IR-active organic additives, and the use of an IR-active organic cation in the presence of alkali metal cations.

While prior work from our team has contributed significantly to the understanding of the catalyst structure and morphological dynamics during CO_2 and CO reduction with

SEIRAS [31, 62], this thesis focuses on using CO_{ads} and novel vibrational probes to understand molecular factors on the liquid side of the electrified interface. However, this does not preclude the impact that the liquid side has on altering the catalyst structure under reaction conditions, as will be demonstrated in this thesis. The discussion will be broken down into four main components: pH dependent surface dynamics of key intermediates, the influence of additives on intermediates, the impact of anions on intermediates, and determining the distribution of metal cations at the interface.

After a brief introduction into some of the theoretical concepts relevant to this thesis in Chapter 2, we will investigate Cu electrodes in alkaline electrolytes. In Chapter 3 of the thesis, this discussion will focus on the principal intermediate for the reduction of CO_2 and CO to hydrocarbons on Cu electrodes, CO_{ads}. It has been demonstrated that electrolytes with basic pH [22, 63, 64] favor the formation of valuable hydrocarbons and oxygenates. Therefore, identifying the adsorption configuration of CO_{ads} under alkaline pH conditions can allow us to identify the on-pathway reduction routes to these valuable products and provide a set of guidelines for the theoretical treatment of CO adsorption. Using SEIRAS, we are able to control the applied electrode potential and observe the resulting dynamics of CO_{ads} as a function of pH, time, and potential. We observe that under alkaline pH conditions (pH = 11.5) in CO saturated 0.05 M Li_2CO_3 during cathodic polarization of the electrode, there appears to be two distinct sub-populations of CO_{ads}: CO_{atop} with a C≡O stretch frequency in the 2000-2100 cm^{-1} range and CO_{bridge} with a C≡O stretch frequency in the 1800-1900 cm^{-1}. Besides the shift in C≡O stretch frequency, the CO_{ads} populations have different dynamics. The CO_{atop} appears to adsorb/desorb reversibly with the applied potential, while a significant hysteresis in adsorption is present with CO_{bridge}. In the anodic reverse scan of a cyclic voltammogram, the applied potential of the electrode must oxidize the Cu surface before CO_{bridge} can be liberated. Interestingly, we observe that under prolonged cathodic polarization (tens of minutes) and further increase in elec-

trolyte alkalinity (pH = 13), the CO_{bridge} population continues to grow. We demonstrate that when the total CO coverage drops below saturation, CO_{atop} can convert to CO_{bridge}. To probe the relative reactivity of the CO_{atop}, we stepped the potential to a reactive potential of -1.75 V vs SHE. Under these conditions, only CO_{atop} reacts away from the surface while CO_{bridge} remains. We determined that the accumulation of this spectator CO_{bridge} species is likely the result of reconstruction of the polycrystalline Cu surface to predominately Cu(111) or Cu(100) facets during a combination of alkaline and prolonged cathodic polarization conditions. This work demonstrates that we can track the dynamics of surface intermediates that are on-pathway with CO_{atop} and use CO_{bridge} as a probe of the local pH and pH-driven alteration of the electrode surface structure with catalysis. The differing reactivity of CO_{atop} and CO_{bridge} serves as a cautionary reminder that computational and micro-kinetic modelling needs to specify the adsorption configuration of CO to accurately describe catalytic interfaces.

While the electrolyte pH has been used as a tool to alter the reactivity of CO_2 reduction, an alternative route is adding a molecular cocatalyst [44, 65–68]. It was recently demonstrated that by adding derivatives of N-substituted arylpyridinium compounds, the selectivity of CO_2 reduction can be significantly modulated [69]. Compared to the bare Cu electrode surface, when 1-(4-tolyl)pyridinium (T-pyr) was added to the electrolyte, the Faradaic efficiency for $C_{\geq 2}$ products increased from $\approx 25\%$ to $\approx 80\%$, while the addition of 1-(4-pyridyl)pyridinium (P-Pyr) prevented any $C_{\geq 2}$ products. Prior work determined that the arylpyridinium additives would deposit on the surface to form an organic film, but the mechanisms for how the film regulated the reaction selectivity was not understood. In Chapter 4, we demonstrate how the presence of T-Pyr does not significantly impact the population of CO_{ads}, but impedes the mass transport of OH^- from the interface resulting in a locally alkaline pH. This is evident by the accumulation of solution phase carbonate observed in IR spectra in the presence of T-Pyr, which can be simulated on

the bare Cu electrode by stopping convection of the electrolyte. Increasing the local pH at the Cu/electrolyte interface has been demonstrated to lower the rates of hydrogen and methane formation, therefore boosting the selectivity towards $C_{\geq 2}$ hydrocarbon products. P-pyr alternatively does impact the CO_{ads} population. The CO_{atop} band is normally comprised of a lower frequency component corresponding to CO adsorbed on terrace sites and a higher frequency component assigned to CO adsorbed on comparatively lower coordinated or defect sites. In the presence of P-pyr, the high frequency band, or CO adsorbed on defect sites, is completely missing. By using the molecular additive pyridine, which has the analogous pyridyl functional group but does not form an organic film, we demonstrate that CO_{atop} adsorbed on defect sites can be displaced as the concentration of pyridine is increased in the bulk solution. This supports two key conclusions: that the pyridyl functional group poisons undercoordinated Cu sites, and that these sites are crucial to reduce CO_{ads} to $C_{\geq 2}$ hydrocarbons. We demonstrated that seemingly similar additives can have drastically different impacts at the electrified liquid interface, and *in situ* techniques are necessary to identify the underlying mechanisms.

This thesis will demonstrate that CO_{ads} is a powerful probe of the pH environment, the electrode structure, and changes in the on-pathway population with the addition of molecular additives. Beyond this, we want to understand what are the fundamental driving forces for CO adsorption on metal electrodes. On Au electrodes, it has been shown that CO adsorption occurs at applied potentials near the potential of zero charge (PZC), significantly more positive than where CO_2 reduction takes place [70]. On Cu electrodes however, CO adsorption occurs at more negative potentials of the PZC, which probably contributes to the overpotentials to drive further reduction of CO_{ads}. It has been previously suggested that the desorption of specifically adsorbed anions drives the potential dependence of CO adsorption. However, the systematic study of anion identity and concentration dependence has yet to be carried out on Cu electrodes. To bridge this gap in understanding, we show

in Chapter 5 CO adsorption studies on Cu electrodes in the presence of three anions with increasing affinity for the Cu surface (ClO_4^-, SO_4^-, Cl^-) at two extremes of concentration (10 mM and 1 M). While these anions are either IR-inactive or have observable modes out of the IR-window of study, under 1 M concentrations, we can observe their relative population with the change in their respective hydration shell band and the resulting impact on the C≡O stretch band as a function of applied potential. Under low anions concentrations, we show that there is virtually no difference in the CO adsorption curve of CO_{atop}. At high anion concentrations, the CO_{atop} saturation is generally lower; however, the magnitude and mechanisms by which anions modulate CO adsorption are anion dependent. Weakly and non-adsorbing anions (ClO_4^- and SO_4^-) counter intuitively block a fraction of the CO adsorption sites. This blocking is dependent on the CO coverage, which can originate from reversible reconstruction of the Cu with CO adsorption. The specifically adsorbing Cl^- anion lowers the CO coverage by altering the CO adsorption energy, as evidenced by the large C≡O stretch frequency shift and the independence of the adsorption on CO coverage. This work demonstrates that anions can have an unexpected influence on surface intermediates: specific adsorption is not necessary for site blocking, and adsorbed anions can exist on Cu even at relatively cathodic potentials. Ultimately, the adsorption onset potential of CO on Cu is relatively unchanged by anion identity, necessitating alternative methods than altering the anion identity in order to modulate the overpotential of adsorption.

While the relative population of anions in the electrochemical double layer can indirectly be be observed with SEIRAS, determining the distribution of metal cations is an even greater challenge. The choice of cation used during electrocatalytic transformations can drastically impact the energetic landscape at the electrode/electrolyte interface [23]. The mechanisms for how cations influence the electrochemical double layer during reactions is still a matter of debate. The mechanisms that have been proposed include electro-

static and/or chemical interactions with intermediates, [71–74], interfacial water restructuring [25], site-blocking, [75, 76], and interfacial pH modulation [77–79]. To understand the effects of cations and properly leverage their influence on electrocatalytic processes, it is critical to illuminate the potential-dependent distribution of cations in the electrochemical double layer. This is particularly true for the reduction of CO_2 on metal electrodes.

It has been demonstrated that on Ag, Cu and Au electrodes in 1 mM H_2SO_4, CO_2-to-CO conversion only takes place when metal cations are added to the electrolyte [56]. Further, the identity of the metal cation can control the rates and tune the product selectivity during the reduction of CO_2 [56, 74, 80–82]. However, these studies have been limited in determining the distribution of the alkali metal cations in the electrochemical double layer. In Chapter 6, we show that the CH_3 vibrational mode of methyl$_4$N$^+$ is a novel probe of cations in the electrode/electrolyte interface under catalytically relevant CO_2-to-CO reduction conditions on Au electrodes. We show that there are two distinct sub-populations of methyl$_4$N$^+$: surface adsorbed methyl$_4$N$^+$ (methyl$_4$N$^+_{\mathrm{ads}}$) and bulk-like methyl$_4$N$^+$. In a mixture of methyl$_4$N$^+$ and K$^+$, K$^+$ is able to displace methyl$_4$N$^+_{\mathrm{ads}}$ as the potential is tuned negatively. Product detection studies on a roughened Au electrode allow us to linearly correlate the displacement of methyl$_4$N$^+_{\mathrm{ads}}$ by K$^+$ to the rate of CO production. This method is extended to smaller and larger alkali cations (Li$^+$ and Cs$^+$ respectively). It is observed that the magnitude of displacement by each metal cation correlates to the hydration energies of the cations in the order of Li$^+$<K$^+$<Cs$^+$. This is further corroborated by product detection studies demonstrating the increasing rate of CO_2-to-CO with increasing cation size in accordance to their free energies of hydration. This is the first spectroscopic evidence supporting the key role of cation hydration in the surface concentration of alkali cations in the double layer.

The efforts presented in this thesis validate the efficacy of *in situ* SEIRAS in breaking down the complexities of the electrochemcial double layer to their core components during

a sophisticated reaction like CO_2 reduction. The knowledge developed from this work is expected to improve the development of electrocatalysts for the reduction of CO_2 and optimize the liquid side of the electrode/electrolyte interface. The final chapter of this thesis (Chapter 7) will provide a summary and outlook of this field, discussing limitations of the techniques provided, improvements to the experimental setup, and applications of the methods developed herein to future work.

Chapter 2

Theory

2.1 The Electrochemical Double Layer

Electrochemistry occurs at the interface between a charged electronic conductor (the electrode) and an ionic conductor (electrolyte) [83]. In this thesis, we will limit this to the study of metal electrodes immersed into aqueous electrolyte. During electrochemical reactions, an understanding of the molecular makeup of the electrode/electrolyte interface starts with modeling how the liquid and metal sides interact. The ordering of this structure is known as the 'electrochemical double layer', with a drop in potential leading from the metal surface into the electrolyte. This concept was first realized in 1853 by Hermann von Helmholtz, who discovered that when a charged electrode is immersed into an electrolyte, ions of like charge were repelled by the metal while counter ions were attracted to the surface [84]. While this initial model may oversimplify the electrode/electrolyte interface, it provided foundations for how the electric double layer can be described and impact the arrangement of cations, anions, and interfacial water during electrocatalysis.

In this section, we will briefly present some of the classic theories to describe the electrochemical double layer. Albeit somewhat primitive, the predictions of these models can successfully reproduce gross experimental features of real electrochemical systems.

2.1.1 Helmholtz Model

In the most basic model used to describe the electrode/electrolyte interface, the electrode is assumed to be perfectly polarized and the electrolyte treated as a continuum dielectric medium. In the model proposed by Helmholtz, the charged electrode is immersed into the electrolyte and the charges at the surface are screened by the counter ions in the electrolyte [85]. The counter ions at the electrode surface make up the Helmholtz plane and are separated by a molecular radius (Figure 2.1A). These compact layers were initially treated as hydrated ions that are electrostatically adsorbed at the surface, and later in an updated model treated as specifically adsorbed. In these two scenarios, the position of the compact layers are respectively referred to as the outer and inner Helmholtz planes of the Helmholtz layer. With either treatment, the surface of the electrode and Helmholtz plane resemble the sheets of a parallel plate capacitor. As such, the double layer can be modeled with a differential capacitance:

$$\mathrm{C_d} = \frac{\epsilon\epsilon_0}{\mathrm{d}} \tag{2.1}$$

where d is the distance between the two layers, ϵ represents the dielectric constant of the medium, and ϵ_0 is the permittivity of free space [83]. From this equation, the differential capacitance is regarded as a constant regardless of the applied potential. In a real electrochemical system, this tends to break down as the C_d is found to depend on both the applied potential and solution species concentration [86].

2.1.2 Gouy-Chapman Model

To rectify the limitations of the Helmholtz model, the solution side of the interface needs to be treated differently. With an electrode, the charge is confined to its surface. The same

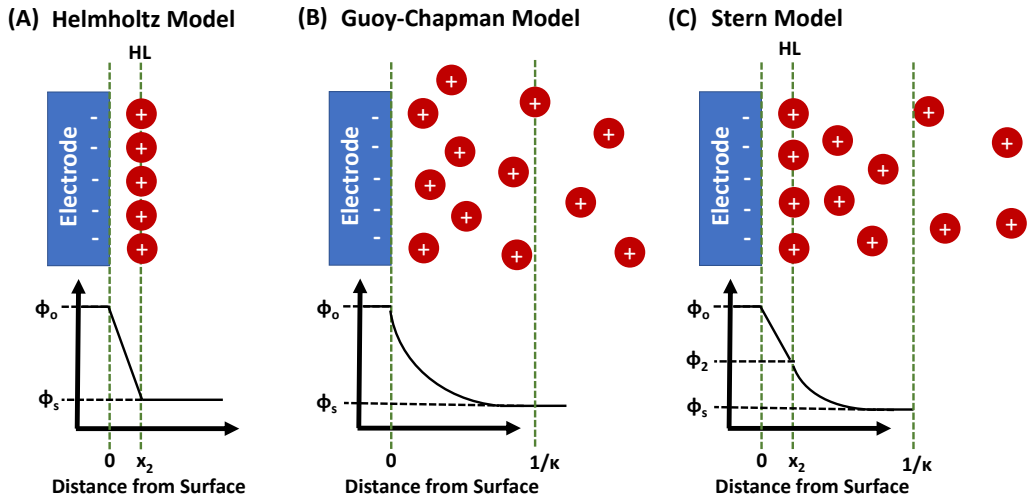

Figure 2.1: Depiction of the electrochemical double layer with a negatively charged electrode surface/electrolyte interface and the corresponding potential drop according to the (A) Helmholtz, (B) Gouy-Chapman, and (C) Stern double layer models.

is not necessarily so for the solution side of the interface. In particular, at low concentrations of supporting electrolyte, the liquid phase contains a relatively small density of charge carriers. Therefore, it may take a significant thickness of electrolyte solution in order to balance the charge on the electrode surface. This brought about the idea of a diffuse electrolyte layer, independently proposed by Louis Georges Gouy in 1910 [87] and David Leonard Chapman in 1913[88]. The statistical mechanical treatment of the electrolyte layer allows both the concentration and potential dependence to be added to the potential drop and differential capacitance, now known as the Gouy-Chapman model. Here, the width of the diffuse layer is represented by the Debye screening length (Figure 2.1B): $1/\kappa = 1/\sqrt{2F^2z^2C_0/(\epsilon RT)}$, where C_0 is the molar concentration of a mono-valent electrolyte [83]. This leads to the differential capacitance determined to be as follows:

$$\mathrm{C_d} = \mathrm{zF} \times \sqrt{\frac{\epsilon \mathrm{C_0}}{2\pi \mathrm{RT}}} \times \cosh(\frac{\mathrm{zF}}{2\mathrm{RT}}\zeta) \tag{2.2}$$

where z represents the ion valency, F is Faraday's constant, ϵ is the dielectric constant,

C_0 is the concentration of the electrolyte, R is the gas constant, and ζ is the zeta potential. This model is successful in determining the double layer capacitance near the potential of zero charge (PZC) for very dilute electrolyte solutions. However, the value of the predicted capacitance is overestimated at higher electrolyte concentrations and potentials further away from the PZC.

2.1.3 Stern Model

To solve both of the issues inherent to the Helmoltz and Gouy-Chapman models, Otto Stern introduced into the Gouy Chapman model the idea that the electrolyte ions have a finite size, and therefore are limited by their ionic radii in their approach to the electrode surface. This essentially combines the compact layer of the Helmholtz model with the diffuse layer of the Gouy-Chapman model. Overall, this results in the capacitance of the interface being represented by the Helmoholtz and Gouy-Chapman capacitances in series (C_H and C_{GC}) [83]:

$$\frac{1}{\mathrm{C_d}} = \frac{1}{\mathrm{C_H}} + \frac{1}{\mathrm{C_{GC}}} \tag{2.3}$$

This model is known as the Stern or Gouy-Chapman-Stern (GCS) model. When the electrolyte concentration is large or even the applied electrode potential is large in dilute solutions, the counter ions are located very near the electrode surface and resemble the Helmholtz model. This results in the capacitance of the diffuse layer (C_{GC}) becoming so large that the overall capacitance is dominated by the compact layer (C_H). While there are still some discrepancies, the Stern model is able to predict gross features in real electrochemical systems.

2.2 Fourier Transform Infrared Spectroscopy at Electrified Interfaces

Conventional electroanalytical methods can provide extensive amounts of mechanistic and kinetic information regarding charge-transfer processes at an electrocatalytic interface. However, these techniques probe the bulk electrode/electrolyte properties and can be limited in discerning the interfacial molecular structure. The molecular understanding of the interface is critical to improving the rates and desirable selectivities during electrochemical processes. Traditional electrochemical methods are particularly limited in discerning electrode processes that involve multiple proton/electron transfers to adsorbed intermediates. In order to probe the molecular components of an electrochemical interface, surface sensitive *in situ* techniques need to be employed in addition to traditional electrochemical methods. One of the techniques that can achieve this is based on infrared (IR) absorption spectroscopy.

IR absorption spectroscopy is one of the most powerful and important spectroscopic techniques for the structural elucidation of chemical compounds. This technique relies on the interaction of infrared electromagnetic radiation with vibrational modes of matter resulting in absorption of the radiation. The frequency of absorbed radiation is dependent on the characteristics of the chemical structure, which in turn is influenced by its surrounding environment. This makes IR spectroscopy particularly powerful in identifying molecular structures and reaction environments at an electrochemical interface. In this section, we will outline some of the key theories for IR spectroscopy and how the technique is applied to study electrode surfaces.

2.2.1 Selections Rules for IR Absorption

In order for a molecule to interact with an electromagnetic field and absorb a photon of a particular frequency ν, it must have a dipole that oscillates at that frequency. This can be expressed quantum mechanically in terms of the transition dipole moment, μ_{01}, between two states ψ_0 and ψ_1:

$$\mu_{\mathrm{fi}} \;=\; \int \psi_1^{*}\, \hat{\mu}\psi_0 \,\mathrm{d}\tau \tag{2.4}$$

where $\hat{\mu}$ is the dipole moment operator. The integral represents the propagator and therefore the probability of the transition between the states. Only if the transition dipole moment is nonzero will it contribute to the spectrum. When applied to the vibration of a diatomic molecule, we can express the transition dipole moment in terms of the bond length *r* between the atoms:

$$\mu_{01} \;=\; \int \psi_{1,\mathrm{vib}}^{*}\, \mu(\mathrm{r})\psi_{0,\mathrm{vib}} \,\mathrm{dr} \tag{2.5}$$

The dipole moment is a function of the displacement $x = r - r_e$ from an equilibrium bond length r_e. The dependence of the dipole on its displacement from its equilibrium position can be expressed through a Taylor expansion of the equilibrium dipole moment:

$$\mu \;=\; \mu_{\mathrm{e}} \;+\; \frac{\mathrm{d}\mu}{\mathrm{dr}}|_{\mathrm{r_e}}\,(\mathrm{r}-\mathrm{r_e}) +, \frac{1}{2}\frac{\mathrm{d}^2\mu}{\mathrm{dr}^2}|_{\mathrm{r_e}}(\mathrm{r}-\mathrm{r_e})^2 \;+\; ... \tag{2.6}$$

By combining equations 2.5 and 2.6 and omitting the latter terms after the linear term, we get:

$$\mu_{01} \;=\; \mu_{\mathrm{e}} \int \psi_{1,\mathrm{vib}}^{*}\, \psi_{0,\mathrm{vib}} \,\mathrm{d}\tau \;+\; \frac{\mathrm{d}\mu}{\mathrm{dr}}|_{\mathrm{r_e}} \int \psi_{1,\mathrm{vib}}^{*}\, (\mathrm{r}-\mathrm{r_e})\psi_{0,\mathrm{vib}} \,\mathrm{d}\tau \tag{2.7}$$

As the first term in 2.7 equals zero because the vibrational wavefunctions of the same electronic state are orthogonal to each other, we are left with only the second term. Therefore, the intensity of a vibrational transition is proportional to the square of the change in the dipole moment with bond distance, expressed by:

$$\mathrm{I} \propto \mu_{01}^2 \propto \frac{\mathrm{d}^2\mu}{\mathrm{dr}^2}|_{\mathrm{r_e}}^2 \tag{2.8}$$

It follows that there must be a change in the dipole moment with a change in bond length for a vibrational transition to absorb infrared light.

2.2.2 Attenuated Total Reflection Surface Enhanced IR Absorption Spectroscopy (ATR-SEIRAS)

In the early applications of IR spectroscopy to study metal electrode/electrolyte interfaces, one of the primary methods employed was IR reflection-absorption spectroscopy (IR-RAS). This technique has been used extensively on many single crystal and polycrystalline electrode surfaces [89]. Even so, it has some inherent limitations that arise from the experimental cell geometry. One of the biggest issues arises from the need to reflect the IR beam off of the metal surface: to reach the metal surface, the IR beam needs to travel through the bulk electrolyte. In aqueous electrolyte, water and potentially other species will absorb a significant proportion of the incoming IR radiation, increasing the interference from the bulk and lowering the signal intensity for species adsorbed on or near the electrode surface. Figure 2.2A [90] shows a typical experimental cell geometry for how this is achieved and the bulk-interference minimized for an IR-RAS experiment. In this setup, an IR transparent prism is pressed up against the cathode compartment, with an electrolyte layer of $1 - 10$ μM between the prism and the working electrode. The thin electrolyte layer lowers the IR absorption from the bulk as much as possible. However,

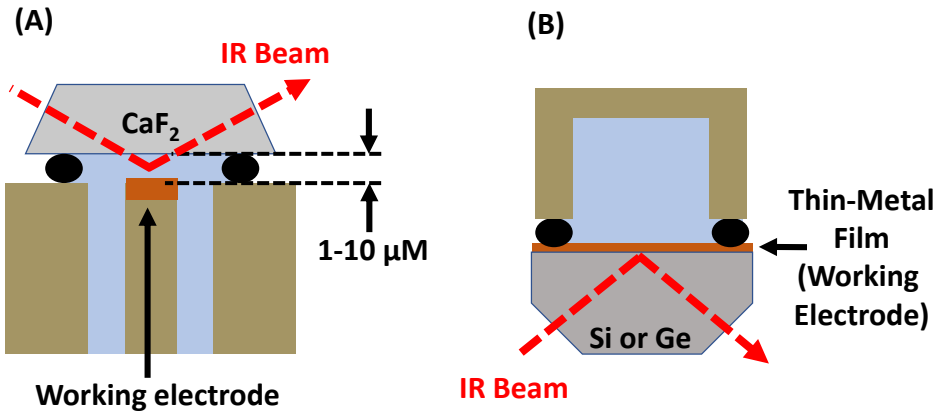

Figure 2.2: Depiction of the (A) traditional IR-RAS cell geometry and the (B) SEIRAS cell geometry in the ATR configuration. Adapted with permission from Ref [90]. Copyright 2006 WILEY-VCH Verlag GmbH & Co. KGaA, Weinheim.

thinning the electrolyte too much has further consequences. The first is that reactants in this layer may be depleted rapidly leading to mass transport limitations. The second is an increase in the solution resistance. While in cases where the reaction rates are low, the applied potentials are modest, and the time scales are slow, these effects may be able to be ignored. However, during reaction conditions like CO_2 reduction on Cu or Au where significant current densities can occur, or where a quick reaction response is needed, the IR-RAS cell geometry is limited.

To overcome this, the IR spectroelectrochemical cell is set up in an attenuated total reflection (ATR) configuration. Figure 2.2B [90] shows a typical ATR configured cell geometry, where a thin-metal film working electrode is layered onto an IR transparent prism, with the thin-film blanketed by the electrolyte. IR light is transmitted through a Si or Ge prism and totally reflected off of the back of the electrode. Under total internal reflection of the IR beam, to satisfy the condition that the tangential components of the electric and magnetic fields be continuous across the boundary, a powerless transmitted field called the evanescent wave emerges [91]. The evanescent wave propagates through the film parallel to the interface decaying exponentially into the medium, here the electrode/electrolyte.

The evanescent wave can interact with IR active species at the electrode surface, absorbing the light and attenuating the beam intensity, ergo the name 'attenuated internal reflection' (ATR). When the ATR configuration is coupled with a nanoscopically roughened electrode surface, the signal adsorption by molecules at the electrode surface can be one to three orders of magnitude larger. This resulting effect is known as surface-enhanced IR absorption spectroscopy (SEIRAS), and the effect is localized to a distance of only a few monolayers from the surface [90]. This ultimately results in comparable signals for the surface species and the bulk solution, allowing the cancellation of the latter much more easily than with IR-RAS, where the solution component of the spectra is dominant. Further, the electrolyte solution resistance can be kept low and have free mass transport, allowing measurement under large current densities with a quick measurement time.

Since it's discovery in 1980 by Hartsein et al.[92], SEIRAS has been a powerful technique to probe surface reactions at electrochemical interfaces. It has been applied to study electrochemical processes on a broad range of metal thin films, including but not limited to Rh, Ru, Pd, Pt, Sn, Cu, Ag, and Au [93–98]. The breadth of different metals that can maintain the SEIRA effect has made this technique indispensable.

The SEIRA effect that this spectroscopic method relies on is similar to the prominently used surface-enhanced Raman scattering (SERS). The basis for the surface-enhancement is generally considered to result from two distinct mechanisms, an electromagnetic and a chemical mechanism. Representing the infrared absorption as A, we can write[99]:

$$A \propto \mid \partial\mu/\partial Q \cdot E \mid^2 = \mid \partial\mu/\partial Q \mid^2 \mid E \mid^2 cos^2\theta \tag{2.9}$$

where $\partial\mu/\partial Q$ is the derivative of the dipole moment with respect to normal coordinate Q, E is the electric field exciting the molecule, and θ is the angle between $\partial\mu/\partial Q$ and E. In distinguishing the two mechanisms, the electromagnetic is a result of an increase

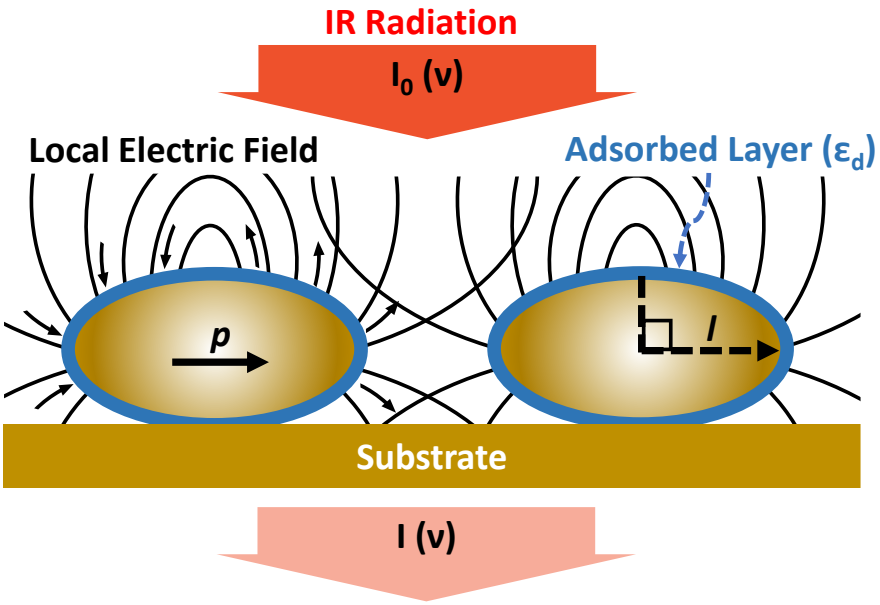

Figure 2.3: Depiction of the electromagnetic mechanism on an island metal film, where the incident photon field polarizes the metal particles to form the dipole p, exciting the (blue) adsorbed molecules. The electric field is represented by the curves and arrows. Adapted by permission from Springer Nature [99]: Springer-Verlag Berlin Heidelberg, Surface-Enhanced Infrared Absorption by Masatoshi Osawa Copyright 2001.

in $|\mathrm{E}|^2$ while the chemical is largely based upon an increase in the absorption coefficient, $|\,\partial\mu/\partial\mathrm{Q}|^2$.

The most common SEIRAS experimental setups rely on a chemically deposited or vacuum-evaporated metal thin film. These thin films are generally made up of metal islands and it is these metal islands that result in the SEIRA effect. Specifically, it is the nanostructure of these metal islands that gives rise to the electromagnetic mechanism for the signal enhancement. Shown in Figure 2.3, the metal islands are modeled as ellipsoids. The incident photon field of the IR light polarizes the metal islands through the excitation of localized plasmon modes. This induced dipole p on the island generates a local electromagnetic field that is stronger than the incident photon field that surrounds the island. The magnitude of the induced dipole moment p generated by the incident electric field (E) can

be represented as [51]:

$$p = \alpha V E \tag{2.10}$$

where α is the polarizability and *V* is the volume of the metal island. This dipole in turn induces a local electric field (lines in Figure 2.3) where the molecules adsorbed on the surface of the metal islands can be excited. The magnitude of this field is generally larger than the incident electric field, leading to an increase in the $\mid E \mid^2$ term of equation 2.9, enhancing the IR Absorption (A in equation 2.9). The magnitude of this local electric field can be represented as [51]:

$$\mid E_{local} \mid^2 = 4p^2/l^6 \tag{2.11}$$

with *l* being the distance from the center of the metal island. This relationship between $\mid E_{local} \mid^2$ and *l* explains the rapid decay in the signal with distance away from the electrode surface. This restricts the SEIRA effect to primarily adsorbed layers within a few monolayers of the interface, preventing large contributions from the bulk electrolyte.

The chemical mechanism for explaining the SEIRA effect arises from the observation that chemisorbed species on the metal surface tend to have a larger enhancement than physisorbed species. As mentioned previously, the chemical effect assumes that the $\mid \partial\mu/\partial \mathrm{Q} \mid^2$ from equation 2.9 increases in magnitude. This can result from charge oscillations between the metal surface and the metal surface enlarging the absorption coefficients [100, 101].

2.3 Chemisorption of CO on Transition Metal Surfaces

CO adsorption on transition metal surfaces is a touchstone of characterizing metal surfaces and has been studied extensively [102, 103]. A deep understanding of the adsorption of CO on metals has allowed the spectroscopic study of such phenomenon to become a powerful too in studying catalytic processes at electrode/electrolyte interfaces [50].

A classic interpretation of the CO transition metal bond is based on the Blyholder model. The Blyholder model explains this bond in terms of frontier molecular orbitals, as a combination of the charge transfer from the filled 5 σ orbital of CO to empty metal orbitals and the charge transfer from the filled metal orbitals to the empty $2\pi^*$ orbital of CO [102]. Based on this model, the chemisorption energy is predicted to increase with the coordination number of the CO molecule. This is due to the increase in the charge transfer from the filled metal orbitals to the empty $2\pi^*$ orbital of CO, referred to as π-backdonation. In this way, for a given metal surface, CO adsorbed on an atop site (CO_{atop}) has a lower chemisorption energy than CO adsorbed on a bridge site (CO_{bridge}). In its most basic application to IR spectroscopy, the increase in π-backdonation to CO lengthens the average CO bond length, red-shifting the frequency of absorbed IR radiation.

More sophisticated models have since been developed. Using *ab initio* calculations, Hammer, Morikawa and Nørskov (HMN) have presented a new model that describes the bonding of CO with transition metals by determining the interaction between the density of states (DOS) of the CO molecular orbitals and the DOS of the transition metals [104]. In this model, as the CO approaches the metal surace, the 5 σ and $2\pi^*$ frontier molecular orbitals renormalize through the interaction with the *sp*-states of the metal and hybridize with the *d*-states of the metal, splitting into bonding and anti-bonding orbitals. For late translation metals, the $2\pi^* - d$ hybridization determines the degree of *d* contribution to the CO metal bond. This is because the 5 $\sigma - d$ contribution is generally small as both

the bonding and antibonding orbitals from this hybridization are below the Fermi level, while the $2\pi^* - d$ hybridization results in a bonding orbital below the Fermi level and an anti-bonding orbital that is partially unoccupied. The $2\pi^* - d$ interaction becomes stronger as the energy gap narrows between the center of the metal's d-band and the $2\pi^*$ orbital of CO. The trend of energy gap narrowing follows the decreasing coordination number of the metal surface atom and metal identity from right to left for a given row on the periodic table. It was found that these trends correlate with the CO binding strength to a transition metal surface.

Chapter 3

Understanding Key Intermediates during CO Reduction: Identifying an Electrochemically Inert Population of CO on Cu electrodes under Alkaline pH

3.1 Introduction

Cu is the only pure metal that is able to electrochemically reduce CO_2 to $C_{\geq 2}$ hydrocarbons at significant rates [36, 63, 64, 68, 77, 105–119]. In this capacity, Cu can be employed as an electrocatalyst to provide value-added hydrocarbons from CO_2 and disrupt the use of fossil fuels in both commodity chemical synthesis and energy consumption. However, Cu suffers from a number of drawbacks, namely high over-potentials and low selectivities [63, 105, 120, 121]. The parasitic side reaction of hydrogen evolution is particularly challenging to mitigate during CO_2 reduction. A general strategy to suppress hydrogen evolution is to carry out the CO_2 reduction reaction under alkaline conditions. Under alkaline (0.1 M OH^-) to extremely alkaline (10 M OH^-) conditions, Faradaic efficiencies of $>$60% have been achieved for the multicarbon product ethylene with current densities up to $>$1 Acm^2[13, 111, 115, 117, 119]. Understanding the impact of alkaline conditions on the mechanism of CO_2 and CO reduction is therefore of great importance to determining the key components that boost the selectivity towards ethylene on Cu electrodes.

Through numerous experimental and theoretical studies, the rate- and potential-limiting step of CO_2 reduction to value added hydrocarbons such as ethylene has been identified as the reduction of surface-adsorbed CO.[35, 105, 122–127] Thus, understanding the surface dynamics of surface-adsorbed CO under reaction conditions is crucial to optimizing the formation of hydrocarbons. A number of theoretical studies using Density Functional Theory (DFT) have been carried out to understand the adsorption and further reduction of CO on Cu [35, 128–130]. However, these studies have used a variety of CO adsorption configurations, often omitting the vibrational frequency of CO, resulting in confusion as to what is the true binding mode of CO under reaction conditions. In these models, CO can be adsorbed on atop sites, two-fold bridge, three-fold bridge, and four-fold bridge sites. For a variety of electrocatalytic processes involving adsorbed CO, experimental studies have shown that differently coordinated CO on the surface can exhibit distinct reactivity [129, 131–133]. As we will demonstrate in the following work, during the electrochemical reduction of adsorbed CO, the reactivity of CO can drastically change depending on the binding configuration of CO. Further, experimental analysis of the electrochemical adsorption of CO on Cu has primarily been carried out on atop-bound CO. The result is a disconnect between experimental and theoretical interpretations regarding the reduction of adsorbed CO to hydrocarbons on Cu electrodes.

To bridge the prior experimental and theoretical work, we carried out systematic studies of CO adsorption and reduction on Cu under alkaline conditions with SEIRAS. Our previous work was carried out under neutral (pH=6.8) or mildly basic conditions (pH 8.3) to study the CO population as a function of potential and alkali metal cation identity [31, 82]. Under these pH conditions, the CO population was found to adsorb primarily in the atop-configuration (CO_{atop}). However, when transitioning to a more alkaline pH, we observe the coexistence of two sub-populations of adsorbed CO: the aforementioned CO_{atop} and CO adsorbed in a bridging configuration (CO_{bridge}). While CO_{bridge} had been ob-

served in a limited capacity previously, the dynamics of this species and relationship to the electrolyte pH had yet to be determined [82, 134–136]. Based on the observations that an alkaline electrolyte leads to an enhancement of ethylene formation and the appearance of CO_{bridge} in alkaline conditions, we want to answer two key questions: (1) Is CO_{bridge} the electroactive population of CO_{ads} that leads to ethylene or other multicarbon products? (2) Does the presence CO_{bridge} broadly affect the catalytic properties of the Cu/electrolyte interface, such as the adsorption of CO_{atop} and/or hydrogen?

With the use of SEIRAS in the attenuated total reflectance configuration (ATR) and complimentary DFT calculations of the Cu electrocatlytic interface, we demonstrate a comprehensive account of the surface dynamics and reactivity of CO_{bridge} on Cu. In this Chapter, we demonstrate the conversion of CO_{atop} to CO_{bridge} when the total coverage of CO drops below saturation conditions. This CO_{bridge} species is irreversibly bound to the Cu surface and can only be removed upon oxidation of the Cu surface. However, under the coverage range studies, CO_{bridge} does not measurably impact the adsorption of CO_{atop}, the on-pathway intermediate towards further reduction. These results provide evidence that not all adsorbed species are on-pathway intermediates in CO_2 reduction on copper electrodes. Here, we find pH and potential driven reconstruction of the Cu surface as the likely source of the increase in CO_{bridge} population. This work highlights the role of the pH in the liquid side of the electrolyte in determining the speciation of CO on Cu. The possibility that the different adsorbed CO populations have different reactivity warrants further investigation into the pH dependent speciation of both oxide species and CO adsorbed at the interface.

3.2 Results

Potential Dependence of CO_{ads} and Assignment of CO Vibrational Bands. To investigate the populations of CO adsorbed (CO_{ads}) on the Cu electrode surface, we collected IR spectra of the Cu/electrolyte interface with SEIRAS on chemically deposited polycrystalline Cu thin-film electrodes during cylcic voltammograms (CVs) in CO saturated 0.05 M Li_2CO_3 electrolyte. The nominal turning potentials of the CVs were 0.11 to -1.1 V vs. standard hydrogen electrode (SHE) with a scan rate of 10 mV/s. For clarity, all potentials in this chapter will be referenced versus the SHE scale. Each turning potential was maintained for 2 minutes before continuing the cycle.

Shown in Figure 3.1A is the potential dependent CO spectra in the $2000 - 2100$ cm^{-1} region collected during the CV experiment. The band observed in this region is ascribable to CO_{atop} [31, 82, 136–145]. In order to estimate the relative coverage of CO_{atop}, we integrated the C≡O stretch band and plotted its potential dependence in Figure 3.2A.

In accordance with previous studies, the adsorption and desorption of CO_{atop} demonstrates a high degree of reversibility [31, 82, 136]. The unique asymmetry in the lineshape with potential (at ≈ -0.8 V of Figure 3.1A) has been investigated previously by our group [31]. In brief, it is the result of CO_{atop} coordinated environment, stemming from CO-induced reversible reconstructions and a complex combination of dynamical dipole coupling between terrace and defect sites [62]. In contrast, a large hysteresis in the potential dependence of the band in the $\approx 1800 - 1900$ cm^{-1} region (Figure 3.1B, labeled CO_{bridge}) is observed. Like with CO_{atop}, the integrated band area of CO_{bridge}, plotted in Figure 3.2A, demonstrates the relative potential dependent population of this species. We initially observe that the onset adsorption potential for both species occurs in the same range. However, the population of CO_{bridge} is maintained well into the anodic region of the reverse scan. By comparing the CO_{bridge} area to the Cu current profile of the CV (Fig-

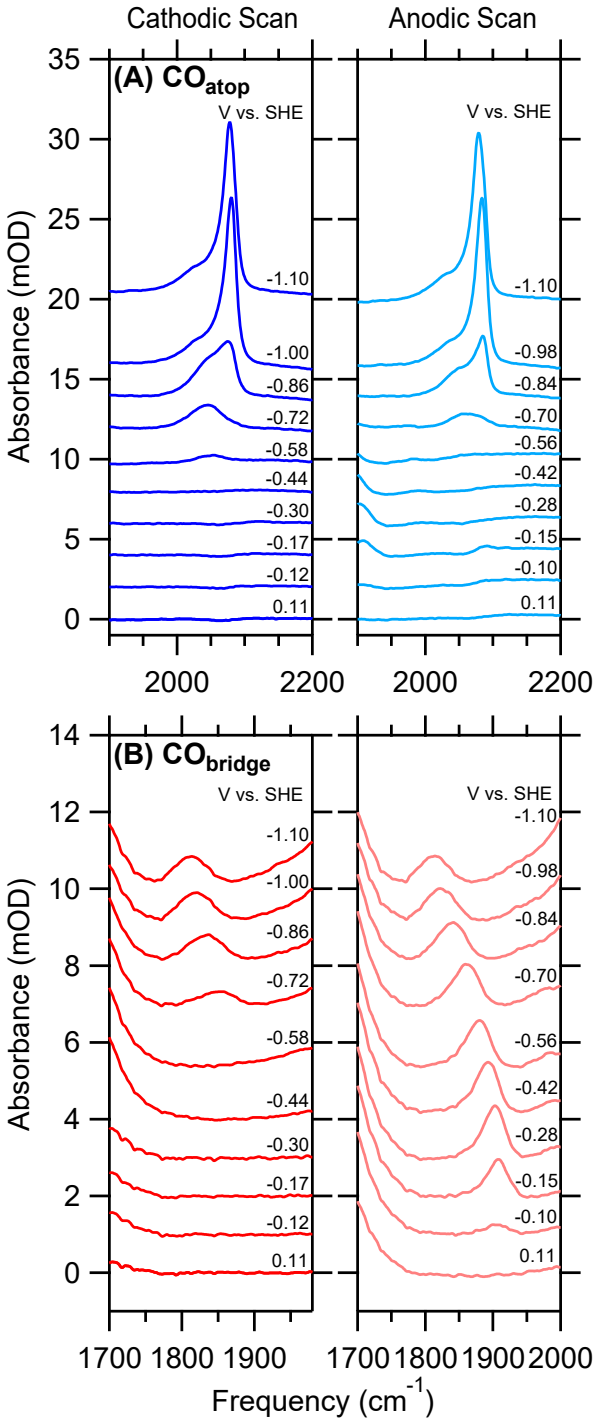

Figure 3.1: Representative IR Spectra in CO-saturated 0.05 M Li_2CO_3 (pH of 11.4) at a scan rate of 10 mV/s plotted in the regions of (A) CO_{atop} and (B) CO_{bridge}. The cathodic forward and anodic reverse scans are shown on the left and right panels, respectively.

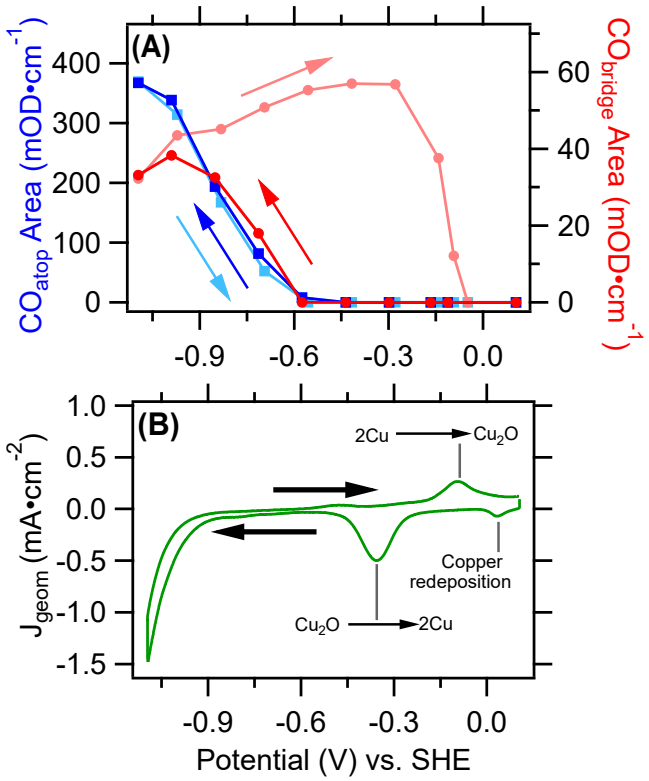

Figure 3.2: (A) Integrated band areas of CO_{atop} (blue squares) and CO_{bridge} (red circles) derived from the spectra in Figure 3.1 with the (B) corresponding current CV. The arrows indicate the direction of the potential scans. CV peaks were assigned according to previous reports [40, 128].

ure 3.2B), the disappearance of CO_{bridge} correlates with the oxidation of Cu at ≈ -0.1 V.

As spectroscopic studies on CO adsorption on Cu have primarily investigated CO_{atop}, we employed density functional theory (DFT) to unambiguously assign the band we have labeled as CO_{bridge}. The adsorption of CO was investigated in Cu(111) and Cu(111) facets with a coverage of 1/4 of a monolayer. Figure 3.3 shows the *ab initio* determined C≡O stretch frequency in various surface-bound configurations as a function of an applied electric field. To confirm the validity of this model, the calculated frequencies need to be compared with experimental studies. For CO_{atop}, the calculated frequencies are found to be within a respectable $\approx 20 - 50$ cm^{-1} of the experimentally observed values (Figure 3.1) [31, 82, 136, 139–146]. Further, the calculated frequencies for a 4-fold bridging site for CO adsorption on Cu(100) agree similarly with previous experimental investigations [133]. Comparing the experimentally observed band in this work from the $\approx 1800 - 1900$ cm^{-1} region (figure 3.1B) with those obtained from the DFT calculations (Figure 3.3) reveals that the CO_{bridge} band likely originates from a population of 3-fold bridged CO on Cu(111) sites and/or a 2-fold bridged CO on Cu(100) sites.

Time- and pH-Dependence of CO Populations. To probe the surface dynamics of CO_{bridge} and CO_{atop}, we carried out chronoamperometry experiments to monitor the CO_{ads} populations as a function of potential, time, and dissolved gas. Operating under the assumption that the integrated band area is proportial to the CO surface coverage, we can monitor the relative populations of each CO species. Plotted in Figure 3.4A is the change in CO coverages, with blue squares representing the integrated band area of CO_{atop} plotted against the left y-axis and red circles representing the CO_{bridge} band area in the right y-axis, over an experiment comprising of three distinct regions. The light colored boundary lines indicate the 95% confidence intervals of the respective band areas. In region 1 of the experiment (grey shaded area), the electrode potential was stepped from the reference potential to -1.1 V and held for (A) 25 min and (B) 1 min with CO saturated 0.05 M

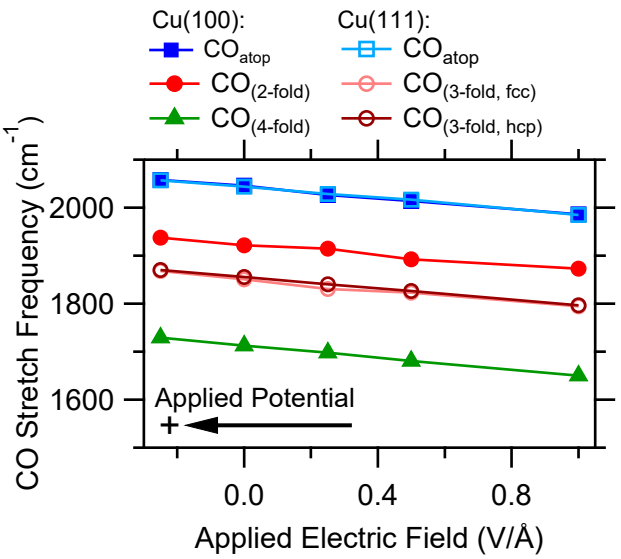

Figure 3.3: Dependence of DFT-calculated C≡O stretch frequencies of CO bound to various adsorption sites on applied electric field. The CO coverage was 1/4 of a monolayer. A more positive electric field represents a more cathodic potential.

Li_2CO_3, and (C) 1 min with CO saturated 0.1 M LiOH. Following region 1, the electrode polarization and gas purging were identical for Figure 3.4: in region 2, the applied potential was maintained at -1.1 V for 25 min, however the gas purging was switched from 5 standard cubic centimeters (SCCM) of CO to Ar. In region 3, the Ar purging was maintained, but the electrode potential was stepped to -1.75 V. This experiment was crafted in such a way to achieve the following goals in each region: (1) Saturate the Cu surface with CO and observe how the pH and length of CO surface saturation effect the initial and ultimate populations of CO sites. (2) Remove CO from the electrolyte and observe any shifts in CO coverage between sites. (3) Step to a reactive potential where CO reduction occurs for any remaining adsorbed species. First, we focus on the CO_{atop} population. In all three panels of Figure 3.4, the same general trend of CO_{atop} is observed. With the initial potential jump, the CO_{atop} reaches a maximum value, and remains relatively constant. Once the gas purge is shifted from CO to Ar, the CO_{atop} declines, consistent with previous reports that CO_{atop} is in dynamic equilibrium with the CO in the electrolyte [134,

147, 148]. Finally, in region 3, any CO_{atop} left on the surface is reduced away, indicated by an integrated band area of 0. The main differences between the three panels of Figure 3.4 arise from CO_{bridge}. In panel A, we initially observe that the CO_{bridge} coverage is relatively low and slowly increases to an integrated band area of ≈ 45 mOD cm^{-1} after 25 minutes. However, when the gas is changed from CO to Ar, despite the decrease in CO_{atop} coverage, the CO_{bridge} monotonically increases. In stark contrast to CO_{atop}, region 3 sees no change in the CO_{bridge} coverage at a electrode potential where CO should easily be reductively desorbed. Taken together, these observations suggest that when the CO_{atop} coverage dips below saturation, it can be converted to CO_{bridge}, and the CO_{bridge} is inert to further electrochemical reduction.

In order to further probe the time dependent dynamics of the CO_{atop} and CO_{bridge} bands, the same experiment was carried out, but with an initial polarization time shortened to 1 min (Figure 3.4(B), gray shaded area). While CO_{atop} is not significantly impacted by this change, we observe that this 1 min polarization results in very little increase in the CO_{bridge} band area when the gas was changed from CO to Ar. This suggests that the conversion of CO_{atop} to CO_{bridge} is a result of changes in the interface that occur under negative electrode polarization on the time scale of tens of minutes. Under such conditions applied here, a change that can occur on this time scale is an increase in the interfacial pH due to the consumption of protons during hydrogen evolution [44, 149]. Interestingly, previous spectroscopic studies have indicated that CO_{ads} on Co, Ni, and Pt is predominantly in the CO_{bridge} configuration under alkaline pH conditions [150–153].

To determine the impact of local pH on the adsorption configurations of CO_{ads}, we carried out the same experiment in Figure 3.4B in 0.1 M LiOH, increasing the initial bulk pH to 12.4. This concentration maintains the same cation concentration as 0.05 M Li_2CO_3, as our previous work has demonstrated that the coverage of CO is cation-dependent [82]. Figures 3.4C shows that the increase in pH had an immediate effect on the CO_{bridge} cov-

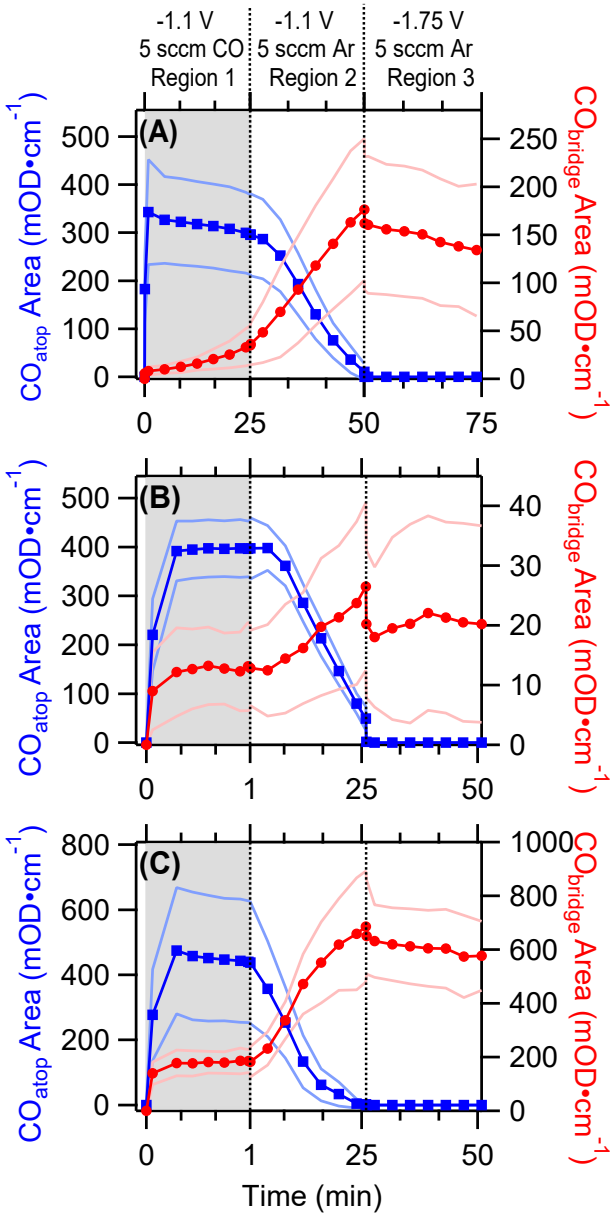

Figure 3.4: Change in integrated band areas of CO_{atop} (blue squares; left y-axis) and CO_{bridge} (red circles; right y-axis) over time: With an initial polarization at -1.1 V for (A) 25 min and (B) 1 min (Region 1) in CO-saturated 0.05 M Li_2CO_3. (C) Same experiment as in panel (B) but in 0.1 M LiOH. Light-colored solid lines indicate the 95% confidence intervals. The main source of uncertainty is the variation in IR enhancement for independently prepared films.

erage, with an initial increase in relative coverage by 10 times after region 1, ultimately reaching a coverage 25 times greater in 0.1 LiOH than in 0.05 M Li_2CO_3. This experiment clearly shows that alkaline pH conditions promoted the accumulation of a significant CO_{bridge} population.

Possible Origins of Observed CO Surface Dynamics. The observed CO surface dynamics can be explained best by three possible explanations relating to electrostatics and surface reconstruction. The first scenario operates under the assumption that increasing the charge density on the electrode favors CO_{bridge} over CO_{atop} sites. This originates from studies on Ni, Co, Pt, and Rh electrode studies, where the ratio of CO_{bridge} to CO_{atop} coverage increases with decreaseing potential [153–157]. The change in binding preference was rationalized by the increase in back donation from the metal electrode to the π^* orbital of CO with an increase in electron density on the metal. Compared to CO_{atop}, CO_{bridge} is able to facilitate a higher degree of back donation and becomes the dominant surface species as the potential becomes increasingly negative.

Generally, the potential of zero charge (PZC) under the SHE scales with the pH, becoming 59 mV more negative per pH unit: $E_{\mathrm{z,\,SHE}} = E_{\mathrm{z,\,pH=0}} - 0.059\,\mathrm{V} \times \mathrm{pH}$ [158]. Therefore, the PZC is invariant on the RHE scale: $E_{\mathrm{z,\,RHE}} = E_{\mathrm{z,\,SHE}} + 0.059\,\mathrm{V} \times \mathrm{pH} = \mathrm{constant}$. This dependence can be traced back to the adsorption of hydroxide anions on the surface of the electrode increasing with the electrolyte pH [158]. However, in the presence of CO, the adsorption of hydroxide can be disrupted, resulting in a $E_{z,SHE}$ that is invariant with pH and an $E_{z,RHE}$ that shifts positively with pH. Under these conditions, for a given applied potential on the RHE scale, the charge density should be more negative under an alkaline pH than a relatively more acidic pH. Assuming more charge density favors CO_{bridge}, the coverage of this population should increase.

This explanation based on electrostatics does not apply to this case. First, the applied potentials in this chapter are reported against the SHE scale. Thus, if the applied potential

on this scale is independent of pH, the charge density on the electrode would be invariant of the pH for a given SHE potential. Further, under the assumption the $E_{z,SHE}$ has the theoretical pH dependence of $-0.059\ \mathrm{V} \times \mathrm{pH}$, [158], the absolute negative charge density would actually decrease with increasing pH.

The observed surface dynamics of CO are more likely to emerge as a result of the reconstruction of the Cu surface during catalytic conditions. It has been shown that Cu surfaces can readily reconstruct under a variety of experimental conditions [31, 39, 41, 42, 159–163]. The reconstruction observed in this study can likely manifest in two possible ways, with the first being slow reduction of Cu oxide phases during cathodic polarization. It is possible that kinetically stable Cu oxides can persist at a potential of -1.1 V, where they are no longer thermodynamically stable [164], and influence the adsorption behavior of CO. This subject has been the matter of debate, with some studies finding no evidence of Cu oxides under CO_2 reduction conditions [165–167], and others both observing oxides under cathodic polarization and implicating them as key promoters of hydrocarbon formation [112, 116, 168]. To investigate the possible presence of oxide phases on Cu, we collected spectral data with surface-enhanced Raman scattering (SERS). In Ar saturated 0.05 M Li_2CO_3, SERS spectra obtained at open circuit and -0.5 V showed the presence of clear copper oxide/hydroxide bands (Figure 3.5). However, when the potential was polarized to -1.1 V, no oxide phases were detected. This suggests that the Cu surface is fully reduced and refutes that kinetically stable oxides are influencing the dynamics of surface adsorbed CO.

We postulate that the CO population dynamics are the result of differing degrees of polarization- and pH-dependent reconstruction to unique surface facets that favor CO_{bridge} binding. Strong evidence for this comes from scanning tunneling microscopy imaging studies of Cu electrodes under prolonged cathodic polarization [39, 163, 169]. It was observed that under alkaline and mildly alkaline pH conditions, cathodic polarization of

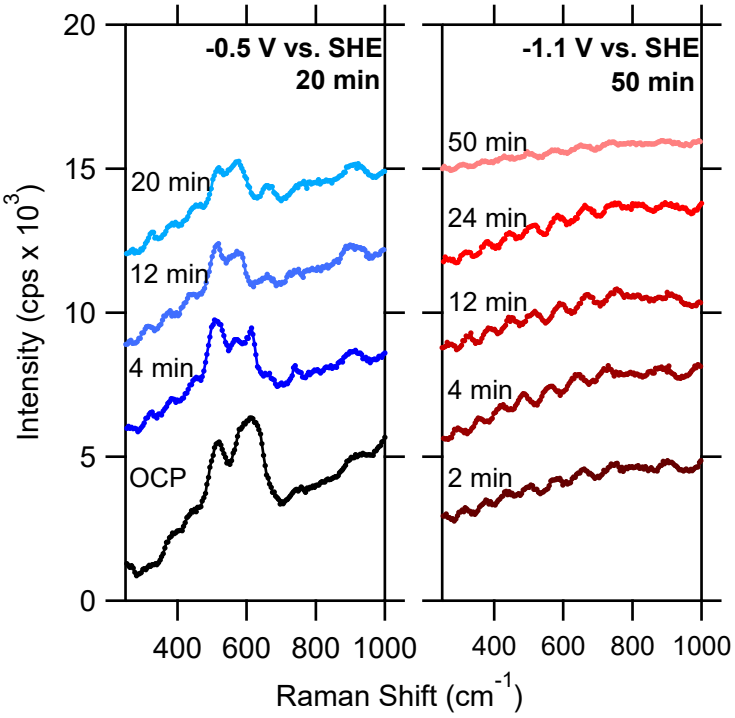

Figure 3.5: Representative SERS spectra of the Cu electrode surface in Ar-purged 0.05 M Li_2CO_3 at (left panel) -0.5 V and (right panel) -1.1 V. The black spectrum in (left panel) is collected at open circuit potential. The two major peaks at 517 and 610 cm^{-1} are assigned to Cu_2O.

the Cu surface on the scale of tens of minutes, the initially polycrystalline Cu surface reconstructed to Cu(111) and then to Cu(100). Our experiments demonstrate that under increased pH and prolonged electrolysis conditions, CO_{bridge} sites increase in coverage. Taken together, we therefore ascribe the observed CO population dynamics to pH induced surface reconstruction of Cu. Specifically, it is likely that Cu(100) or Cu(111) like sites are formed during this surface reconstruction, allowing CO to irreversibly bind in 2-fold and/or 3-fold bridging configurations. However, co-adsorption of hydroxide ions may additionally favor the irreversible adsorption of CO [170].

Insensitivity of CO_{atop} Coverage to CO_{bridge} Population. With the accumulation of an irreversible adsorbed species like CO_{bridge} at the Cu surface, it is possible that this species can modulate catalysis in the blocking of sites for hydrogen or by modulating the adsorption energy of CO_{atop} [72, 130]. To test this hypothesis, we probed how the amassing of CO_{bridge} coverage affects the CO_{atop} coverage. This was done by carrying out a series of consecutive CVs. Figure 3.6 shows the integrated band area at the beginning and end of each turning potential as a function of time during CVs, the second cycle of which was previously described in Figure 3.2. As the potential is cycled between -1.1 and 0.11 V, the CO_{bridge} integrated band area montonically increases. In contrast, the band area of CO_{atop} remains virtually the same across the four cycles. Therefore, under this coverage range, the population of CO_{atop} remains unaffected by the increase in coverage of CO_{bridge}. This observation demonstrates that the total coverage of adsorbed CO is well under one monolayer [72] at this potential and that CO_{atop} and CO_{bridge} are adsorbed at different sites.

Origin of the Electrochemical Inertness of CO_{bridge}. To gain insight into the electrochemical inertness of CO_{bridge}, we carried out DFT analysis of the further reduction of adsorbed CO species. Again, Cu(100) and Cu(111) surface facets were used as model electrode surfaces. Figure 3.7 shows the formation energy of CO at differently configured

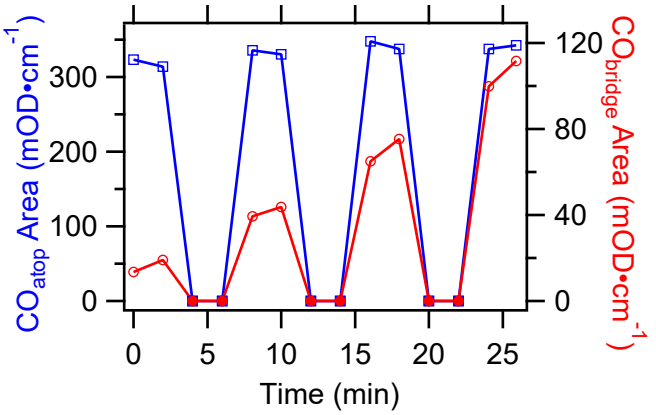

Figure 3.6: Integrated band areas of (blue squares, left y-axis) CO_{atop} and (red circles, right y-axis) CO_{bridge} at the turning potentials of (hollow symbols) -1.1 and (solid symbols) 0.11 in consecutive CVs.

adsorption sites as a function of electric field. The more positive electric field is indicative of a more cathodic potential.

When the electric field is increased from -0.25 to 1 V/Å, the formation free energy of CO_{atop} remains relatively constant, while the CO_{bridge} formation energy becomes more negative by ≈ 0.1 eV. This suggests that more negative potentials (positive electric fields) favor bridge binding for CO.

We further used DFT to justify the difference in reactivity between CO_{atop} and CO_{bridge}. This was accomplished by calculating the thermodynamics and corresponding activation barriers for the H_2O-assisted hydrogenation of CO to CHO on Cu(100) as a function of electric field (Figure 3.8). The activation barrier for CO_{atop} to 2-fold CHO exhibits little change with an increasingly large applied electric field. In contrast, the activation barrier between 2-fold and 4-fold CO_{bridge} and 4-fold CHO increases in the presence of an increasingly large applied electric field. This is a result of this increased stability that CO_{bridge} maintains as the potential is more cathodic and the applied electric field becomes more positive. Therefore, the electrochemical inertness of CO_{bridge} likely originates from its stabilization at increasingly negative potentials on Cu electrodes.

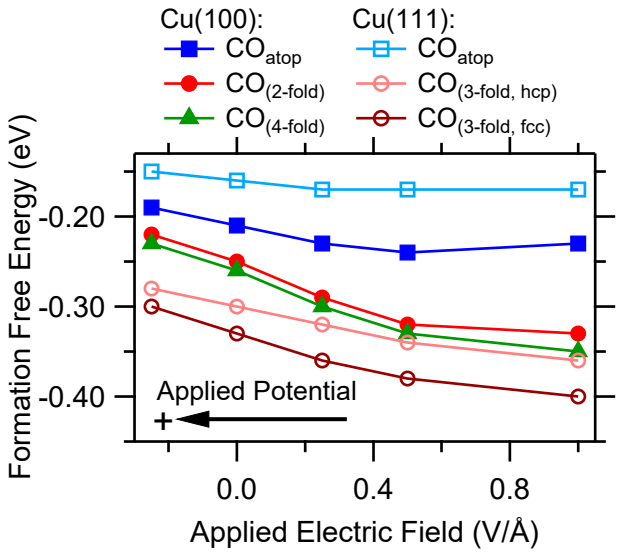

Figure 3.7: Formation energy of CO at different adsorption sites on Cu(111) and (100) as a function of applied electric field.

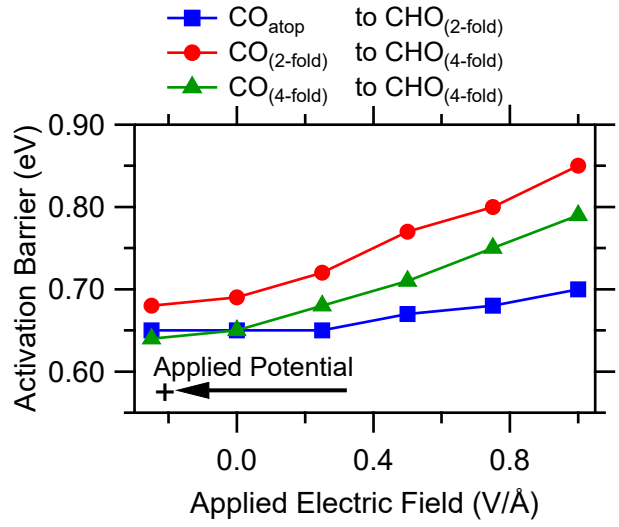

Figure 3.8: Activation barrier for the water-assisted hydrogenation of CO to CHO on Cu(100) as a function of applied electric field. A more positive electric field indicates that the potential has become more cathodic.

3.3 Conclusions

This chapter demonstrates that under alkaline pH conditions in the liquid side of the Cu/electrolyte interface, a CO_{bridge} population develops. This population growth is promoted by irreversible surface reconstruction originating from high pH and extended cathodic polarization of the electrode over the course of tens of minutes. This leads to the formation of sites that favor a multiply bonded CO species. We find that CO_{bridge} is unexpectedly inert to electrochemical reduction, but does not significantly impact the adsorption of the on-pathway CO_{atop} population.

3.4 Experimental Procedures

Materials. HF (48 wt%), NH_4F (40 wt% in H_2O), and Li_2CO_3 (99.999%; trace metals basis) were aquired from Fisher Scientific. $CuSO_4{\cdot}5H_2O$ (99.999%; trace metals basis), HCHO (35 wt%; 10% methanol as stabilizer), $LiOH{\cdot}H_2O$ (99.95%; trace metals basis), Na_2EDTA (99.0-101.0%; ACS Reagent), NaOH (99.99%; trace metals basis), and 2,2-bipyridine ($\leq$99%; ReagentPlus) were purchased from Sigma-Aldrich. Polycrystalline diamond pastes were purchased from Ted Pella (Redding, CA) or Electron Microscopy Sciences (Hatfield, PA). Ar (Ultra High Purity) and CO (99.999%) were procured from Air Gas. High purity water (18.2 MΩ cm) was sourced from a Barnstead Nanopure Diamond system (APS Water Services; Lake Balboa, CA) and used for all experiments.

Cu Thin Film Deposition. Cu thin films were electrolessly deposited onto the reflecting pane of a 60° Si ATR prism (Pike Technologies; Madison, WI). This was accomplished by first polishing the Si prism reflecting pane by hand on a polishing pad with 6 and 1 μM diamond slurries for 10 min each. Following this, the surface was polished with 0.5 μM diamond paste with a cotton swap for 5 minutes. The surface was then polished with

fresh cotton swabs until the paste was completely removed from the surface. The Si prism surface was then wiped with a folded Kim-wipe under flowing high purity water for 5 minutes. Following this, the prism was placed into a PTFE holder and sonicated consecutively in alternating baths of water and acetone for 10, 5, and 5 min each. During this time, the seeding and plating baths were prepared as follows. The seeding bath was made up of a 25 mL volume of 0.5 w.t% HF with 750 μM $CuSO_4$. The plating bath (20 mM Na_2EDTA, 0.3 mM 2,2-bipyridine, 20 mM $CuSO_4$, and 250 mM HCHO; pH 12) was made up of initially two separately prepared solutions: a 5 mL solution Na_2EDTA and 2,2-bipyridine adjusted to a pH of 12 with solid NaOH was added dropwise into a 10 mL of a mixture of dissolved $CuSO_4$ and HCHO and diluted to a total volume of 25 mL. The final pH was adjusted to 12.05-12.20 with solid NaOH. This plating bath was first heated for 10 minutes in a water bath set at 54-55°C. Following this, the Cu thin-film was deposited by first dipping the reflection plane of the Si prism in 40 wt% NH_4F for 30 s. The surface was rinsed with high purity water and immediately dipped into the seeding solution for 1.5 min. The prism was then gently rinsed with water and placed into the plating bath for 3.5 min. Following the deposition, the film was rinsed, dried under gentle N_2 gas flow, and the resistance of the film measured to be 5-30 Ω. The cell was then immediately assembled and the Cu film subsequently covered in 4 mL of either 0.05 M Li_2CO_3 or 0.1 M LiOH. This electrolyte was then purged with Ar or N_2 to remove dissolved O_2 and subject to cleaning and capacitance CVs (-0.13 to -0.6 V vs. Ag/AgCl at 50 mV/s scan rate and -0.6 to -0.7 V at 20, 40, 60, 80, and 100 mV/s). The capacitance measurements allowed the determination of the surface roughness factor to be between 10-12, in good agreement with previous reports (Addendum, Figure A3.2) [31].

Electrochemical methods for ATR-SEIRAS Measurements. SEIRAS experiments were carried out in a single-compartment polyetheretherketone (PEEK) cell (Addendum, Figure A3.1). The PEEK components of the cell were cleaned in an acid bath (30 wt%

HNO_3 + 30 wt% H_2SO_4) for 1 hour followed by sonication in water for 1 hour. The overall cell was assembled with the chemically deposited Cu-thin film working electrode, a Au wire (99.999%, 0.5 mm thick, Alfa Aesar) counter electrode, and a Ag/AgCl (RE-5B, 3 M NaCl, BASi Inc,; West Lafayette, IN) reference electrode. The potential was manipulated using a VersaStat3 potentiostat (AMETEK; Berwyn, PA). 85% of the solution resistance was compensated *in-situ* for all electrochemical experiments.

ATR-SEIRAS Measurements. FTIR spectra were collected with a nitrogen-purged Bruker Vertex 70 FTIR spectrometer (Billerica, MA) interfaced with a liquid nitrogen-cooled MCT detector (FTIR-16; Infrared Associates; Stuart, FL). Spectra were collected with a 40 kHz scanner velocity and 4 cm^{-1} resolution. To determine the potential and time dependent spectra, the change in the absorbance (ΔOD) was calculated with the following; $\Delta mOD = -10^3 log(S/R)$, where S and R represent the respective sample and reference single beam spectra.

SERS Measurements. SERS data were collected in a Horiba Scientific Xplora Raman microscope (638 nm laser) interfaced with a water immersion objective (NA = 1.0, WD = 2.0 mm; LUMPLFLN-60X/W; Olympus Inc.; Waltham, MA) wrapped in a 0.006 mm thick protecting Teflon sheet with a drop of water between the objective and the sheet. Spectra were collected over an acquisition time of 25 s, a 600 lines/mi grating, 300 μm hole, and 100 μm slit. A Si standard was used to calibrate the instrument prior to each experiment.

SERS data was collected with the same Cu-thin film used for SEIRAS deposited onto a Si wafer. The Cu-coated Si wafer was assembled into a custom Raman cell. After cleaning the cell in with the same method used for the SEIRAS cell, 50 mL of 0.05 M Li_2CO_3 was placed on top of the Cu-coated Si wafer and purged with Ar for $\sim$ 30 min. The Cu film was then cleaned with CVs and the roughness factor determined as described previously. Spectra were taken every two minutes throughout the following experiment: the potential

was held at open circuit for $\sim$ 2 min before applying -0.5 V vs. SHE for 20 minutes, followed by a potential step to -1.1 V vs. SHE maintained for 50 min.

3.5 Addendum

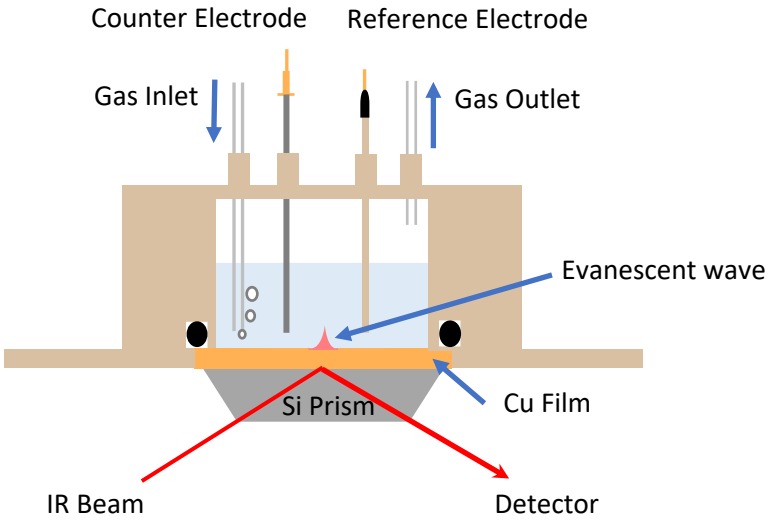

Figure A3.1: Cartoon depiction of the electrochemical cell used in this chapter.

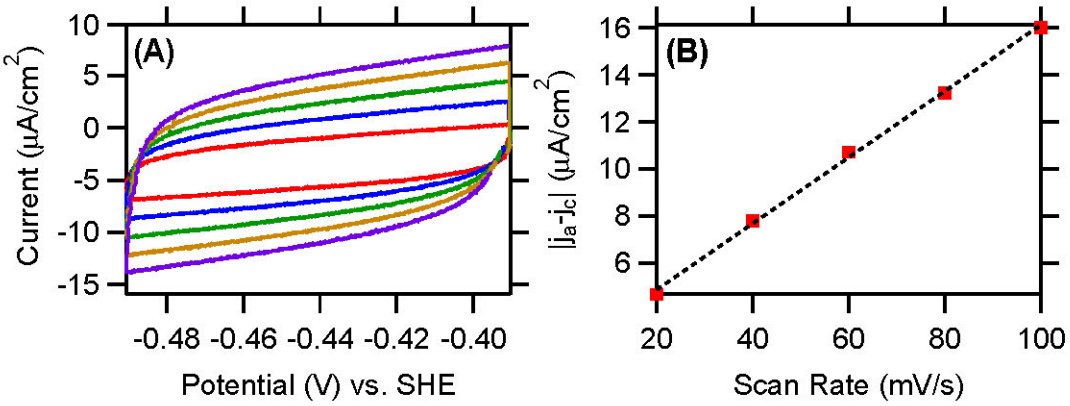

Figure A3.2: (A) Representative capacitance CVs taken at scan rates of (red) 20, (blue) 40, (green) 60, (yellow) 80, and (purple) 100 mV/s. The CVs were used to determine the double layer charging current vs. scan rate plotted in B with a linear fit. The roughness of the film was calculated by dividing the slope of the line by a factor of two and a reference capacitance value for a smooth Cu surface ($28\mu\text{Fcm}^{-1}$) [171].

3.6 Acknowledgements

We acknowledge the financial support by the National Science Foundation (award no.: 1565948). V. J. O. expresses gratitude to Xiang Li and Paul Hicks for help collecting and analyzing SERS data. V. J. O. further thanks Charuni M. Gunathunge for guidance in this project and Jingyi Li for their support in collecting SEIRAS data.

3.7 Original Publication

This chapter has been published: Gunathunge, C. M., Ovalle V. J., Li. Y., Janik M. J. & Waegele, M. M, *ACS Catal.* **8**,7507–7516 (2018).

Chapter 4

Modulation of Interfacial pH and Intermediates with N-Arylpyridinium Ions: Impact on Selectivity of CO_2 Reduction at the Cu/Electrolyte Interface

4.1 Introduction

Chapter 3 demonstrated that electrocatalysis in an alkaline pH can be a strong driving-force for the liquid side of the interface to alter the catalyst structure. Reconstruction of the catalyst morphology led to a significant coverage CO_{bridge}. With SEIRAS, we were able to determine that the CO_{bridge} formed under these conditions is an inert species in the further reduction of CO on Cu electrodes. Even though CO_{bridge} is electrochemically inert on Cu electrodes under alkaline pH conditions, these pH conditions have been employed to improve the product selectivity during CO_2 reduction. Coupled with optimized Cu electrode morphologies, high pH electrolytes have enabled the conversion of CO_2 and CO to $C_{\geq 2}$ hydrocarbons with selectivities of $>$70% [111, 115, 119, 172, 173]. Besides altering the pH, a simple strategy for impacting the catalyst structure, surface intermediate populations, and ultimately the catalytic selectivity and rates during CO_2/CO reduction is with organic additives [65–69, 174–185]. For example, during CO_2 reduction on Ag elec-

trodes, the presence of diaminotriazole improves the selectivity towards CO over hydrogen by one order of magnitude compared to when it is absent [65, 186]. Modification of the Au and Cu electrode surfaces with a variety of organic compounds can also substantially tune catalysis. In comparison to the unmodified surfaces, enhancements in the selectivities towards valuable products have been observed with Cu and Au electrodes modified with amino acids [66], poly-amides [176], and thiol-containing compounds [67]. Han and coworkers have reported selectivities as high as $70 - 80\%$ for $C_{\geq 2}$ products generated from CO_2 reduction with the presence of an organic film derived from N-arylpyridinium compounds at the Cu electrode/electrolyte interface [69].

The origins of these changes in selectivity is manifold: it can include the modulation of adsorption energies of key intermediates, change in the reaction pathway, or blocking of catalytic sites. Understanding what mechanisms are at play with surface modifications are critical to utilizing them effectively to alter catalysis. However, many of these mechanisms remain largely unexplored.

In this Chapter, we used SEIRAS to probe the Cu/electrolyte interface to determine the impact that organic films derived from N-arylpyridinium compounds have during CO_2 reduction. The impact of these films on CO_2 reduction was intriguing; the product selectivity changed drastically. For some of these films, Faradaic efficiencies for $C_{\geq 2}$ hydrocarbons reached up to $\approx 80\%$ [69]. However, the changes in selectivity varied greatly with the chemical structure of the N-arylpyridinium compound. In the presence of a different organic film, the formation of hydrocarbons was essentially shutdown. Therefore, this system provided the opportunity to understand the interfacial properties of molecular additives that can be beneficial or detrimental to electrocatalytic selectivity.

4.2 Results and Discussion

Choice of Additives. In this work, we chose two arylpyridinium chloride derivatives, 1-(4-tolyl)pyridinium (T-Pyr) and 1-(4-pyridyl)pyridinium (P-Pyr), that had been reported to modulate the product selectivity during CO_2 reduction on polycrystalline copper electrodes in contrasting ways [69]. The chemical structures of each are shown in Figure 4.1. It was previously discovered that the presence of 10 mM of each compound dissolved in the electrolyte, under cathodic polarization of the electrode, resulted in the reductive deposition of the compounds onto the electrode surface. The white, visible films that formed at the surface were demonstrated to exhibit unique influences on the product selectivity during CO_2 reduction. The partial currents for the main CO_2 reduction products measured by Han *et al.* [69] are summarized in Table 4.1. In the presence of the organic film formed from T-Pyr, the rate of methane and hydrogen formation fell greater than an order of magnitude in comparison to the unmodified Cu electrode, while the rates of $C_{\geq 2}$ species (ethylene, ethanol, and propanol) were only slightly reduced. In contrast, the films derived from P-Pyr virtually shut down the rates of production for all hydrocarbons species, while maintaining the same rate of hydrogen formation of the unmodified Cu electrode. This chapter will use SEIRAS to identify the physical and chemical origins of the observed impact on the CO_2 reduction product distribution dealt by the T-Pyr and P-Pyr films at the Cu/electrolyte interface

Formation of T-Pyr- and P-Pyr-derived Films. The formation of the organic films was monitored with cyclic voltammetry coupled with SEIRAS. A similar experimental setup was used with Chapter 3, where a chemically deposited polycrystalline Cu thin film was deposited onto the reflecting pane of a Si ATR element. In order to prevent the cross-contamination of oxidized products, an updated two-compartment cell with an anion-exchange membrane and stirring functionalities was employed(Addendum, Figure A4.5.

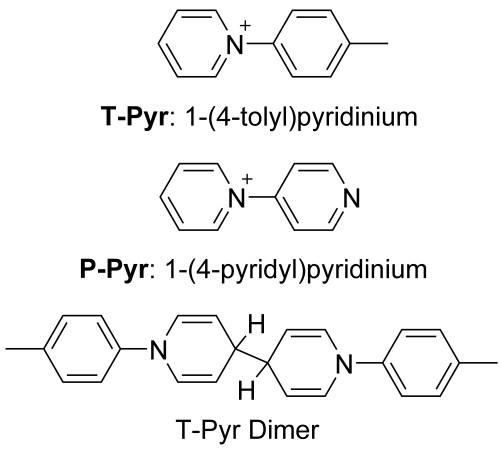

Figure 4.1: Chemical structures of T-Pyr, P-Pyr, and the T-Pyr dimer.

Table 4.1: Partial current densities of various reduction products for polycrystalline Cu electrodes in the presence and absence of 10 mM T-Pyr/P-Pyr in CO_2-saturated 0.1 M $KHCO_3$ at an applied potential of -1.1 V vs RHE, as reported by Han and coworkers [69].

	Current Density (mA cm^{-2})		
Compound	CH_4	H_2	$C_{\geq 2}$
Unmodified Cu	0.90	1.91	1.16
T-Pyr	0.01	0.16	0.80
P-Pyr	0.001	1.94	0.00

Aqueous solutions of 0.5 M $KHCO_3$ (pH 7.4) with and without 10 mM P-Pyr and T-Pyr were saturated with CO_2 and used as the electrolytes. These electrolytes and electrochemical setup allowed us to observe the film-induced changes in the product selectivities reported in Table 4.1. In this chapter, all potentials are referenced against the silver/silver chloride electrode (Ag/AgCl) unless otherwise noted.

Shown in Figure 4.2 is the cyclic voltammograms (CVs) in the presence and absence of 10 mM P-Pyr and T-Pyr. In the absence of these additives, the current density rapidly and monotonically increases in magnitude in the cathodic forward scan. In contrast, the presence of either P-Pyr or T-Pyr results in a reduction wave at ≈ -0.9 V. This wave is due to the reduction of P-Pyr and T-Pyr [69]. The reduction of either of these species forms a visible white film on the Cu electrode that is maintained even after the cell is disas-

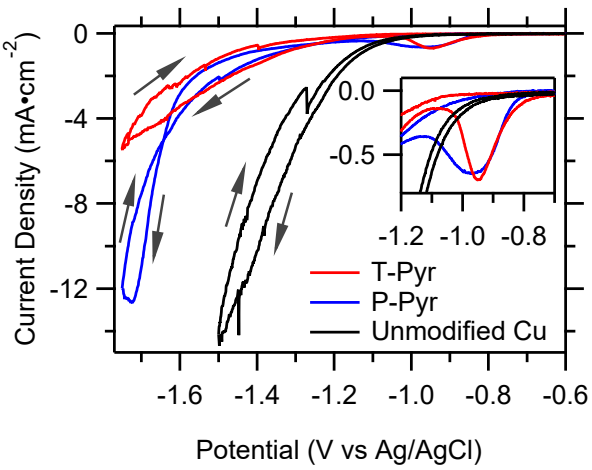

Figure 4.2: CVs of Cu thin films in CO_2-saturated aqueous solutions of 0.5 M $KHCO_3$ in the absence (black) and presence of 10 mM P-Pyr (blue) and T-Pyr (red). The scan rate was 2 mV s^{-1}. The inset shows the waves due to the reductions of P-Pyr and T-Pyr.

sembled. For T-Pyr, *ex situ* NMR spectroscopy has demonstrated that the reduced species is a hydrogenated T-Pyr dimer (Figure 4.1) [69]. The spectra corresponding to -1.1 V of the CV where the organic films have formed are shown in Figure 4.3A. These spectra are difference spectra, with the reference taken before the addition of T-Pyr or P-Pyr to the bulk electrolyte. This results in the presence of spectral features from both solution species and the solid film. In order to delineate the film formation from their precursors, IR spectra of T-Pyr and P-Pyr is shown in Figure 4.3B. We focused our analysis on the feature that appears during the CV at ≈ 1685 cm^{-1} (indicated by the dashed line in Figure 4.3A). In comparison to the solid and solution phase spectra, this band is only present in the spectra at the electrochemical interface in the presence of T-pyr and P-Pyr. These observations demonstrate that the band at ≈ 1685 cm^{-1} emerges from the film formation at the interface. The frequency of the band is also consistent with the C=C stretch of an alkene group [187]. Upon dimerization of T-Pyr and P-Pyr, the aromaticity of the ring systems is lost, thereby resulting in the observation of the alkene group (Figure 4.1). The observation of this band confirms that T-Pyr and P-Pyr are in a reduced state during their

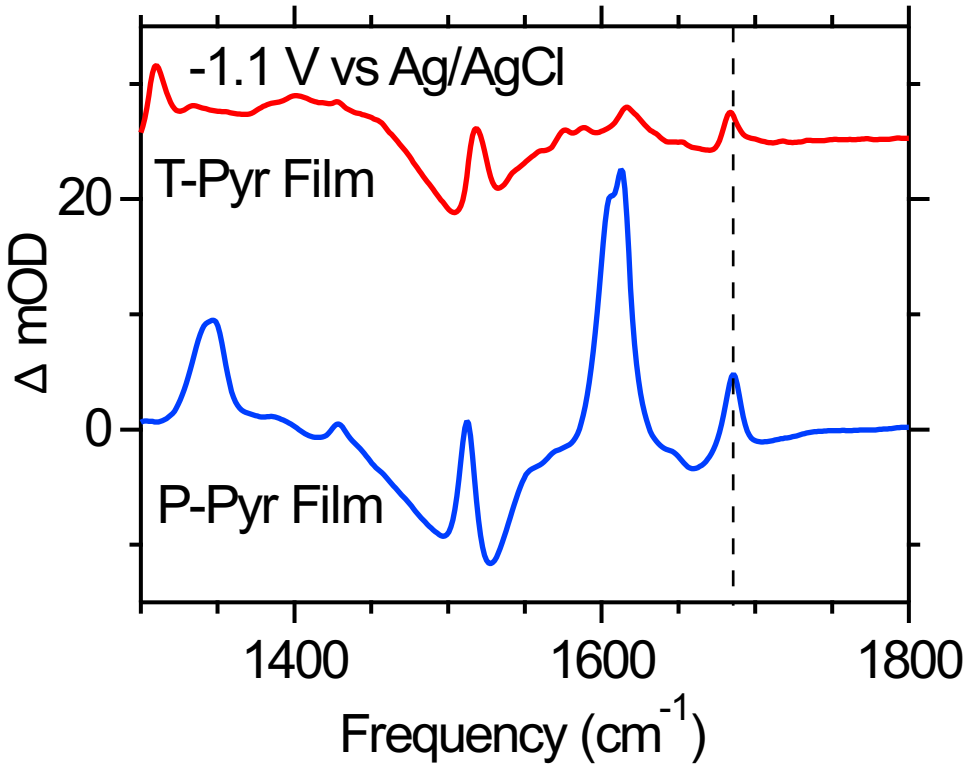

Figure 4.3: (A) IR spectra of the Cu/electrolyte interfaces in the presence of 10 mM T-Pyr (red) and 10 mM P-Pyr (black) in CO_2-saturated 0.5 M $KHCO_3$ at a potential of -1.1 V. The reference spectrum was taken at -0.6 V immediately before the arylpyridiniums were added. The band indicated by the dashed line is consistent with the C=C stretch of an alkene. (B) Transmission IR spectra of solid-phase T-Pyr (red) and P-Pyr (black) and their aqueous solutions.

film formation and CO_2 reduction conditions.

The presence of the films significantly reduces the magnitude of overall reductive current compared the unmodified Cu interface (Figure 4.2). This is expected and originates from the reduced partial currents for the respective products measured at a potential of -1.1 V vs RHE by Han and co-workers [69]. The lower current with T-Pyr is primarily from the > 10 times lower partial currents for hydrogen and methane in comparison to the unmodified Cu surface. In contrast, the lower current with P-Pyr primarily originates from

the drastically reduced currents for hydrocarbons.

Spectra taken after the reduction wave at -0.9 V reveal little changes in the organic film features with potential, suggesting the organic film growth is a self-limiting process (Addendum, Figures A4.1 and A4.2).

Effect of T-Pyr on Interfacial Characteristics. The impact of T-pyr on CO_2 reduction product selectivity is revealed through the analysis of interfacial carbonate (CO_3^{2-}). Figure 4.4 shows representative potential dependent IR spectra of the three interfaces in the region of $1300 - 1600$ cm^{-1}. For clarity, these spectra represent the change in absorbance (optical density) at the indicated sample potential with respect to the reference potential of -0.6 V, taken at the end of the CV. The bands around 1330/1350 cm^{-1} and 1515 cm^{-1} in the presence of T-Pyr (Figure 4.4A) and P-Pyr (Figure 4.4B) correspond to Stark tuning of film-related vibrational modes with potential. The broad negative band at $\approx$ 1525 cm^{-1} in the unmodified Cu/electrolyte interface is due to the desorption of surface-adsorbed carbonate and/or bicarbonate [82, 188].

In the presence of the T-Pyr film, a large broad positive band appears ≈ 1410 cm^{-1} at cathodic potentials (Figure 4.4A). As the potential is tuned positively, this band decreases. A similar band is present at the P-Pyr modified Cu/electrolyte interface (Figure 4.4B), but with a substantially smaller amplitude. This band is completely absent at the unmodified Cu/electrolyte interface (Figure 4.4C). These observations lead to the distinction of T-Pyr modified Cu/electrolyte interface from the others with the presence of the relatively larger magnitude of the band at ≈ 1410 cm^{-1}.

The ≈ 1410 cm^{-1} band at the Cu/electrolyte interface has previously been attributed to the out-of-phase stretching vibrations of solution-phase carbonate (CO_3^{2-}) in the vicinity of the electrode [145, 189–191]. We believe this is a reasonable assignment due to a number of explanations: The first being that other possible intermediate species that could appear in this IR region are most likely to be at very low surface concentrations, preventing their

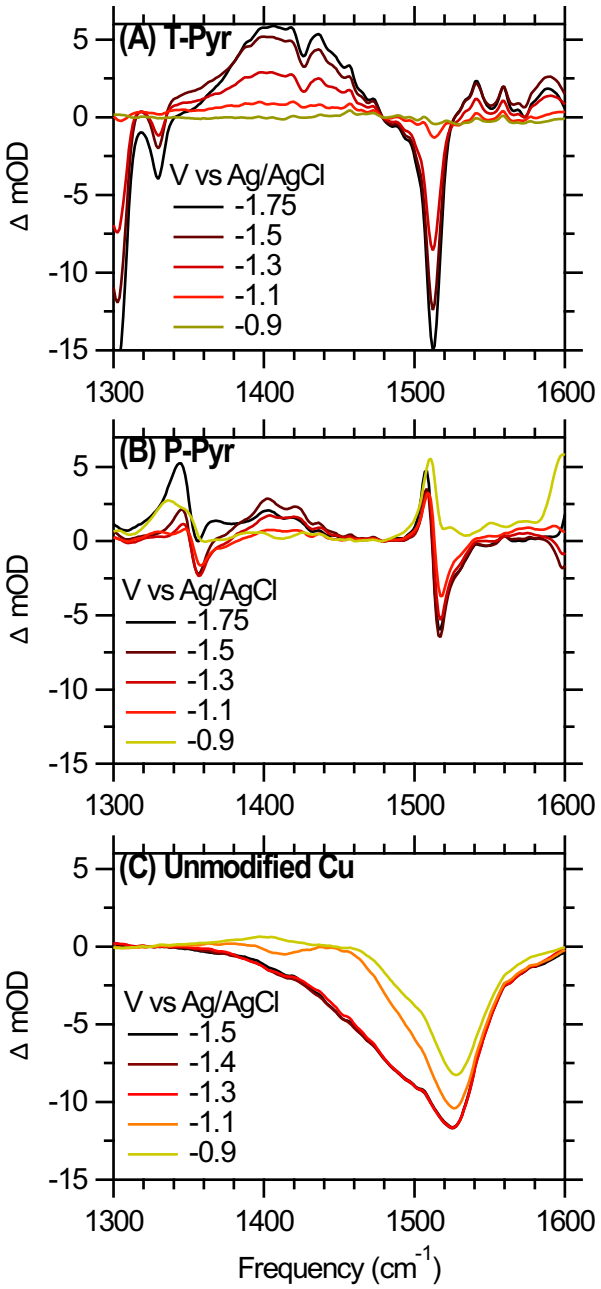

Figure 4.4: Potential-dependence of the carbonate band (≈ 1410 cm^{-1}) during the anodic reverse scan of the CV (Figure 4.2) in the absence and presence of the organic films as indicated. The final spectrum at the anodic end of the scan (-0.6 V) served as the reference spectrum.

detection. Next, the IR transmission spectrum of 10 mM K_2CO_3 shows a feature at a similar frequency and a comparable width (Addendum, Figure A4.3). Finally, for every electron-transfer in CO_2 reduction and hydrogen evolution, a hydroxide ion is produced according to:

$$\mathrm{A} + \mathrm{H_2O} + \mathrm{e^-} \longrightarrow \mathrm{B} + \mathrm{OH^-}, \tag{4.1}$$

Where A and B represent the respective oxidized and reduced species. In the absence of efficient mass transport, we therefore expect the local pH in the vicinity of the electrode to increase due to the Faradaic current. The increase in pH will lead to the deprotonation of the electrolyte's bicarbonate anions:

$$\mathrm{HCO_3^-} + \mathrm{OH^-} \longrightarrow \mathrm{CO_3^{2-}} + \mathrm{H_2O}. \tag{4.2}$$

To test the correlation of this bands' amplitude with deficient mass transport at the interface, we recorded IR spectra of the unmodified Cu/electrolyte interface with and without stirring at a potential of -1.5 V. Shown in Figure 4.5A, during the time period after stirring stops at $t = 0$ s, the band at ≈ 1410 cm^{-1} indeed grows in. After the stirring is restarted in Figure 4.5B, the band disappears within a few seconds. These observations confirm that the appearance of this band is linked with poor mass transport at the surface. Based on the peak frequency and large pool of bicarbonate in the electrolyte, we attribute this band to solution-phase CO_3^{2-} produced according to reaction 4.2. Ultimately, an increase in this band indicates an increase in the local pH in the vicinity of the electrode.

According to reaction 4.2, the electrochemical interface with the largest Faradaic current should have the largest carbonate band. However, further inspection of Figure 4.2 reveals that the smallest current is observed with the T-Pyr-modified Cu/electrolyte interface. However, the presence of the largest carbonate feature occurs with the T-Pyr-modified Cu/electrolyte interface, indicating the largest pH increase. We would expect the

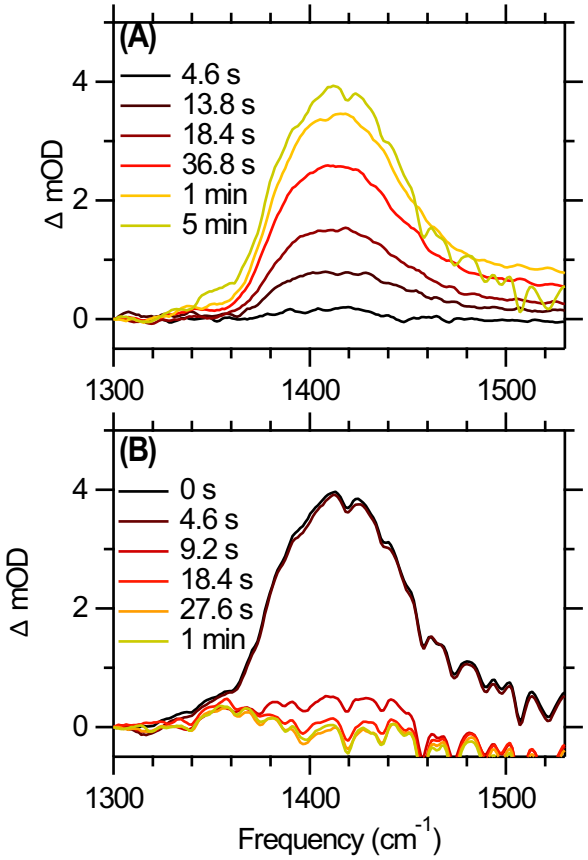

Figure 4.5: Time-evolution of the carbonate band at the unmodified Cu/electrolyte interface with the Cu electrode held at a potential of -1.5 V: (A) after stirring of the electrolyte was stopped and (B) after stirring at 900 rpm was resumed. The stop/start time is $t = 0$ s in each panel. The reference spectrum was taken at -1.5 V, right before the stirring was initially stopped.

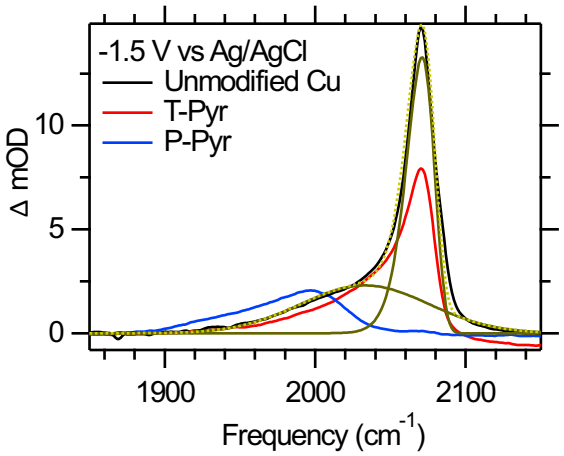

Figure 4.6: Comparison of the C≡O stretch bands of CO_{atop} on Cu at an applied potential of -1.5 V at the three different interfaces as indicated. The green dashed line represents a fit of the model, the sum of the two (skewed) Gaussian functions, [31, 192] to the spectrum of CO_{atop} at the unmodified Cu electrode (black). The solid green lines represent the Gaussian functions.

T-Pyr modified interface to have the smallest increase in local pH at the interface. Base on this observation, the presence of the T-Pyr-derived film may be physically obstructing the electrode from buffering species in the bulk electrolyte. SEM images of the T-Pyr- and P-Pyr-derived films shows that the films exhibit unique surface structures (Addendum, Figure A4.4). Taken together, the results indicate that the T-Pyr-derived film limits the interfacial mass transport due to its unique morphology, thereby leading to an accumulation of hydroxide in the vicinity of the electrode.

An increase in pH and lower buffering capacity at the Cu/electrolyte interface has been previously been demonstrated to decrease the rates of hydrogen and methane evolution, while the rates of ethylene formation remains indifferent to pH changes [22, 64, 193]. The same argument has been invoked to explain the increase in CO_2 reduction selectivity and decrease in hydrogen evolution on porous metal electrodes [194–196]. Further, a high (local) pH can limit the availability of surface-adsorbed hydrogen, a common reaction intermediate during the production of methane and hydrogen gas [197]. Our spectroscopic

results clearly demonstrate the comparatively highest pH gradient at the T-Pyr-modified Cu/electrolyte interface (Figure 4.4). Consequently, the rate of methane and hydrogen formation are reduced with the T-Pyr-derived films.

Effect of P-Pyr on the Adsorption of CO. In contrast to T-Pyr, P-Pyr-derived films result in little to no hydrocarbon evolution but rather an unperturbed rate of hydrogen evolution with respect to the unmodified-Cu/electrolyte surface (Table 4.1). To determine the physical origin of the lack of hydrocarbon formation in the presence P-Pyr, we analyzed the C≡O stretch band of atop-bound CO (CO_{atop}) on the Cu electrode in the presence and absence of the films. As discussed in Chapter 3, CO_{atop} is an on-pathway intermediate in the electrochemical reduction of CO_2 [124, 148].

Figure 4.6 shows the representative C≡O stretch bands of CO_{atop} at a potential of -1.5 V for the three different interfaces. With no modification to the Cu interface, the lineshape of CO_{atop} is clearly asymmetric. The overall CO population can be well-described as a sum of two populations, represented by the sum of a broad and narrow Gaussian functions (Figure 4.6, green lines). The narrow band at ≈ 2070 cm^{-1} is a result of CO_{atop} adsorbed on undercoordinated Cu sites (step and kink sites), while the broad band at ≈ 2040 cm^{-1} is attributed to CO_{atop} adsorbed on comparatively more highly coordinated Cu sites (terrace sites) [31]. For clarity, we will refer to the narrow band at ≈ 2070 cm^{-1} as the high frequency band (HFB). It is important to note that the integrated band areas of the individual bands are not directly proportional to the relative population of CO_{atop} on the two different types of sites. The large amplitude of the HFB relative to the broad band can be a manifestation of intensity-borrowing due to dynamical dipole coupling [198–200].

Compared to the unmodified Cu/electrolyte contact, the C≡O stretch frequency and lineshape of CO_{atop} with the T-Pyr-modified interface is relatively unchanged. This observation demonstrates that the T-Pyr film does not substantially alter the chemisorption of CO on Cu. In stark contrast, the HFB is virtually absent in the presence of the P-Pyr-

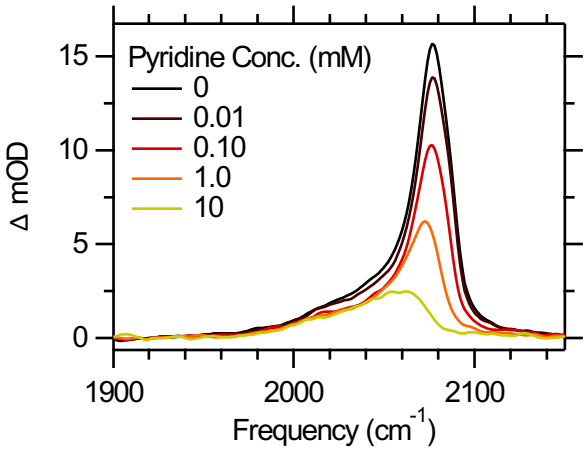

Figure 4.7: Evolution of the C≡O stretch bands as a the concentration of pyridine in the electrolyte increases while the potential is maintained at -1.3 V in CO saturated electrolyte.

modified interface. This suggests that P-Pyr may partially block CO adsorption sites. We hypothesized that the nitrogen atom with an available electron lone pair unique to P-Pyr may compete with CO for adsorption sites.

The absence of the HFB in the presence of P-Pyr is most likely caused by two possible mechanisms: (1) P-Pyr may broadly bind to a mixture of Cu sites, lowering the overall CO_{atop} coverage. Under low-coverage conditions, dynamical dipole coupling is weak and the signal borrowing intensity may prevent the observation of the HFB. (2) P-Pyr may preferentially bind to the relatively undercoordinated Cu sites, thus blocking CO adsorption on these specific sites.

We tested the first hypothesis by monitoring the C≡O stretch frequency at the unmodified Cu/electrolyte contact at a fixed potential as a function of coverage. This was done by saturating the electrolyte with CO_2 and maintaining the potential to generate CO_{atop}. The gas was then switched to Ar, continuously lowering the coverage of CO_{atop} . Even at a CO_{atop} coverage at $\approx 1/5$ the amplitude observed at saturation coverage, the HFB is still clearly observable. Therefore, an indiscriminately lower coverage of CO_{atop} cannot solely

account for the absence of the HFB with P-Pyr.

The second hypothesis was tested by conducting an experiment in CO-saturated electrolyte and observing how pyridine in the electrolyte impacted the CO population. Like P-Pyr, pyridine also possesses a nitrogen atom with an electron lone pair, but does not reductively form an organic film on the surface. Further, it similarly suppresses hydrocarbon formation [69]. To test the effect of pyridine on CO adsorption, a potential of -1.3 V was applied to the Cu electrode, saturating the surface with CO. Then, pyridine was added to the electrolyte in a stepwise manner and its impact on the C≡O stretch lineshape of CO_{atop} monitored. Figure 4.7 demonstrates that increasing the concentration of pyridine in the electrolyte is detrimental to only the HFB, decreasing and eventually disappearing completely. The final C≡O stretch spectrum with 10 mM pyridine is similar to that observed in the presence of P-Pyr, suggesting that both additives similarly impact CO adsorption. Taken together, these observations suggest that pyridine and P-Pyr selectively poison undercoordinated Cu sites.

Interestingly, even though a significant population of CO_{atop} remains on the electrode with P-Pyr and pyridine, no significant formation of hydrocarbons is observed during CO_2 reduction (Table 4.1). This observation is to the best of our knowledge, the first spectroscopic evidence that undercoordinated Cu sites are the more catalytically active sites in the reduction of CO to hydrocarbons. This conclusion is consistent with prior and more recent reports [38, 108, 128, 201].

4.3 Conclusions

In this chapter, we investigated the effects of two N-substituted arylpyridinium derivatives on the electrocatalytic properties of the Cu/electrolyte interface during CO_2 reduction. We showed with SEIRAS that the unique morphology of the organic film derived from

T-Pyr increases the local surface pH even at modest current densities (< 5 mA cm^{-2}) as evidenced by the appearance of a significant population of solution-phase carbonate (CO_3^{2-}) in the vicinity of the electrode. This increase in local pH is not achieved under even greater current densities where interfacial proton consumption occurs in the presence of the P-Pyr modified and unmodified Cu electrode. Taken together, the T-Pyr film is uniquely able to impede mass transport and buffering to/from the Cu surface. This results in a lower availability of protons for H_2 and CH_4 formation, while minimally impacting $C_{\geq 2}$ hydrocarbon production rates in the presence of this film. While P-Pyr also forms an organic film, it significantly impacts the adsorption of CO_{atop}. With the use of a molecular analogue pyridine, we were able to show that N-heterocycles with an electron lone-pair can selectively poison undercoordinated sites, thereby blocking CO adsorption on these sites. This results in the prevention of further hydrogenation of adsorbed CO to hydrocarbons. On this basis, these more undercoordinated sites are implicated as the active sites for CO_2 reduction to hydrocarbons.

4.4 Experimental Procedures

Materials 1-(4-pyridyl) pyridinium chloride hydrochloride (TCI Chemicals, >98%) and pyridine (Fisher Chemical, >99%) were used as received. 1-(4-tolyl) pyridinium chloride was synthesized from 1-(2,4-dinitrophenyl)pyridinium chloride (Oakwood Chemicals, 97%) and p-toluidine (Sigma Aldrich, 99%) according to reported microwave-assisted methods and purified with silica flash chromatography [202]. $KHCO_3$ ($\geq$99.98%) was obtained from Sigma Aldrich. High purity water (18.2 MΩ cm) was sourced from a Barnstead Nanopure Diamond system and used for all experiments. CO_2 (research grade) and Ar (ultra high purity) were procured from Air Gas.

SEIRAS Measurements SEIRAS experiments were carried out in a custom two-

compartment glass/polyetheretherketone (PEEK) cell (Addendum, FigureA4.5) equipped with stirring capabilities [191]. The cell was placed into a horizontally mounted ATR Accessory (VeeMax III; Pike Technologies; Madison, WI). The cell was equipped with a Ag/AgCl reference electrode (3 M NaCl; Basi Inc.; West Lafayette, IN) and a graphite rod counter electrode (99.995%; 3 mm thick; Sigma Aldrich). The potential was manipulated with a Versastat 3 potentiostat (AMETEK; Berwyn, PA). The solution resistance was measured with the Versastudio software and compensated by 85% for all measurements. The Cu thin film preparation, spectroscopic methods, and electrochemical methods were previously described in Chapter 3, Experimental Procedures.

4.5 Addendum

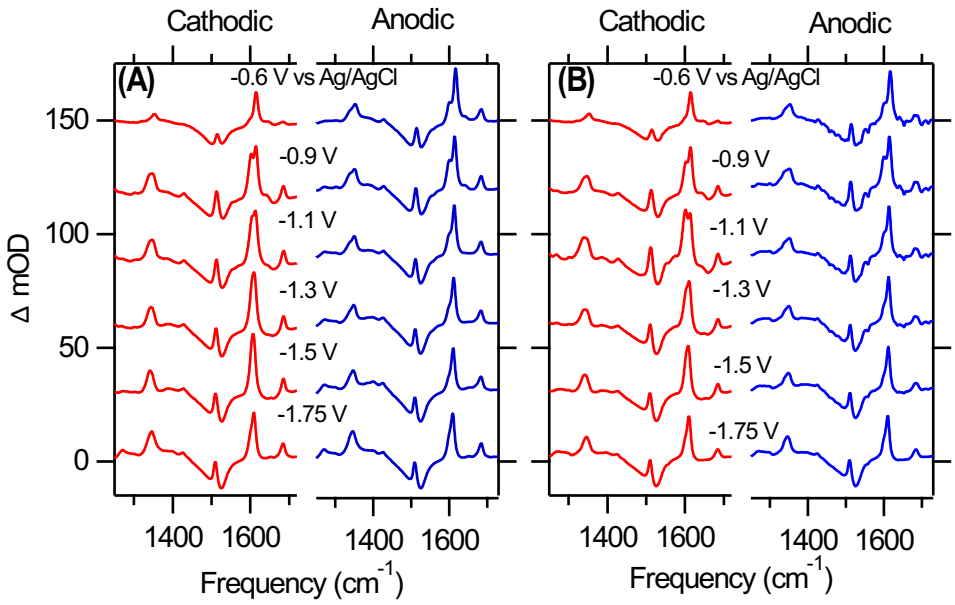

Figure A4.1: (A) IR spectra of the Cu/electrolyte interface in the presence of 10 mM P-Pyr in CO_2-saturated 0.5 M $KHCO_3$ during the CV in Figure 1 of the main text and (B) a repeated experiment. The main organic film features at 1610 and 1511 cm^{-1} are consistent with the ring stretch of the pyridyl moiety of the film dimer. A reversibly appearing peak at 1599 cm^{-1} that reaches the maximum intensity at ≈ -1.1 V is attributed to pyridinium ions that adsorb/desorb or change their orientation.

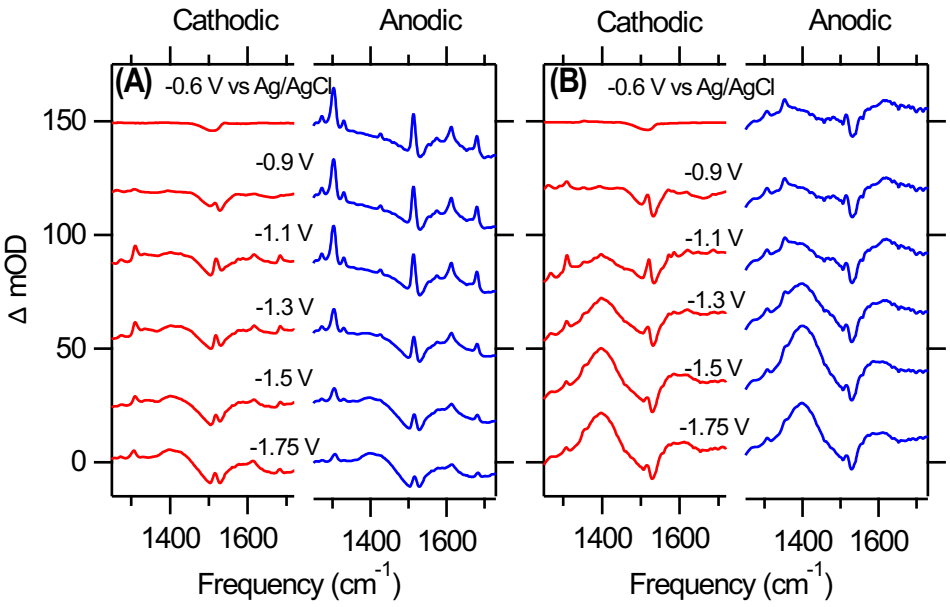

Figure A4.2: (A) IR spectra of the Cu/electrolyte interface in the presence of 10 mM T-Pyr in CO_2-saturated 0.5 M $KHCO_3$ during the CV in Figure 1 of the main text and (B) a repeated experiment.

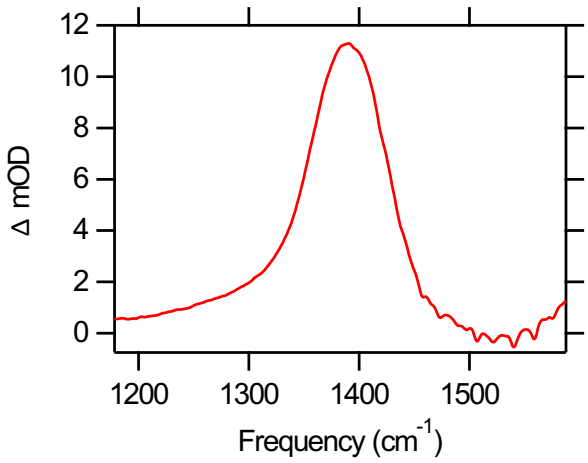

Figure A4.3: IR spectrum of a 10 mM aqueous solution of K_2CO_3. The spectrum of pure water served as the reference spectrum.

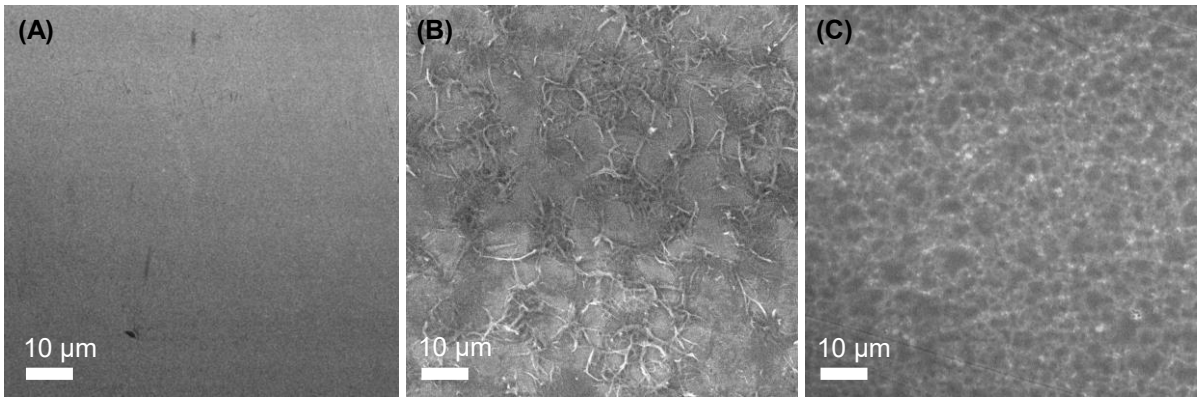

Figure A4.4: SEM images of Cu foils. (A) Pristine copper surface, (B) P-Pyr-derived film on Cu, (C) T-Pyr-derived film on Cu. The organic films were deposited during a CV under conditions as those employed for SEIRAS (Figure 2 of the main text). The films were deposited on a 1 cm^2 Cu foil. After removal of the electrode from the catholyte, the films were rinsed with deionized water, gently dried with N_2, and placed into a N_2-flushed container before SEM images were taken. A JEOL JSM-6340F Scanning Electron Microscope was used for all measurements.

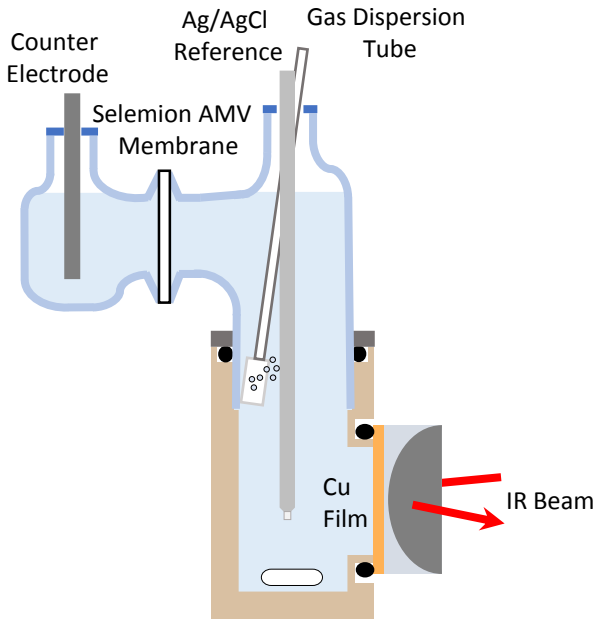

Figure A4.5: Depiction of the custom-built two-compartment cell setup[191]. The catholyte and anolyte were filled with 17 and 10 mL of 0.5 M $KHCO_3$, respectively. The catholyte was purged with 5 SCCM gases through a fin-porosity gas dispersion tube to ensure quick saturation of gases in the electrolyte. Before each experiment, the Cu surface was cleaned and the roughness factor determined with CVs as reported in Chapter 3, Experimental Procedures. Before each experiment, the Cu surface was fully reduced by cycling the potential between -0.6 V and -1.2 V, and without going back to open circuit, holding the potential at -0.6 V for 20 minutes while purging the gas of interest. After 20 minutes, the reference spectrum was collected and subsequently 0.5 mL of the aqueous electrolyte containing T-Pyr or P-Pyr was added to the catholyte. The potential was maintained for two more minutes at -0.6 V to allow the additives to disperse into the electrolyte. This was immediately followed by the electrochemical experiment.

4.6 Acknowledgements

We acknowledge the financial support received through a CAREER award from the National Science Foundation (award no.:CHE-1847841). V. J. O. expresses gratitude to Xinyu Yang and Chet Tyrol for help with synthesis and purification steps. V. J. O. would also like to thank Wei-Shang (Victor) Lo for his help with SEM measurements.

4.7 Original Publication

This chapter has been published: Ovalle V. J., & Waegele, M. M, *J. Phys. Chem. C* **123**, 24453–24460 (2019).

Chapter 5

Impact of Electrolyte Anions on the Adsorption of CO on Cu Electrodes

5.1 Introduction

In the electrochemical conversion of CO_2 to hydrocarbons on Cu electrodes, the rate-limiting step is the further reduction of the population of surface-adsorbed CO (CO_{ads}) on the electrode surface [31, 136, 148, 203, 204]. It is the intermediate binding energy of CO_{ads} on Cu that allows comparatively high rates of hydrocarbon formation not observed on any other pure metal electrodes [205, 206]. The adsorption energies of atop bound CO on the (111) facets of Au and Pt, for example, are respectively 0.04 and 1.45 eV [207]. This results in the desorption of CO_{ads} on Au electrodes rather than further reduction and the poisoning of Pt during CO_2 reduction conditions [205, 206]. However, the binding energy on CO on Cu(111) sites at 0.62 eV [207], falls in a relatively intermediate strength and coverage during CO_2 reduction conditions. This enables the co-adsorption of hydrogen, [144, 197, 206] and therefore the further reduction of CO_{ads} at significant rates [205, 208]. Regardless, to achieve these rates requires a substantial overpotential ($\approx$ 1 V), resulting in the excess of the parasitic side reaction of hydrogen evolution and poor product selectivity [205]. In optimizing the selectivity and catalytic performance of C_2 reduction on Cu, it is critical to determine the molecular underpinnings of the adsorption of CO on

Cu electrodes under low overpotential conditions.

The adsorption of CO on an electrode surface can be modulated through the coordination environment of exposed surface atoms through roughening or alloying of the surface [108, 209–213]. For a given metal surface, the adsorption energy is not a static value, but is sensitive to the coverage and identity of the adsorbed species. As shown in Figure 1.1 of chapter 1, there are many species that may directly interact with the electrode surface. The sensitivity of CO coverage on adsorption energy has been previously demonstrated on Pt(111), dropping by a factor of two when the coverage shifts from $1/4$ to a single monolayer [214]. Similarly, the presence of co-adsorbates can substantially affect CO adsorption energies and possibly block adsorption sites [215–218]. During CO adsorption on Cu, the components of the electrolyte make up the main co-adsorbates. Therefore, changing the components their concentrations in the electrolyte can be used to control the CO coverage and ultimately the catalytic activity and product selectivity.

Previous studies have suggested that it is specifically adsorbed anions from the supporting electrolyte that limit the adsorption of CO on Cu. With cyclic voltammograms (CV) on Cu electrodes, it was demonstrated that in the presence of specifically adsorbing anions in the CO saturated electrolyte, redox waves appeared [140, 142, 188, 219]. These charge transfer peaks were attributed to the desorption of specifically adsorbed anions during the adsorption of CO. This assignment was rationalized with the help of *in situ* infrared (IR) spectroscopic measurements: the C≡O stretch band area of CO_{atop} was correlated with the charge of the redox peak and inversely correlated with the bands of interfacial carbonate [70, 220] and phosphate [188] of the electrolyte as the potential was scanned negatively.

These foundational studies established a relationship between the desorption of anions and the adsorption of CO on Cu electrodes. However, the scope of these earlier studies was relatively limited because the effect of relative CO coverage and anion concentration

were not investigated fully. While the characterization of the redox peak during CVs was studied with a large variety of electrolyte anions and concentrations, the coverage of CO investigated with IR spectroscopy was only reported in perchlorate [219], phosphate [188], and carbonate [70, 140] at concentrations limited to 0.1-0.2 M. While the anion identity and concentration may influence the potential-dependent CO coverage, the formation of a CO adlayer intrinsically alters the properties of the electrode interface [31, 221, 222]. An in depth study systematically determining the relationship between anion identity, concentration, and CO coverage is thus lacking. We address this key issue in this work.

Here, we employed SEIRAS to investigate the effect of anion concentration and identity on the adsorption of CO on polycrystalline electrodes. With this technique, we surveyed the potential dependent C≡O stretch frequency and band area with 10 mM and 1 M aqueous solutions of NaCl, Na_2SO_4, and $NaClO_4$. In 10 mM electrolytes, the adsorption and desorption of CO with electrode potential are found to be insensitive to the identity of the anion in the supporting electrolyte. At 1 M Na_2SO_4 and $NaClO_4$, the saturation coverage of CO reaches $2/3$ of what is observed in 10 mM electrolytes. This is indicative of site blocking effects by the quasi-adsorbed anions. In every electrolyte except 1 M NaCl, a hysteresis is observed between the adsorption and desorption of CO during the CV. We attribute this hysteresis to the increased stability of the CO adlayer during the reverse scan induced by a CO-driven reversible reconstruction of the electrode surface. We attribute the lack of hysteresis in the 1 M NaCl electrolyte to the co-adsorption of Cl^- anions and subsequent decrease in the adsorption energy of CO. The decrease in adsorption energy due to Cl^- co-adsorption is manifested in a substantial blue-shift in the C≡O stretch frequency of CO_{atop} compared to the other electrolytes. Further, the relative concentration of the anions can be tracked near the electrode surface with the O-H stretch of the anion hydration-shell. At 1 M, Cl^- is the only anion that does not have a significant hysteresis during the CV, indicating its interplay with CO. However, the initial onset of CO adsorp-

tion was similar for the different electrolytes. Overall, the anion identity and concentration can significantly influence the coverage of adsorbed CO on Cu electrodes, but minimally impact the effective onset potential for CO adsorption.

5.2 Results and Discussion

Choice of Electrolytes. To investigate the interdependence of CO adsorption with anions of the supporting electrolyte, we carried out SEIRAS in the attenuated total reflectance (ATR) configuration on chemically deposited polycrystalline Cu electrodes. During these experiments, the electrolyte was continuously purged with CO and stirred. The electrolytes chosen for this experiment were 1 M and 10 mM aqueous solutions of NaCl, Na_2SO_4, and $NaClO_4$. The anions in the supporting electrolyte were chosen on the basis of different interactions with the Cu surface to all, allowing us to describe a range of anion-Cu interactions and their effect on the adsorption of CO. Prior studies have found that SO_4^{2-} and Cl^- can specifically adsorb on Cu [223–225], whereas ClO_4^- can only physisorb on Cu electrodes [224]. As these solutions are not buffered, D_2O was chosen as the solvent rather than H_2O. This is a result of the kinetic isotope effect minimizing the Faradaic current resulting from hydrogen evolution [226]. Therefore, the production of hydroxide during hydrogen evolution is limited. Despite this, the pH of the bulk electrolyte increased from 7.1 to 10.1 in the course of each experiment. However, previous work indicates that the adsorption of CO on Cu is insensitive to the pH in this range[136].

Impact of Anions on CO Adsorption. Plotted in Figure 5.1 is the C≡O stretch spectra of CO_{atop} as a function of potential during a CV with nominal turning potentials of -0.6 to -1.4 V versus Ag/AgCl in 10 mM $NaClO_4$ solution. In this chapter, unless otherwise specified, all potentials will be reported against the Ag/AgCl electrode. With the 10 mM concentration electrolytes of Na_2SO_4 and NaCl, a similar potential dependent CO

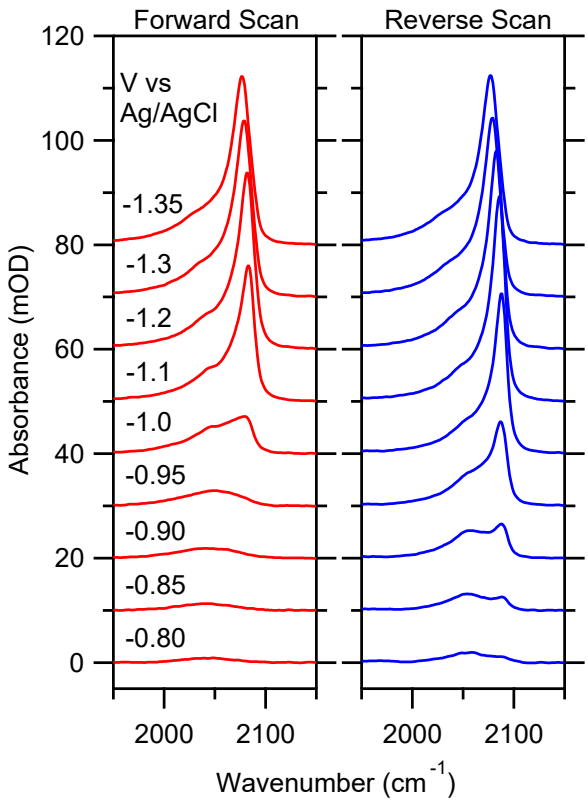

Figure 5.1: Representative C≡O stretch spectra of CO_{atop} on Cu as a function of applied potential during the cathodic forward (red) and anodic reverse scans (blue) in 10 mM $NaClO_4$ in D_2O. The reference potential used was -0.6 V.

adsorption profile is observed (Addendum, Figure A5.1). Further analysis of this spectra relies on multiple assumptions that are justified in prior work: at a scan rate of 2 mV s^{-1}, a pseudo-steady state CO population is achieved [136], and the integrated band area under of the C≡O stretch band is approximately proportional to the surface coverage [136, 140, 142]. The latter may be partially impacted by deviations from Beer's law at high CO surface coverage resulting from dynamical dipole coupling [199].

By integrating the C≡O stretch band area in the different electrolytes, the effect of the anion identity on the potential dependent CO_{atop} coverage is observed. Figure 5.2A show such analysis in the 10 mM solutions of the sodium electrolytes. In this figure, the forward scans are represented by reddish traces and the reverse scans by bluish ones. Between the

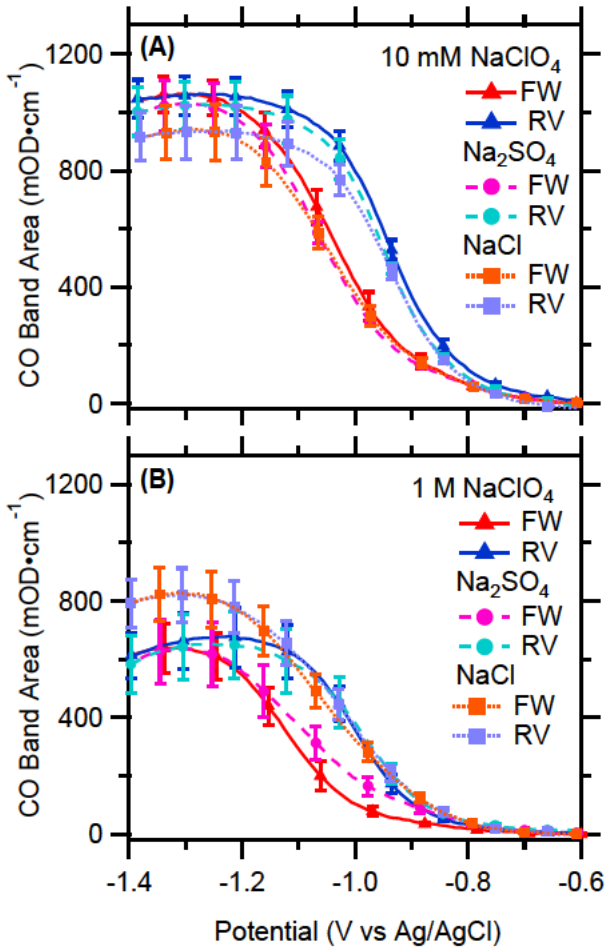

Figure 5.2: Integrated C≡O stretch band areas of CO_{atop} on Cu as a function of applied potential with the indicated (A) 10 mM and (B) 1 M electrolytes. FW and RV refer to the forward and reverse scans, respectively. Error bars represent the standard errors from an average of at least three independent experiments.

different electrolyte anions, there is almost no difference in both the potential dependence and magnitude of the integrated band areas. Interestingly, the CVs demonstrate a clear hysteresis between the forward and reverse scans, with the latter shifted anodically by $\approx$ 95 mV. This hysteresis is not due to irreversible changes in the electrode structure, as the hysteresis is also observed in a second consecutive CV (Addendum, Figure A5.2). The hysteretic behavior is the result of a reversible interfacial process.

In the 1 M electrolytes (Figure 5.2B), there is a clear dependence of the electrolyte

anion and the potential dependent CO_{atop} coverage. The differences between the 1 M and 10 mM electrolytes manifest in the saturation coverage and potential dependence. In the presence of 1 M ClO_4^- and SO_4^{2-}, the band area saturation coverage is $\approx 35\%$ lower than in the corresponding 10 mM electrolytes. This suggests that these anions are able to partially block CO adsorption sites. This is counter-intuitive, as the ≈ -1.3 V potential applied to saturate the Cu surface with CO is approximately 0.4 V more negative than the potential of zero charge (PZC) of polycrystalline Cu (-0.93 V in $NaClO_4$ under acidic pH conditions) [227], and should electrostatically repulse the anions. This suggests that an interaction is occurring between the anions and the electrode. However, SO_4^{2-} and ClO_4^- are not expected to specifically adsorb on Cu electrodes at this potential range, [224] precluding a direct chemical interaction.

While a direct interaction is unlikely, the electrolyte anions may still interact with an electrode mediated by another species. With an applied electrode potential of ≈ -1.3 V, the Na^+ cations are the predominant charged species in the double layer. It has been demonstrated with density functional theory (DFT) studies that alkali metal cations can specifically adsorb on Cu and other metal electrodes in this potential range [72, 228]. Further, surface-enhanced Raman (SERS) studies have observed that the specific adsorption of phosphate anions on Ag electrodes is stabilized under cathodic polarization in the presence of alkali cations in the electrolyte [229]. On the basis of our observations and these prior investigations, we attribute the blocking effects to anions that are quasi-specifically adsorbed, mediated by Na^+.

It is relevant to note that in a previous study, the onset potential for CO adsorption on Cu(100) electrodes was reported as more positive in ClO_4^--containing electrolyte compared to electrolytes containing specifically adsorbing anions. In this study, we define the onset potential where the integrated band area reached $\approx 1\%$ of the saturation coverage. As such, the onset potential observed in Figure 5.2 with our polycrystalline Cu electrode

is between -0.65 and -0.7 V, despite the differences in cation identity and concentration. As the interaction of electrolyte species with an electrode surface can significantly depend on the morphology of the electrode [23, 230, 231], we attribute the difference in our observation with the differing electrode surface facets.

Another key difference observed in Figure 5.2, with 1 M Cl^-, the saturated CO coverage only decreases by $\approx 12\%$ compared to that in 10 mM Cl^-. This indicates that the in contrast to ClO_4^- and SO_4^{2-}, Cl^- does not block the CO adsorption sites in a significant manner.

Finally, the hysteresis observed between the forward and reverse scans is uniquely absent in the 1 M NaCl electrolyte. Specifically, in desorption of CO in the reverse scan is shifted to more cathodic potentials in this electrolyte. The presence of a hysteresis for an adsorbed species like CO can emerge due to irreversible changes at the electrode interface. These irreversible changes can result from surface reconstruction and an increase in the interfacial pH due to reduction reactions. To see if the hysteresis is due to one of these irreversible processes, we carried out a consecutive CV to see if the potential dependent adsorption of CO returns to its initial potential dependence. Demonstrated in Figure A5.2 of the Addendum, with both 10 mM and 1 M Na_2SO_4, the consecutive CVs had overlapping CO adsorption and desorption profiles. This observation and the lack of substantial change in the Cu electrode surface roughness indicates that the hysteresis is not the result of an irreversible change in electrode structure during the CV, but is rather reversibly tied to the CO coverage and a general feature of the Cu/Electrolyte interface. Our results agree with previously reported hysteresis in CO adsorption behavior both the C≡O stretch band areas of CO_{atop} on Cu and the redox peaks that have been tied to the desorption of anions in the presence of CO on Cu [136, 188].

To understand the pronounced absence on the hysteresis in CO_{atop} adsorption and desorption on Cu with 1 M NaCl, we first need to understand what is the origin of the hys-

teresis in the CVs.

Origin of the Hysteresis. The hysteresis observed with the integrated C≡O stretch band areas of CO_{atop} can emerge from a number of different explanations. In a similar case, IR bands at the ionic liquid/electrode interface encountered potential dependent hysteresis [232]. This was attributed to the activation barrier associated with rearranging the ionic liquid components at the electrode surface. Due to the observation of a similar hysteresis with multiple different anions in a wide concentration range, we believe that the rearrangement of these species with potential is not the underlying explanation for the hysteretic behavior. It is more likely that the formation of the CO_{atop} adlayer is the driving force for the hysteretic behavior. Prior reports help support this claim: DFT studies have demonstrated that the CO binding energy is strongly related to the surface coverage of CO [206, 214, 233]. In a specific example, on Pt(100) surfaces, the chemisorption energy of CO_{atop} lowers from 1.8 to 1.16 eV as the coverage goes from 1/4 to one monolayer [214]. This change in binding energy is primarily a result of repulsive interactions between neighboring CO_{atop} molecules [214]. The decrease in binding energy with coverage is generally observed with CO at the vacuum/metal interface [206, 214, 233]. While there is a correlation observed with CO coverage in this prior work, it trends in the opposite direction of CO binding energy. We observe that the desorption of CO shifts to more positive potentials (Figure 5.2), suggesting that CO_{atop} is increasingly stabilized with its increasing coverage on polycrystalline Cu. This indicates that the CO coverage alone does not lower the binding energy, but contributes to another factor that modulates its binding energy. It's been observed that under a variety of conditions where CO adsorbs on a metal surface, it can alter the surface structure [41, 82, 234, 235]. This is in contrast to the DFT studies where the surface structure is invariant to the CO coverage.

The adsorption of CO can induce changes in the morphology of metal surfaces [41, 82, 234, 235]. We have previously demonstrated with the same SEIRAS technique with poly-

crystalline Cu electrodes, CO adsorption can drive a reconstruction that renders the further adsorption of CO as more favorable [31]. This was further corroborated with SERS experiments. CO adsorption induces a reversible surface reconstruction that increases the density of relatively more undercoordinated Cu surface sites that bind to CO more strongly. Taken together, we posit that these stronger CO binding sites that are only significantly present at sufficient CO coverages result in the observed hysteresis in the reverse scan of the CV (Figure 5.2). This is in agreement with studies observing a hysteresis attributed to CO-induced reconstruction at the gas/Pt(100) interface during CO adsorption/desorption as a function of temperature [234]. Likewise, a reversible reconstruction induced by CO adsorption has been observed on Au(100) electrodes in alkaline electrolyte [221]. Therefore, we suggest that the hysteresis observed with the C≡O stretch band areas of CO_{atop} are primarily attributed to the CO-induced reconstruction of the surface.

Interplay of CO_{atop} and Anions. To gain a greater insight into the interplay between the formation of the CO_{atop} adlayer and the anions of the electrolyte, we monitored the local changes in anions concentration as a function of applied potential. Due to the IR-invisible nature of Cl^- and the limited spectral window disallowing the observation of the vibrational modes of ClO_4^- and SO_4^{2-}, we monitored the hydration shells of the anions. We would be remiss if we did not specify that this is looking at the anions in the bulk of the electrochemical double layer; we cannot differentiate between specifically adsorbed or anions not directly in contact with the electrode surface.

Plotted in Figure 5.3 is the IR spectra in the $2500-2850$ cm^{-1} region in the 1 M electrolytes and at a sample potential of -1.2 V. Here, the potential-dependent spectra are due to the changes in O−D stretch of interfacial D_2O. We observe a biphasic feature with a positive component at $\approx$ 2710 cm^{-1} and a negative component at $\approx$ 2660 cm^{-1}. The band at $\approx$ 2710 cm^{-1} has been previously assigned to interfacial D_2O that is hydrogen bonded with surface adsorbed CO [25]. The negative band at $\approx$ 2660 cm^{-1} has been

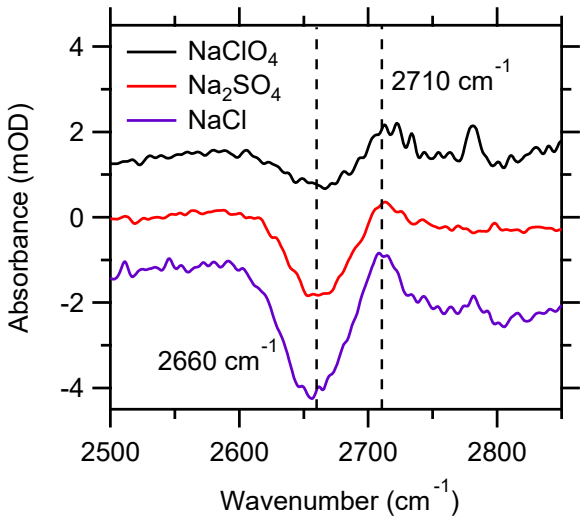

Figure 5.3: Representative O−D stretch spectra at a potential of -1.2 V in the 1 M electrolytes as indicated. The reference potential used was -0.6 V.

previously demenostrated to be due to the water in the hydration shell of the anions in the bulk electrolyte [236, 237]. This feature is observed as a negative band as the IR spectra here are difference spectra. As the potential is tuned negative, anions and their hydration shells are displaced from the interface. It should be noted that the band at 2660 cm^{-1} may not be solely from hydration shells of anions. For example, with NaCl, it may be the solvation environment around specifically adsorbed $Cl^{\delta-}/Na^{+}$ pairs [238]. This band could only be observed in 1 M electrolytes as the signal was too low in 10 mM electrolytes. To obtain a numerical value for the local anion concentration related to this band, we fit the 2500−2850 cm^{-1} region with a linear background and two Gaussian functions.

Shown in Figure 5.4 is the normalized 2660 cm^{-1} band area (right y-axis, dashed lines) in direct comparison to the normalized C≡O stretch band area (left y-axis, solid lines) as a function of potential with each anion. As previous studies correlated the adsorption of CO on polycrystalline Cu electrodes with the desorption of specifically adsorbed phosphate and carbonate anions [70, 188, 220], we wanted to observe if a similar process occurs with these different anions. Figure 5.4 reveals a more complicated relationship between inter-

facial anions and CO_{atop}. Like prior observations with carbonate and phosphate [70, 188, 220], in the presence of ClO_4^- and Cl^-, the rise of the integrated band area of C≡O stretch can be correlated with the decrease in the integrated 2660 cm^{-1} band area associated with these anions (Figure 5.4A, C). The band associated with SO_4^{2-} appears to decline at potentials more positive than -0.9 V (Figure 5.4B), possibly from the higher charge density this anion carries over the other two.

In the reverse scan, SO_4^{2-} and ClO_4^- repopulate the interface at a steeper rate in comparison to their initial rate of depletion. The hysteresis also occurs in the consecutive CV (Addendum, Figure A5.3). However, if the populations of anions and CO_{atop} are believed to replace each other as a function of potential, the coverage of CO_{atop} should be destabilized during the reverse scan. We did not observe this. This demonstrates that the stabilization of the CO_{atop} adlayer by CO-induced reconstruction is strong enough to prevent the desorption of CO by ClO_4^- and SO_4^{2-} as the potential is scanned positively.

Like the CO_{atop} band, in the presence of 1 M Cl^-, virtually no hysteresis is observed in the 2660 cm^{-1} integrated band area (Figure 5.4C). This band also appears to be inversely correlated with the growth of the C≡O stretch band area. These observations suggest that CO adsorption on Cu is affected by the presence of Cl^-.

Interaction of CO_{atop} and Cl^-. To probe the possible interactions between Cl^- and CO_{atop}, we compared the C≡O stretch band peak frequencies in the presence of the different electrolytes. In order to minimize complications due to frequency shifts arising from dynamical dipole coupling [62, 239], we restricted the C≡O stretch analysis to potentials (≥ -0.85 V) where the CO_{atop} coverage is low. Representative spectra of CO_{atop} spectra at an applied electrode potential of -0.85 V are plotted in (Addendum, Figure A5.4). By fitting this peak with a linear background fit and a single Guassian, the C≡O stretch band peak frequencies of CO_{atop} can be quantitatively compared in the different electrolytes. In the 10 mM electrolytes, the C≡O stretch frequencies between potentials of

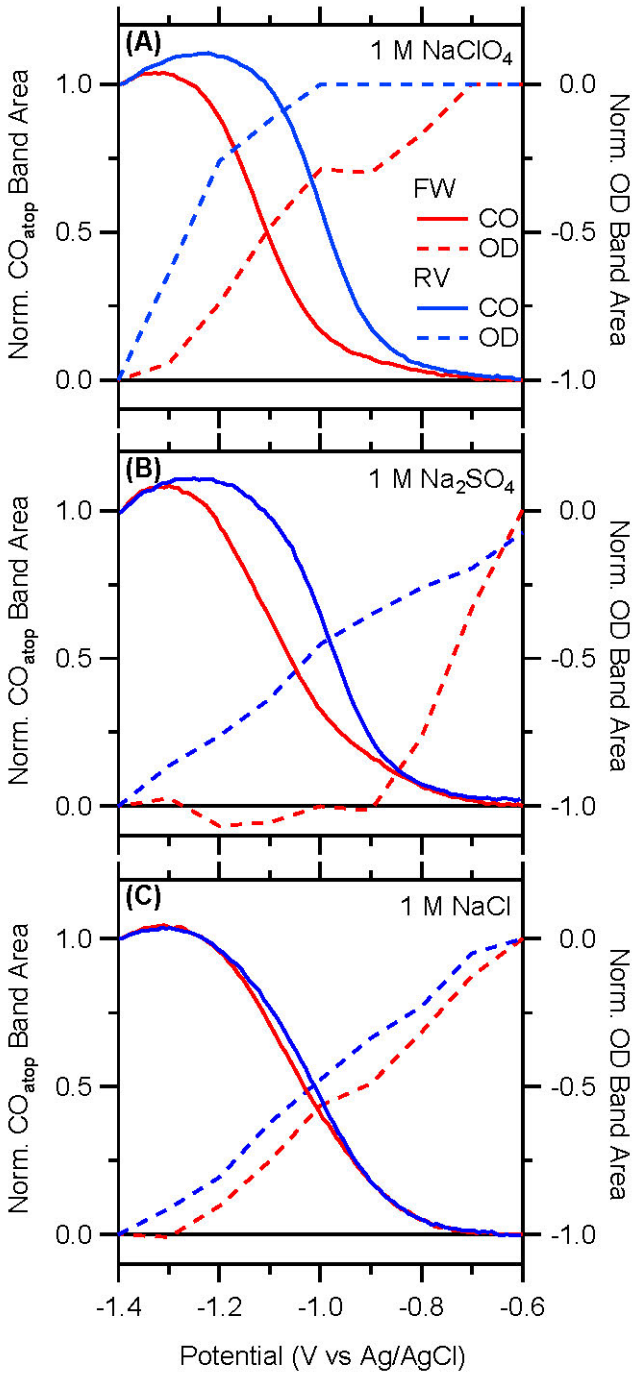

Figure 5.4: Normalized band areas of the C≡O stretch band (left y-axis) and 2660 cm^{-1} O−D stretch band (right y-axis) as a function of applied potential in 1 M solutions of (A) $NaClO_4$, (B) Na_2SO_4, and (C) NaCl.

-0.75 and -0.85 V are relatively similar regardless of anion identity (Addendum, Figure A5.5). Shown in Figure 5.5 are the C≡O stretch frequencies in 1 M anion electrolytes in the same potential range (-0.75 to -0.85 V), with the frequencies of 10 mM $NaClO_4$ as a reference. With respect to this reference, the stretch frequency in 1 M $NaClO_4$ is very similar. This is in contrast to 1 M SO_4^{2-} and Cl^-. In SO_4^{2-}, a moderate blue-shift of ≈ 5 cm^{-1} is observed with respect to 10 mM $NaClO_4$. With Cl^-, an even stronger blue-shift of ≈ 19 cm^{-1} is observed across the potential range. This trend in C≡O stretch frequency shift follows the increasing tendency of the anion to specifically adsorb on the Cu electrode surface ($ClO_4^- < SO_4^{2-} < Cl^-$) [223, 224]. These results further confirm that specifically adsorbed Cl^- ions modulate the interaction between adsorbed CO and the Cu surface. In contrast, SO_4^{2-} and ClO_4^- are expected to be quasi-adsorbed on the electrode at more negative potentials (< -0.85 V). This results in the lowering in saturation CO coverage in 1 M of these anions (Figure 5.2) due to site blocking by these anions and not the modulation of CO adsorption energy.

It has been shown at the vacuum/metal interface that some co-adsorbates can impact the binding energy and subsequently the C≡O stretch frequency of adsorbed CO [215, 216]. While these "ligand effects" can be the result of multiple mechanisms, they are often interpreted successfully in terms of the surface charge distribution among co-adsorbates and adsorbed CO molecules. In this case, the blue shift in the C≡O stretch mode can be described by the bonding competition of CO_{atop} with specifically adsorbed Cl^-. Specifically, less charge donation from the Cu surface to the π^* orbital of CO_{atop} occurs compared to the absence of specifically adsorbed Cl^-. With less charge back donation to the π^* orbital of CO_{atop}, a blue-shift in the C≡O stretch frequency is expected [216], consistent with the observations in Figure 5.5.

Less back donation to the π^* orbital of CO_{atop} is presumed to lower the overall binding energy of CO to the electrode surface [102]. This is expected on Cu, with DFT calculations

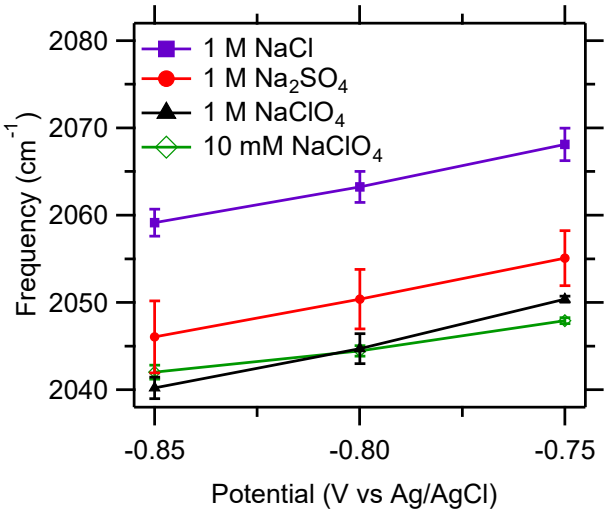

Figure 5.5: Peak frequencies of the C≡O stretch band as function of applied potential at low CO_{atop} coverage. Each trace is an average of a minimum of three independent experimental results. Error bars represent standard errors.

showing that the co-adsorption of I^- on Cu weakens the binding energy by 0.07 to 0.33 eV, depending on the crystallographic facet [72]. A smaller binding energy for CO_{atop} should lower the ability of CO-induced reconstruction, consistent with the observation of a lack of hysteresis with 1 M NaCl electrolyte (Figures 5.2 and 5.4C). This regulation of the CO_{atop} binding energy by Cl^- may partially explain the dependence of the product selectivity and/or rate of CO_2 reduction on the identity of the supporting electrolyte's halide anion [58–60, 240].

Prior computational [225, 241, 242] and experimental [243–245] studies have found that Cl^- desorbs from Cu electrodes at potentials more negative than ≈ -0.56 to -0.88 V versus Ag/AgCl, depending on the surface coverage and crystallographic facet. However, these experiments were typically carried out in low Cl^- concentrations in the electrolyte. With 1 M Cl^- in the electrolyte, a small coverage of Cl^- is expected to linger on the Cu electrode surface at much more negative potentials. Recent work has demonstrated that after 1 hour of CO_2 reduction in 0.1 M $KHCO_3$ + 0.3 M KCl at a potential of -1.0 V versus the reversible hydrogen electrode, small amounts of Cl^- remain on the surface [240].

Further, the magnitude of reduction current was linearly correlated to DFT calculations of the adsorption potential of the halide in the electrolyte. While halide-induced surface reconstruction has been demonstrated to take place on Cu, this has been suggested to not be the primary enhancement of CO_2 reduction with differently prepared Cu electrodes [57–61]. This further supports our notion that the Cl^- coverage on the electrode is sufficiently large enough to alter the binding energy of CO_{atop} even at the most negative potentials applied in this work (-1.4 V).

5.3 Conclusions

With SEIRAS, we investigated the degree that anions in the supporting electrolyte affect the adsorption of CO_{atop}, a key intermediate towards hydrocarbon production, on Cu electrodes. We achieved this by using anions with increasing tendencies to specifically interact with Cu ($NaClO_4$, Na_2SO_4, and NaCl) with a wide concentration difference (10 mM and 1 M). We found that at a concentration of 10 mM anions in the electrolyte, the adsorption of CO was virtually independent of anion identity. In contrast, the 1 M electrolytes resulted a dependence of the saturation coverage of CO on the anion identity. Interestingly, weakly and non-specifically adsorbing anions (ClO_4^- and SO_4^{2-}) limit the CO_{atop} saturation coverage. This suggests that quasi-specifically adsorb anions can block a fraction Cu sites for CO adsorption. However, this blocking effect is dependent on the CO_{atop} coverage, as observed with the hysteresis in the CO desorption shifted to more positive potentials. We posit that the this hysteresis is primarily due to the higher stability of the CO_{atop} adlayer driven by a CO-induced reversible reconstruction of the Cu surface [31]. In contrast, in 1 M NaCl, almost no hysteresis is observed in either the adsorption/desorption of CO_{atop} or in the anion depletion/enrichment profiles of hydrated Cl^- anion near the interface. The correlation between Cl^- and CO_{atop} coverage suggests that specifically adsorbed Cl^- im-

pacts the chemisorption of CO_{atop}. This is further supported by the distinct blue-shift in the presence of 1 M NaCl to all other electrolytes studied. The blue-shift is likely a result of the specifically adsorbed Cl^- weakening the CO adsorption energy, limiting the ability of CO to restructure the surface and therefore lack the hysteresis in the CO_{atop} potential-dependent profile. This work demonstrated that anions can play a significant role in the chemisorption of CO on Cu electrodes, leading to changes in the CO_2 reduction rates and selectivities. While the anions can impact CO chemisorption and block sites, the onset potential is surprisingly insensitive to anion identity and concentration. In order to carry out further reduction of CO and subsequently the adsorption of CO to more anodic potentials, other strategies than changing the electrolyte anions may be more effective.

5.4 Experimental Procedures

Materials Sodium chloride (99.999% trace metals basis) and Sodium perchlorate hydrate (99.99% trace metals basis) were aquired from Sigma-Aldrich. Sodium sulfate (99.9955% metals basis) was obtained from Alfa Aesar Puratronic. D_2O (99.8 atom% D) from Acros Organics was used in all experiments. CO (ultra high purity) and Ar (ultra high purity) were procured from Air Gas.

SEIRAS. SEIRAS experiments were carried out in a home-built two-compartment polyetheretherketone (PEEK) cell (Addendum, Figure A5.6 with the catholyte (6 ml) and anolyte (4 ml) separated by a Selemion AMV anion exchange membrane (AGC Engineering Co.; Chiba, Japan). The counter electrode was graphite rod (99.995%; Sigma Aldrich) and the reference an Ag/AgCl electrode (3 M NaCl; Basi Inc.; West Lafayette, IN). The catholyte was stirred at all times at 900 rotations per minute (rpm) with a magnetic stir bar. The cell was connected to a nitrogen-purged attenuated total internal reflection (ATR) accessory (VeeMax III; Pike Technologies; Madison, WI) in the sample compartment of

a Bruker Vertex 70 Fourier-transform infrared (FTIR) spectrometer, which was interfaced with a liquid nitrogen-cooled mercury cadmium telluride (MCT) detector (FTIR-16; Infrared Associates; Stuart, FL). The potential was controlled with a Versastat 3 potentiostat (AMETEK; Berwyn, PA). Details of the Cu chemical thin film deposition and spectroelectrochemical data collection were provided in Chapter 3. To clean the thin film electrode, the film was subjected to 5 CVs from -0.13 to -0.6 V versus Ag/AgCl at a scan rate of 50 mV s^{-1} under Ar purge at 5 standard cubic centimeter per minute (sccm). Following these cleaning CVs, the interfacial capacitance and solution resistance were measured. 85% of the solution resistance was compensated *in situ*. The remaining 15% was manually corrected following each experiment. To avoid potential complications due to Cu oxides and hydroxides, [246, 247] a CV was carried out from -0.6 to -1.2 V versus Ag/AgCl at 10 mV s^{-1} to remove residual surface oxides and hydroxides. Following this CV, the cell was never returned to open circuit until completion of the experiment. To saturate the electrolyte with CO, the gas purge was then switched from Ar to CO. CO was purged for 20 min at a flow rate of 5 sccm while the potential was maintained at -0.6 V. Then, the spectroscopic measurements were carried out during the CVs from -0.6 to -1.4 V versus Ag/AgCl at a scan rate of 2 mV s^{-1}. CO was continuously purged until completion of the experiment.

5.5 Addendum

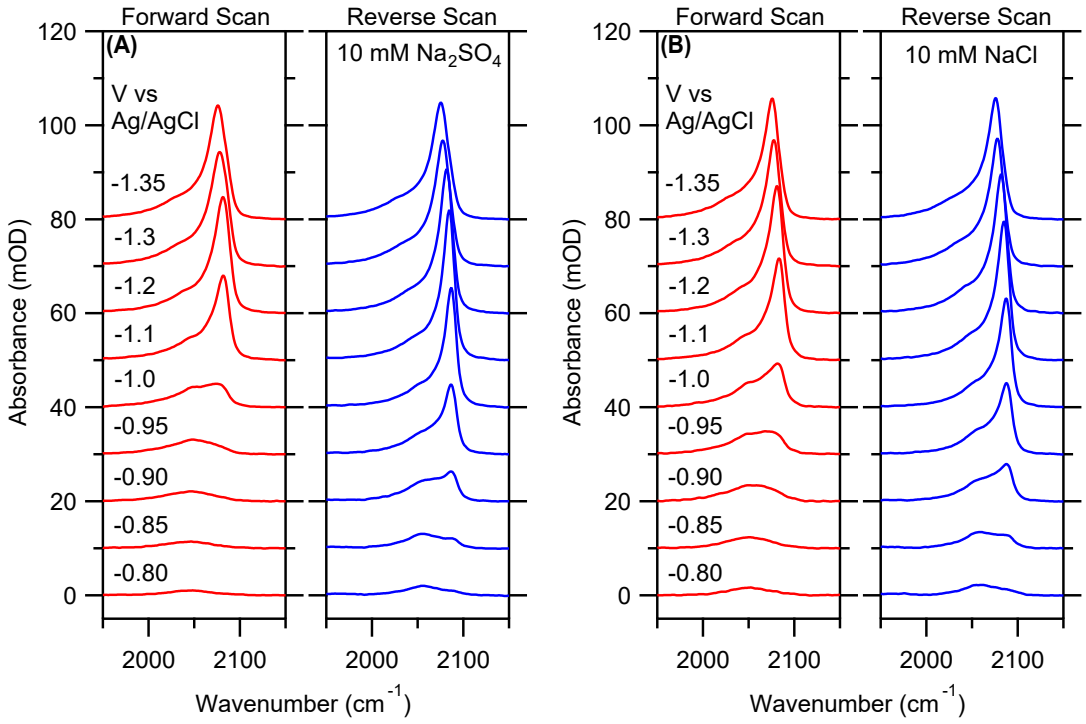

Figure A5.1: Representative C≡O stretch spectra of CO_{atop} as a function of applied potential during the cathodic forward (red) and anodic reverse scans (blue) in (A) 10 mM Na_2SO_4 and (B) 10 mM NaCl.

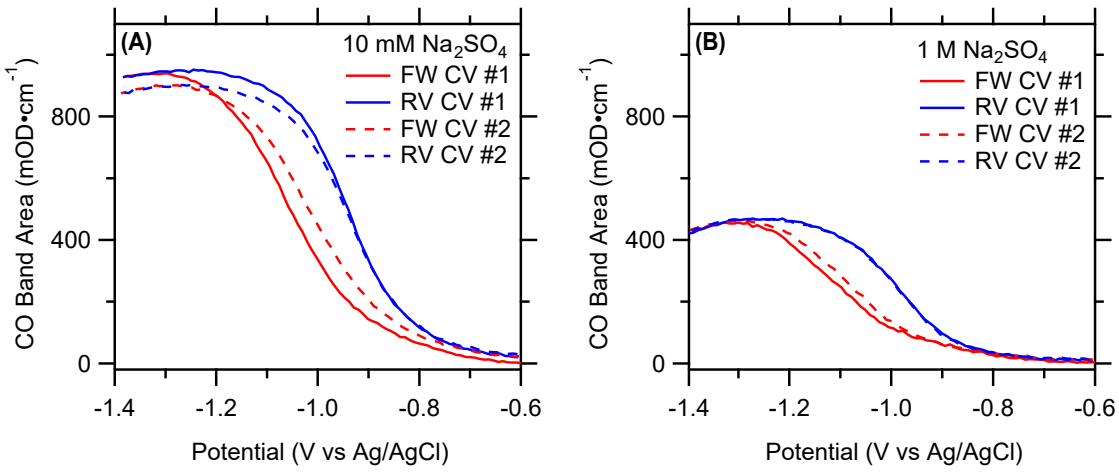

Figure A5.2: Integrated C≡O stretch band areas of CO_{atop} for two consecutive CVs in (A) 10 mM and (B) 1 M Na_2SO_4, with the second CVs indicated with dashed traces. FW and RV denote the cathodic forward and anodic reverse scans, respectively.

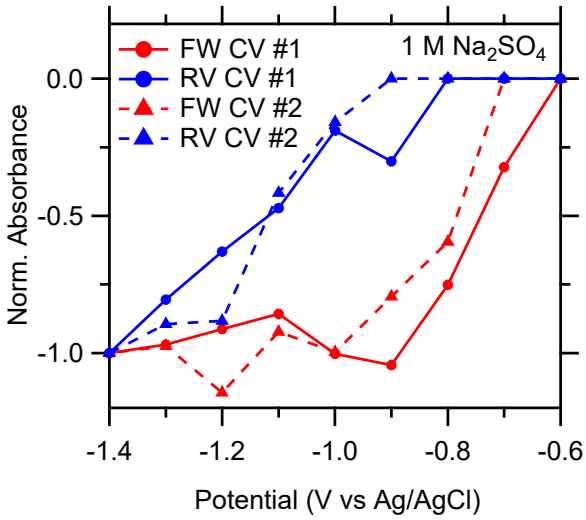

Figure A5.3: Normalized integrated 2660 cm^{-1} band areas for two consecutive CVs in 1 M Na_2SO_4. The dashed traces represent the second CV. The normalization constants were -33.89 and -12.87 mOD cm^{-1} for the first and second CVs, respectively.

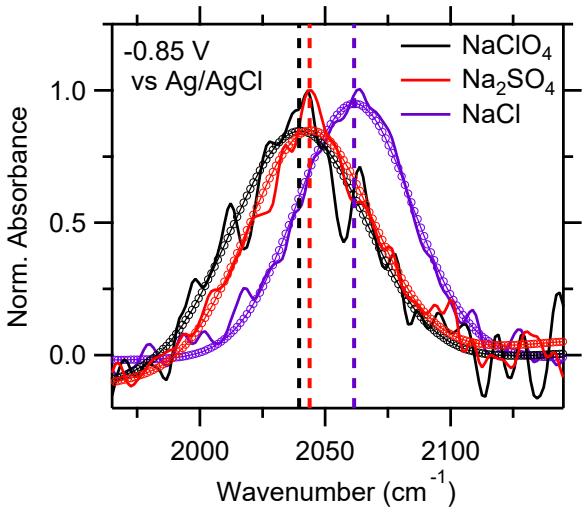

Figure A5.4: Representative C≡O stretch spectra in the indicated 1 M electrolytes. The dashed lines signify the C≡O stretch peak frequencies of the Gaussian fits (circles).

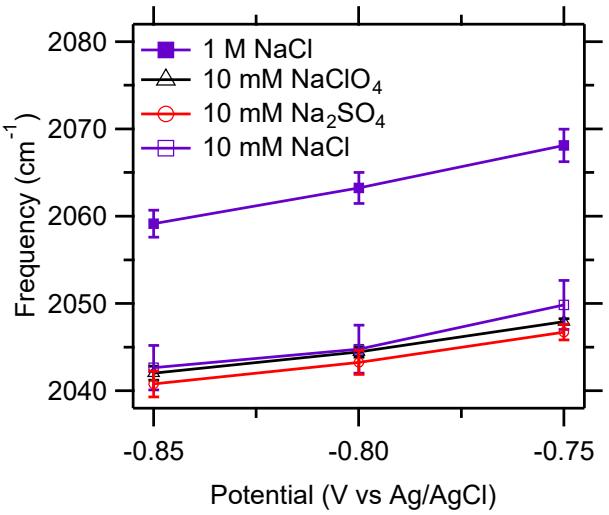

Figure A5.5: Peak frequencies of the C≡O stretch mode as function of applied potential at low CO_{atop} coverage in the 10 mM electrolytes. Each trace is an average of a minimum of three independent experimental results. The peak frequency in 1 M NaCl is shown for comparison. Error bars represent standard errors.

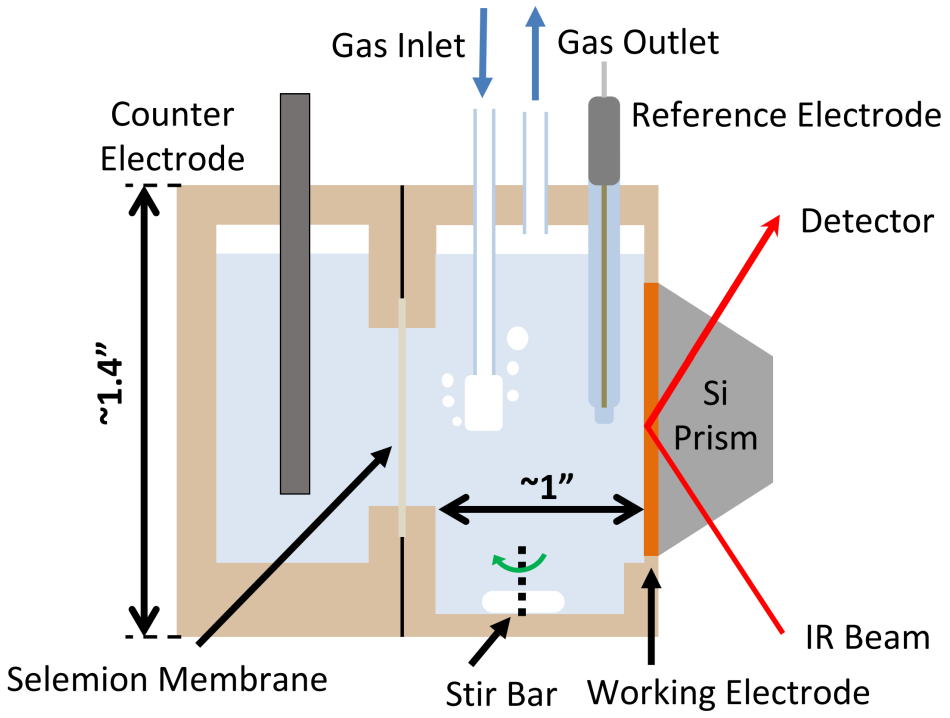

Figure A5.6: Depiction of the updated fully polyetheretherketope (PEEK) custom-built two-compartment cell [62] .

5.6 Acknowledgements

We acknowledge the financial support received through a CAREER award from the National Science Foundation (award no.:CHE-1847841).

5.7 Original Publication

This chapter has been published: Ovalle, V. J. & Waegele, M. M, *J. Phys. Chem. C* **124**, 14713-14721 (2020).

Chapter 6

Hydration Free Energies of Alkali Metal Cations Determine Their Surface Concentrations During CO_2-to-CO Conversion

6.1 Introduction

The electrochemical interface involves a complicated mixture of molecular components that can impact surface intermediates and the resulting electrocatalysis. The previous chapters have demonstrated the utility of surface enhance infrared absorption spectroscopy (SEIRAS) in delineating impacts of specific components in the electrolyte like pH and anions on the catalyst structure, mass transport limitations with solution buffering species, and blocking of surface-bound intermediates. A fundamental component of the electrochemical interface that so far has not been addressed is the cation. Herein, we focus on determining the surface concentrations of alkali cations during CO_2-to-CO conversion on Au electrodes with the help of a novel molecular probe.

It has been known for almost a century that cations influence the energy landscape of electrocatlytic transformations [19, 23, 248, 249]. These cation effects offer a chance to tune the rates and selectivity for important yet challenging electrocatlytic processes like water splitting [250], nitrogen and nitrate reduction [251, 252], and CO_2 reduction [253–

255]. For example, during water oxidation on RuO_2(110), changing from 0.1 M LiOH electrolyte to 0.1 M KOH results in a drop of the activation barrier from 0.53 to 0.42 eV at a constant overpotential of 0.32 V [256]. For CO_2 reduction at -1.1 V versus the reversible hydrogen electrode (RHE) on Cu(100) electrodes, switching from 0.1 M $LiHCO_3$ to 0.1 M $CsHCO_3$ electrolyte results in an increase in the rate of ethylene evolution by a factor of $\sim$3.7 [257]. Even though clear cation effects have been demonstrated for a wide range of reactions, the mechanisms by which cations modulate these processes are still a matter of debate [23]. Mechanisms proposed include chemical and/or electrostatic interactions with adsorbates, [56, 71–73, 82, 231, 258–260], site-blocking, [75, 76, 261] changes in water structure, [25, 27] and modulation of the interfacial pH [77–79]. Under certain conditions, an interplay of multiple mechanisms can be expected to coexist [55, 74, 262, 263]. Intrinsically, these mechanisms are intertwined with the surface concentration of the cations. To delineate the conditions under which mechanisms are dominant, understanding the potential-dependent surface concentration of alkali metal cations is essential.

Pioneering studies have determined the surface coverages and structures of adlattices of alkali and alkaline earth metal cations on single crystal electrodes using Auger spectroscopy and low energy electron diffraction [264, 265]. These techniques rely on an ultra-high vacuum environment, necessitating the removal of the electrodes from the electrolyte prior to characterization. It was assumed that the structure of the electrochemical double-layer was preserved after transferring from a liquid to an ultra-high vacuum environment. To avoid this disturbance, modern approaches have employed surface X-ray diffraction. This approach provides significant alkali cation structural information at an electrode surface while remaining immersed in an aqueous electrolyte environment. However, the structure of alkali cations at an electrochemical interface under reaction conditions remains to be demonstrated. The electrolyte dependence of the electric field under operating conditions can been probed with vibrational stark spectroscopy [25, 74, 82, 262,

266, 267]. However, this technique is unable to determine the surface concentrations of alkali cations. To achieve the important goals in understanding the predominant cation effects, a general technique to probe the surface concentration of alkali cations in the electrochemical double layer under reactions conditions, like CO_2 reduction, is essential. In this work, we introduce such a technique and aim to achieve this task.

Using surface-enhanced infrared absorption spectroscopy, we have developed a novel probe to determine the relative surface concentration of alkali metal cations in the electrochemical double layer under CO_2 reduction reaction conditions on polycrystalline Au electrodes. This technique employs the organic cation tetramethylammonium ($methyl_4N^+$) as a potential-dependent probe of the cation surface concentration in the presence of alkali metal cations. By analyzing the CH_3 asymmetric stretching mode of $methyl_4N^+$, we reveal two distinct sub-populations of $methyl_4N^+$ in the electrochemical double layer: hydrated $methyl_4N^+$ and specifically adsorbed $methyl_4N^+$ ($methyl_4N^+_{ads}$). As the electrode potential is tuned negatively in a mixture of $methyl_4N^+$ and alkali cations, $methyl_4N^+_{ads}$ is displaced from the surface by the alkali cation. This makes the CH_3 asymmetric stretching mode of $methyl_4N^+_{ads}$ a direct measurement of the relative surface concentration of alkali cations. The degree of $methyl_4N^+_{ads}$ displacement is found to be sensitive to the alkali cation identity: for the same bulk concentration, the surface concentration increases with the size of the cation in the order of $Li^+ < Na^+ < K^+ < Cs^+$. Specifically, the relative surface concentration determined spectroscopically correlates to the hydration free energy of the respective cation. Cesium, with the least tightly bound hydration shell, has the highest surface concentration, and lithium, with the most tightly bound hydration shell has the lowest surface concentration. During CO_2 reduction on Au, we observe that the rate of CO production monotonically increases with the surface concentration of alkali cations. This observation reveals that the partial dehydration of the alkali metal cations is a crucial component in their ability to promote the CO_2 reduction reaction on electrode surfaces.

6.2 Results and Discussion

Potential-Dependence of Methyl$_4$N$^+$ in the Electrochemical Double Layer. To investigate the potential-dependent behavior of methyl$_4$N$^+$, we collected SEIRAS spectra in the attenuated total reflectance (ATR) configuration of the asymmetric CH_3 deformation mode (ν_{as}) [268] of this cation. Figure 6.1 shows representative spectra taken during the cathodic forward scan of cyclic voltammograms (CVs) of Au electrodes CO_2-saturated 0.1 M bicarbonate solutions of (A) 100 mM methyl$_4$N$^+$ and 0 mM K$^+$, (B) 90 mM methyl$_4$N$^+$ and 10 mM K$^+$, and (C) 50 mM methyl$_4$N$^+$ and 50 mM K$^+$. The corresponding current densities and reverse scan spectra are provided in Figure A6.1 of the Addendum. The scan rate of the CVs was 2 mV s^{-1} with nominal turning potentials of $+0.2V$ and -1.1 V versus the reversible hydrogen electrode (RHE) scale. All potentials in this chapter will be reported versus RHE unless otherwise noted. The change in optical density of the spectra were calculated according to $\Delta\mathrm{mOD} = -10^3 \log_{10} \frac{SB_S}{SB_R}$, where SB_S and SB_R refer to the single-beam spectra at the sample and reference potentials, respectively. +0.2 V was used as the reference for all spectra unless otherwise noted.

In Figure 6.1, a remarkable dependence of the ν_{as} lineshape on electrolyte composition is observed. When only 100 mM methyl$_4$N$^+$ is present, the predominant feature is a positive band at $\sim$1490 cm^{-1} that appears with decreasing potential (Figure 6.1A). When the electrolyte contains 10 mM K$^+$ and 90 mM methyl$_4$N$^+$, a biphasic feature appears with decreasing potential (Figure 6.1B), with the positive component centered at $\sim$1490 cm^{-1} and the negative portion at $\sim$1482 cm^{-1}. Increasing the concentration of K$^+$ further to 50 mM balanced by 50 mM methyl$_4$N$^+$, the positive feature at $\sim$1490 cm^{-1} is no longer present, and only the negative feature centered at $\sim$1482 cm^{-1} appears as the potential is tuned cathodically. These spectral features are not due to irreversible chemical processes: the peaks disappear in the reverse scan of the cyclic voltammograms with negligible hys-

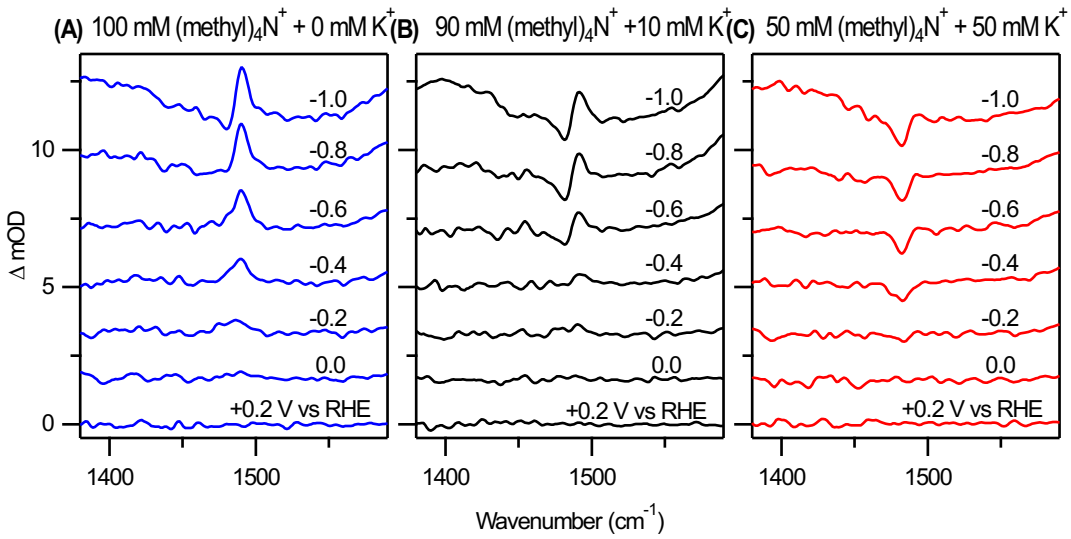

Figure 6.1: Representative potential-dependent spectra during the cathodic forward scan in (A) 100 mM methyl$_4$N$^+$, (B) 90 mM methyl$_4$N$^+$ and 10 mM K$^+$, and (C) 50 mM methyl$_4$N$^+$ and 50 mM K$^+$. The spectra are vertically offset for clarity.

teresis (Addendum, Figure A6.1). The reproducibility of these results is demonstrated in independent, duplicate experiments in Figure A6.2 of the Addendum.

The presence of these two bands under different electrolyte conditions suggest two distinct sub populations of methyl$_4$N$^+$. In order to distinguish these two populations, plotted in Figure 6.2 are spectra from each electrolyte at -0.8 V from Figure 6.1 for direct comparison to bulk solution IR spectra of 100 mM methyl$_4$N$^+$. The solution spectra only contain the single positive feature at $\sim$1490 cm^{-1}, corresponding to hydrated methyl$_4$N$^+$. Based on this, the peak observed at $\sim$1490 cm^{-1} in 6.1 is the same hydrated methyl$_4$N$^+$ species that electrostatically accumulates near the electrode surface as it is negatively charged. This assignment is further corroborated by the increase in the peaks amplitude with increasing bulk methyl$_4$N$^+$ and decreasing K$^+$ concentration (Figure 6.2).

Differentiation of Two Methyl$_4$N$^+$ Populations. We now focus on identifying the nature of the band at $\sim$1482 cm^{-1}. We will detail below that our experimental evidence suggests that this feature corresponds to adsorbed methyl$_4$N$^+$ that is displaced by K$^+$ as the

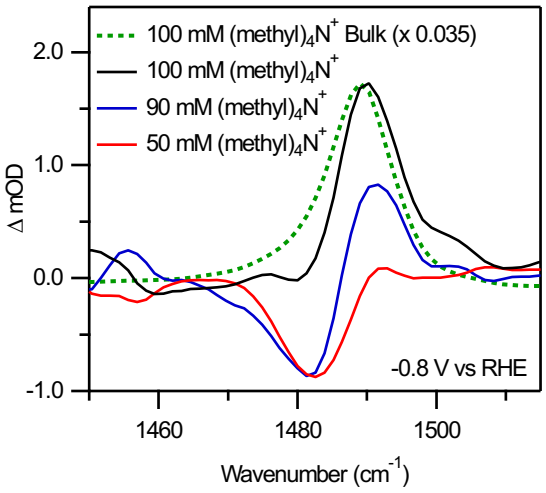

Figure 6.2: Representative spectra taken during the cathodic forward scan at -0.8 V at different concentrations of methyl$_4$N$^+$ balanced by K$^+$ to a total cation concentration of 100 mM. The green dashed line represents a spectrum of 100 mM of methyl$_4$N$^+$ in bulk solution.

potential is tuned negatively. When a cation specifically adsorbs onto an electrode surface, it is usually accompanied by a partial charge transfer from the surface to the cation: [228, 269]

$$\mathrm{M}_{\mathrm{aq}}^{\mathrm{z}+} + * + \delta\mathrm{e}^- \rightleftharpoons {}^*\mathrm{M}^{(\mathrm{z}-\delta)+}, \tag{6.1}$$

where M is the cation and z is its charge. δe^- describes the partial electron transfer upon specific adsorption on a surface site, denoted with $*$. With methyl$_4$N$^+$, we therefore expect to reduce the amount of positive charge on the cation by an amount δe^- upon specific adsorption. To assess the change in ν_{as} of methyl$_4$N$^+$ with charge, we carried out spectroscopy on a molecular analogue, trimethylamine. By simply altering the acid/base chemistry of trimethylamine, we can change the charge on the nitrogen and observe the shift in the CH$_3$ deformation mode frequency. Figure 6.3 shows the bulk solution spectra of trimethylamine and its protonated form, trimethylammonium. Upon losing the positive charge during deprotonation of the nitrogen, the ν_{as} of trimethylammonium red-shifts by

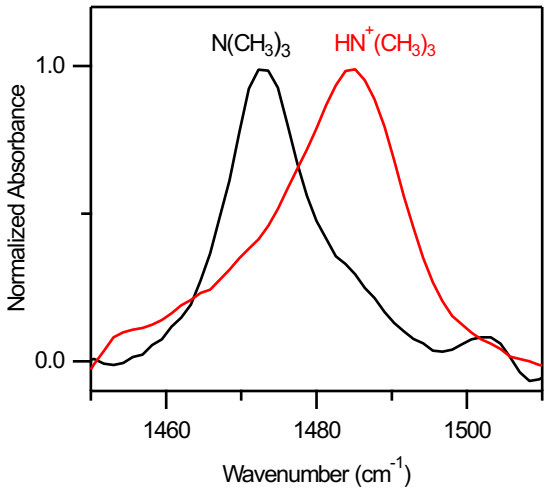

Figure 6.3: Spectra of trimethylamine (black, 10 mM methyl$_3$N plus 10 mM NaOH) and trimethylammonium (red, 10 mM methyl$_3$N plus 10 mM HCl) in bulk aqueous solutions.

approximately $\sim$12 cm^{-1}. Based on this observation, we assign the negative going feature at $\sim$1482 cm^{-1} to methyl$_4$N$^+_{\text{ads}}$, which is red-shifted from bulk methyl$_4$N$^+$ upon adsorption due to the partial charge transfer from the electrode surface via equation 6.1. It is probable that the red-shift in frequency is partly due to the different dielectric environment that occurs with partial dehydration during specific adsorption [270].

It is important to emphasize that the compounds in Figure 6.3 are only used as molecular analogues. We are not positing that there is decomposition of methyl$_4$N$^+$ into either trimethylamine or trimethylammonium. Recent work has demonstrated that methyl$_4$N$^+$ is stable under similar reaction conditions [271]. Further, the reversibility of the $\sim$1482 cm^{-1} band magnitude in the reverse scan of the CV(Addendum, Figure A6.1) suggests that no irreversible chemical process is occurring.

There are two plausible explanations for why a loss of absorbance occurs for the $\sim$1482 cm^{-1} band: A restructuring of the electric double layer with potential that angles the transition dipole moment of ν_{as} away from the surface normal, or a displacement of methyl$_4$N$^+_{\text{ads}}$ by K$^+$ with decreasing potential. It has been demonstrated with tetraalky-

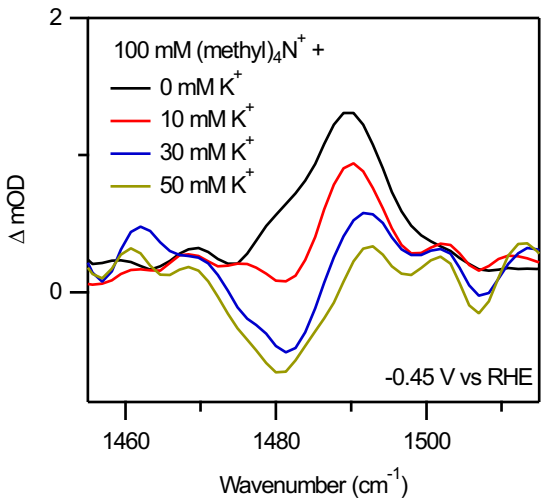

Figure 6.4: Change of lineshape of ν_{as} with addition of K^+ to an electrolyte initially containing only 100 mM methyl$_4$N(HCO_3) (black) at an electrode potential of -0.45 V. Small aliquots of 2 M $KHCO_3$ were added to achieve the desired concentration of K^+ indicated in the legend.

lammonium cations that as an electrode potential is tuned negatively, the cation can be re-oriented at the electrode surface [272]. However, this is expected to occur around the potential of zero charge (PZC) of the electrode. The potentials where we observe the loss of absorbance at $\sim$1482 cm^{-1} occur significantly negative of the PZC on Au electrodes (PZC = 0.16 V versus the standard hydrogen electrode) [273]. Therefore, it is unlikely that a potential dependent reorientation of methyl$_4$N$^+_{\mathrm{ads}}$ is occurring in the potential range studied. It is much more likely that methyl$_4$N$^+_{\mathrm{ads}}$ is being replaced by K^+ with decreasing potential. To confirm this, we carried out an experiment in which small aliquots of 2 M $KHCO_3$ are added to the electrolyte while maintaining a constant potential of methyl$_4$N$^+$. In Figure 6.4, spectra are taken at -0.45 V in an electrolyte initially containing only 100 mM methyl$_4$N(HCO_3). $KHCO_3$ was then added to the electrolyte to achieve final K^+ concentrations of 10, 30, and 50 mM, with the solution resistance measured and re-compensated (85% *in situ*) to account for the changes in solution conductivity. Like in Figures 6.1 and 6.2, Figure 6.4 demonstrates a similar negative feature at $\sim$1482 cm^{-1}

with increasing K^+ bulk concentration. Figure A6.3 in the Addendum demonstrates the reproducibility of these results. Taken together, the band at $\sim$1482 cm^{-1} is a spectroscopic measurement of the surface concentration of K^+.

To ascertain the physical origins of why K^+ displaces $methyl_4N^+_{ads}$ with decreasing potential in Figure 6.1, the potential-dependent adsorption of these cations was examined on an Au(111) surface with DFT. The Au(111) surface was chosen due to the (111)-character of the chemically deposited films used for the SEIRAS experiments [62]. The model employed was used to determine the electrosorption valvency (e_v). Within this model, the electrosorption valency of the adsorbed cation, or the effective number of electrons transferred upon adsorption (δe^-), governs the rate at which the free energy of adsorption becomes more negative with decreasing potential. The electosorption valency upon adsorption of Au(111) was calculated for the series of alkali metal cations including K^+ and $methyl_4N^+$ (Addendum, Table 6.1). The electrosorption valency for $methyl_4N^+$ (0.51) is smaller than that of K^+ (0.66). This indicates that the specific adsorption of K^+ is favored over $methyl_4N^+$ under a sufficiently negative applied electrode potential. Based on these findings, we submit that the difference in electrosorption valancy is a possible physical origin of the potential-dependent displacement of $methyl_4N^+$ by K^+.

$Methyl_4N^+_{ads}$ as a Probe of Alkali Cation Surface Population. With the band at $\sim$1482 cm^{-1} established as a spectroscopic measurement of the surface concentration of K^+, we wanted to expand this study to determine the surface concentration of other alkali metal cations. Accordingly, we carried out the same experiment in Figure 6.4 with Li^+, Na^+, and Cs^+ (Addendum, FigureA6.4), where small aliquots of each cation were successively added to the 100 mM $methyl_4N^+$ base electrolyte while observing the spectra at -0.45 V. The spectra were fitted with two Gaussian functions to determine the dependence of the $\sim$1482 cm^{-1} band area on the bulk alkali cation concentration (Figure 6.5). This fitting procedure is further described in the Experimental Methods section with ex-

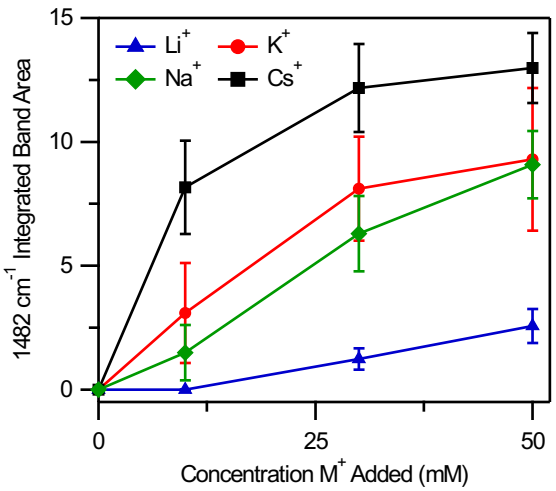

Figure 6.5: Dependence of the alkali cation surface concentration at an electrode potential of -0.45 V, as measured by the change in the methyl$_4$N$^+_{\text{ads}}$ band at $\sim$1482 cm^{-1}, as a function of bulk cation concentration as indicated. All electrolytes contained 100 mM methyl$_4$N$^+$. Error bars ($\pm$ 1 standard deviation) were calculated on the basis of at least 3 independent experiments.

ample fits in Figure A6.5 of the Addendum. The integrated area of the $\sim$1490 cm^{-1} band monotonically decreases with increasing alkali metal cation concentration (Addendum, Figure A6.6). To quantify the surface concentration of the alkali metal cation concentration, we focused the analysis on the $\sim$1482 cm^{-1} band. In Figure 6.5, we observe that the surface concentration, as measured by the $\sim$1482 cm^{-1} band area, is clearly dependent on the alkali cation identity. The surface concentration follows the trend of alkali cation size in the order of $\text{Li}^+ < \text{Na}^+ < \text{K}^+ < \text{Cs}^+$. Intriguingly, the magnitude of displacement of methyl$_4$N$^+_{\text{ads}}$ is linearly correlated to the free energy of hydration of the alkali cation (Figure 6.6).

Impact of Alkali Cation Surface Population on the Reduction of CO_2. To determine the relationship between alkali metal cation surface concentration and electrocatalytic properties, we carried our CO_2 reduction product determination studies on roughened Au electrodes at -0.45 V. At this potential, the rate of CO_2 reduction is not limited by mass transport, but by the adsorption of CO_2. The electrolysis was carried out in an H-cell

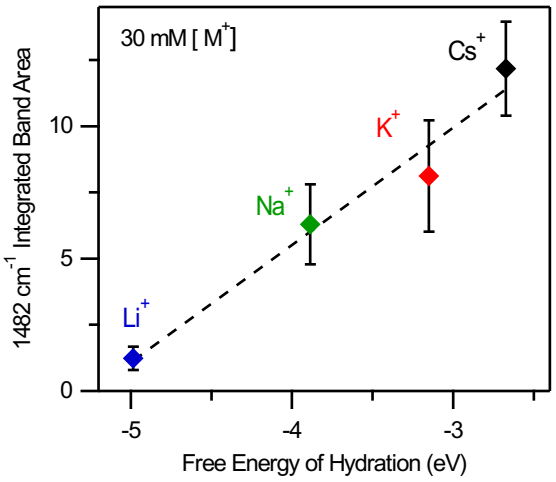

Figure 6.6: Dependence of the displacement of methyl$_4$N$^+_{\text{ads}}$ at $\sim$1482 cm^{-1} on the free energies of hydration determined at 1 M and 300 K [274] of (blue) Li$^+$, (green) Na$^+$, (red) K$^+$, and (black) Cs after addition of a bulk concentration of 30 mM to an electrolyte initially containing only 100 mM methyl$_4$N(HCO$_3$) at an electrode potential of -0.45 V. The dashed line is a linear fit to the data. The error bars represent $\pm$ 1 standard deviation and are calculated based on at least 3 independent experiments.

with CO$_2$ saturated 100 mM methyl$_4$NHCO$_3$ electrolyte containing 30 mM of the respective alkali cation MHCO$_3$. The head-space was analyzed with gas chromatography to measure the product formation. The representative electrochemical current densities and average Faradaic efficiencies are provided in Figure A6.7 and Figure A6.8, respectively, of the Addendum. The rates of H$_2$ and CO production as measured by partial current density were plotted as a function of alkali cation surface concentration, as measured by the $\sim$1482 cm^{-1} band area, in Figure 6.7. In Figure 6.7A, the rate of CO formation increases monotonically with the surface concentration of the cation, with Cs$^+$ achieving the highest rate. This observation suggests that the inclination of an alkali cation to accumulate at the electrode surface is a foundational factor in promoting the electrochemical reduction of CO$_2$.

While this technique is currently unable to describe the mechanism of alkali metal cation promotion of CO$_2$ reduction, an increase in the local cation concentration has pre-

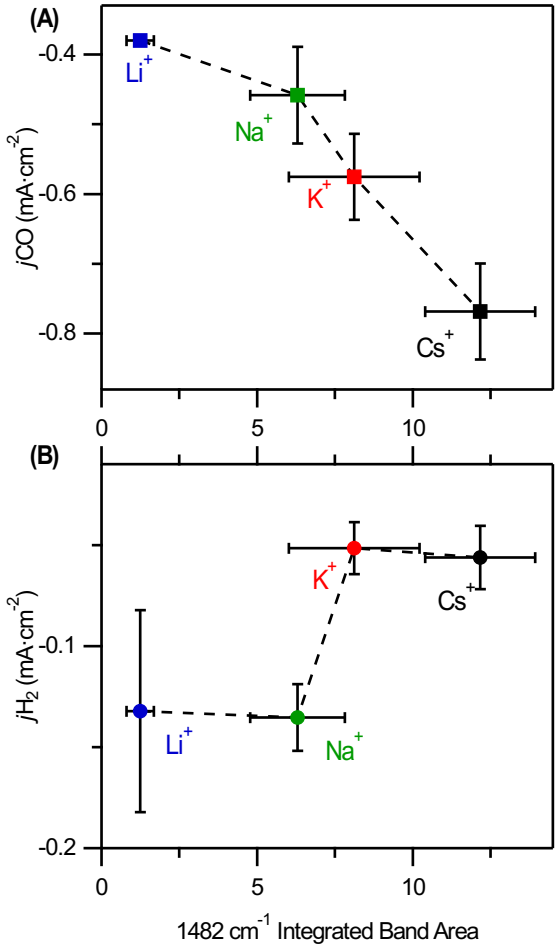

Figure 6.7: Dependence of the displacement of methyl$_4$N$^+_{\text{ads}}$ at $\sim$1482 cm^{-1} on the free energies of hydration determined at 1 M and 300 K [274] of (blue) Li$^+$, (green) Na$^+$, (red) K$^+$, and (black) Cs after addition of a bulk concentration of 30 mM to an electrolyte initially containing only 100 mM methyl$_4$N(HCO$_3$) at an electrode potential of -0.45 V. The dashed line is a linear fit to the data. The error bars represent $\pm$ 1 standard deviation and are calculated based on at least 3 independent experiments.

viously been suggested as a possible factor in the promotion of CO_2 reduction to ethylene on Cu electrodes with larger cations like Cs^+. It has been previously demonstrated that the adsorption of CO_2 accompanied by an electron transfer is the rate-determining step in during CO_2-to-CO conversion [132, 275, 276]. Recently it has been suggested that these cations play a critical role in this rate-determining step by stabilizing the transition state leading to the adsorbed CO_2 intermediate [56]. This can be accomplished by stabilizing electrostatic interactions and/or the coordination of cations to the nucleophilic oxygens of adsorbed CO_2 [56, 277].

In Figure 6.7B, the rate of hydrogen evolution appears to be relatively insensitive to the cation identity. However, the rate of hydrogen produced in Li^+ and Na^+ containing electrolytes is comparatively fast. This is likely due to the lower rates of CO_2 reduction to CO. Protons that would otherwise be consumed during CO_2 reduction or in the reaction with OH^- are available to form hydrogen. This argument regarding the competition of protons in parallel interfacial reactions has been invoked in prior studies regarding CO_2 and O_2 reduction reaction [278–280].

6.3 Conclusions

In this study we establish methyl$_4$N$^+$ as a molecular IR spectroscopic probe for the relative surface concentration of alkali metal cations during electrocatalytic conditions. By observing the the CH_3 deformation mode of methyl$_4$N$^+$ with SEIRAS on Au electrodes, we identified two distinct sub-populations of this cation: hydrated methyl$_4$N$^+$ at $\sim$1490 cm^{-1} and methyl$_4$N$^+_{\text{ads}}$ at $\sim$1482 cm^{-1}. In the presence of alkali cations, the methyl$_4$N$^+_{\text{ads}}$ is displaced as the electrode potential is tuned negatively, allowing the determination of the relative alkali cation surface concentration under catalytically relevant conditions. For a given bulk electrolyte cation concentration, the surface concentration is found to increase

with the size of the alkali cation and correlate with the cation's free energy of hydration. This work indicates that the ability of a cation to undergo partial dehydration is critical to it's ability to promote the electrochemical reduction of CO_2.

6.4 Materials and Methods

Materials. K_2CO_3 (99.997%, Puratronic, trace metals basis), Cs_2CO_3 (99.994%, Puratronic, trace metals basis), tetramethylammonium hydroxide (25 wt % solution in water; 99.9999% trace metals basis), and Au foil (>99.9975%; metals basis, 0.1 mm thick) were acquired from Alfa Aesar. Li_2CO_3 (99.999%, trace metals basis) was acquired from Acros Organics. Graphite rods (3 mm diameter, 99.995% trace metals basis) and $Na_2EDTA{\cdot}2H_2O$ (electrophoresis grade) were obtained from Sigma Aldrich. High-purity water derived from a Barnstead Nanopure Diamond System was used for electrolyte preparation. CO_2 (research grade) and Ar (ultra high purity) were procured from Air Gas. For electroless deposition of Au films on Si, $Na_2S_2O_3{\cdot}H_2O$ (99.999%; trace metals basis), Na_2SO_3 (98.5%; anhydrous), HF (48 wt %), NH_4F (40 wt %), and $NaAu_4{\cdot}2H_2O$ (99.99%; metals basis) were acquired from Fisher Scientific (Waltham, MA). Polycrystalline diamond pastes were purchased from Ted Pella (Redding, CA).

Electrolyte Preparation. Electrolytes for all experiments were prepared by dissolving the appropriate combination of tetramethylammonium and alkali metal cation salts to reach the desired cation concentration. With the exception of experiments in Figures 6.1 and 6.2, all electrolytes contained 10 μM ethylenediamine-tetra-acetic acid (EDTA) to prevent unwanted electrodeposition of metal ion impurities onto the Au electrode surface.[281, 282] The electrolyte was then purged with CO_2 at 40 standard cubic centimeters per minute (sccm) for 2 hours or until the electrolyte pH reached a stable pH reading of 6.8$\pm$0.1.

SEIRAS. SEIRAS experiments were carried out in a home-built two-compartment poly-etheretherketone (PEEK) cell with the catholyte (6 ml) and anolyte (5 ml) separated by a Selemion AMV anion exchange membrane (AGC Engineering Co.; Chiba, Japan). The Au thin-film electrode was deposited onto the reflecting plane of a 60° Si prism [62]. The Au film deposition was carried out as follows: The Si prism was first polished with 6 μM and 1 μM diamond slurries consecutively for five minutes each. The prism was then wiped under flowing DI water with a folded Kim wipe and sonicated in alternating high-purity water and acetone solutions for a total of five times of five minutes each. The Au film was deposited by first etching the surface of the Si prism in 40% NH_4F solution for 90 s. Following the etching, the reflecting plane was submerged in a mixture of $2:1$ mixture of plating solution and 2% HF solution at 63°C for 180 s. The plating solution contained 15 mM $NaAuCl_4{\cdot}2H_2O$, 50 mM $Na_2S_2O_3{\cdot}2H_2O$, 150 mM Na_2SO_3, and 50 mM NH_4Cl. In order to get a better conducting film, this first deposition was washed away with 100 μl of aqua regia, rinsed well with high-purity water, and blow dried with nitrogen. The prism was then re-submerged into the plating bath for 180 s to achieve the final film. Following the Au film deposition, the surface was rinsed with high purity water, blow-dried with N_2 gas, and the resistance across the film was measured to be $5-15\ \Omega$. The electrochemical cell was then assembled with a graphite rod and an Ag/AgCl electrode (3 M NaCl; Basi Inc.; West Lafayette, IN) as the counter and reference electrodes, respectively. The catholyte was first purged with CO_2 at 10 sccm for 20 minutes under open-circuit conditions and with stirring from a magnetic stir bar at 900 RPM. The Au film was then activated by stepping the potential to -1.3 V versus Ag/AgCl and held for 60 s [283]. Then, the potential was held at $+0.2$ V versus RHE for 10 min while the catholyte was stirred and CO_2 purged at the previously specified rates. Within the final minute of this 10 min period, 10 single-beam spectra, each representing 20 co-added single-beam spectra averaged over 4.6s, were averaged to use as the reference single-beam spectrum. Without returning to

open circuit, the electrode potential was then altered according to the experiment of interest while single-beam sample spectra were accumulated, with the CO_2 purging rate and stirring rate maintained for the duration of the experiment. Each subsequent sample spectrum acquired is an average of 20 co-added single-beam spectra over 4.6s and used to calculate the difference spectra shown in the respective figures ($\Delta\mathrm{mOD} = -10^3 \log_{10} \frac{S}{R}$). Spectra were collected with a 40 kHz scanner velocity and a 4 cm^{-1} resolution. The cell was connected to a nitrogen-purged ATR accessory (VeeMax III; Pike Technologies; Madison, WI) in the sample compartment of a Bruker Vertex 70 Fourier-transform infrared (FTIR) spectrometer, which was interfaced with a liquid nitrogen-cooled mercury cadmium telluride (MCT) detector (FTIR-16; Infrared Associates; Stuart, FL). The electrode potential was controlled with a VSP-300 potentiostat (Biologic; Seyssinet-Pariset, France). 85% of the solution resistance was compensated *in situ*. The remaining 15% was manually corrected following each experiment. For alkali cation addition experiments, compensation of the solution resistance (85%) was readjusted after each addition of alkali cation solution to account for the increase in conductivity in the electrolyte.

Peak Fitting Procedure. For determination of the integrated band areas shown in Figure 6.5 and Figure A6.6 in the Addendum, a combination of a linear background and two Gaussian functions were fit to the spectra. The peak positions and widths of the Gaussians describing the negative-going and positive-going bands at 1482 cm^{-1} and 1490 cm^{-1} were first determined as follows: For the peak at 1490 cm^{-1}, the best fit was determined for a 100 mM methyl$_4$NHCO$_3$ electrolyte in the absence of alkali metal cations where no negative-going band is present (Figure A6.5 in the Addendum). For the peak at 1482 cm^{-1}, the best fit was determined in the 50 mM methyl$_4$NHCO$_3$ and 50 mM KHCO$_3$ mixture, where no significant positive peak was present (Figure A6.5 B in the Addendum). To find the optimum fit for the biphasic spectra, the extracted peak positions and widths were kept constant and only the band amplitudes of the two Gaussian functions were used as

fitting parameters (Figure A6.5C in the Addendum).

Product Detection. Product detection was carried out in a two-compartment custom glass cell (Adams & Chittenden; Berkeley, CA). The catholyte and anolyte compartments contained 8.5 mL and 9.5 mL of electrolyte, respectively, and were separated by a Selemion AMV anion exchange membrane (AGC Engineering Co.; Chiba, Japan). To clean the Au foil, the surface was treated with aqua regia for 30 s, rinsed plentifully with high purity water, and blow-dried with N_2 gas. The Au working electrode with an exposed geometric surface area of 1.0 cm^2 was then introduced into the solution. The Au electrode was first anodically roughened. This procedure involved cycling the potential between -0.6 and 2.3 V at 50 mVs^{-1} in CO_2 saturated 0.1 M $KHCO_3$ electrolyte for three cycles, with a potential hold at 2.3 V for 30 min after the first cycle [284]. Immediately following the roughening procedure, the potential was stepped to -0.45 V for 30 min to fully reduce the Au surface. The electrode was then rinsed with high purity water and introduced into a clean cell with a fresh membrane and the electrolyte of interest.

The catholyte was stirred with a magnetic stir bar at 900 rpm throughout the experiments. Prior to the start of electrolysis, the catholyte was purged with CO_2 at 10 sccm for 20 min. The potential was then stepped to -0.45 V and gas chromatography (GC) measurements were obtained after the first 10 minutes of electrolysis. An SRI Instruments (Torrance, CA) Mulit-Gas 5 Configuration GC was calibrated with a gas mixture containing CO and H_2. A thermal conductivity detector (TCD) and a flame ionization detector (FID) were used to measure the produced amounts of H_2 and CO, respectively. The partial current density for each product was calculated according to: $\text{partial current} = \text{gas product volume}\% \times \text{flow rate} \times \frac{nFP}{RT} \times \frac{1}{A}$, where the gas product volume% is determined from the calibrated GC measurement, the flow rate is in liters per second, P = 101,325 Pa, T = 295.15 K, and A is the geometric surface area of the electrode.

6.5 Addendum

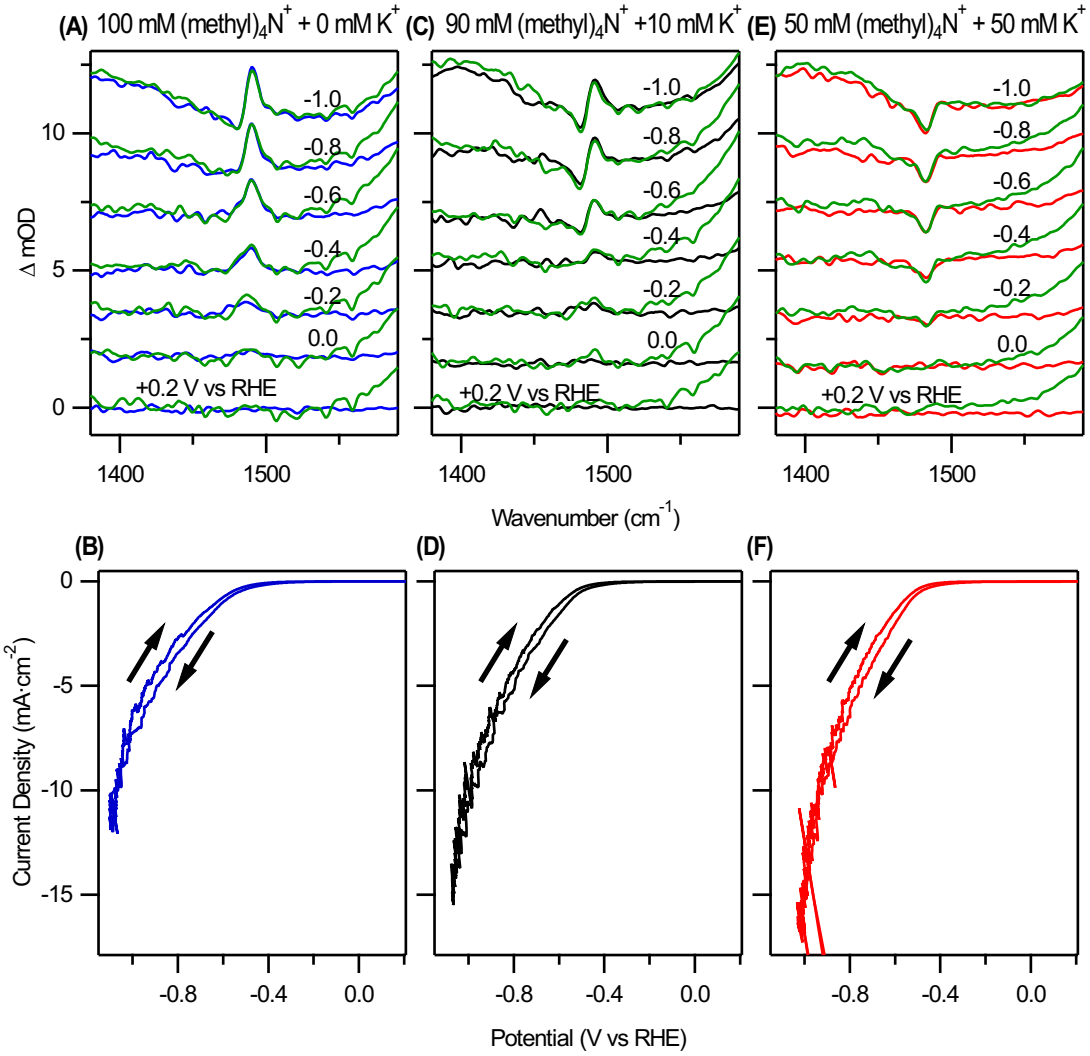

Figure A6.1: Representative potential-dependent spectra and the respective current density profiles during a voltammetric cycle. The spectra during the forward scans are shown in blue, green, and red and are reproduced from Figure 6.1. Spectra taken during the reverse scans at the same electrode potentials are overlaid and shown in green. Spectra are offset from the baseline for clarity. +0.2 V was used as the reference potential and −1.1 V as the nominal turning potential for the cyclic voltammograms. After correcting for the 15% uncompensated solution resistance, the turning point ranged from −1.03 V to −1.08 V depending on the magnitude of the current density. (A, B) 100 mM methyl$_4$N$^+$, (C, D) 90 mM methyl$_4$N$^+$ and 10 mM K$^+$, and (E, F) 50 mM methyl$_4$N$^+$ and 50 mM K$^+$.

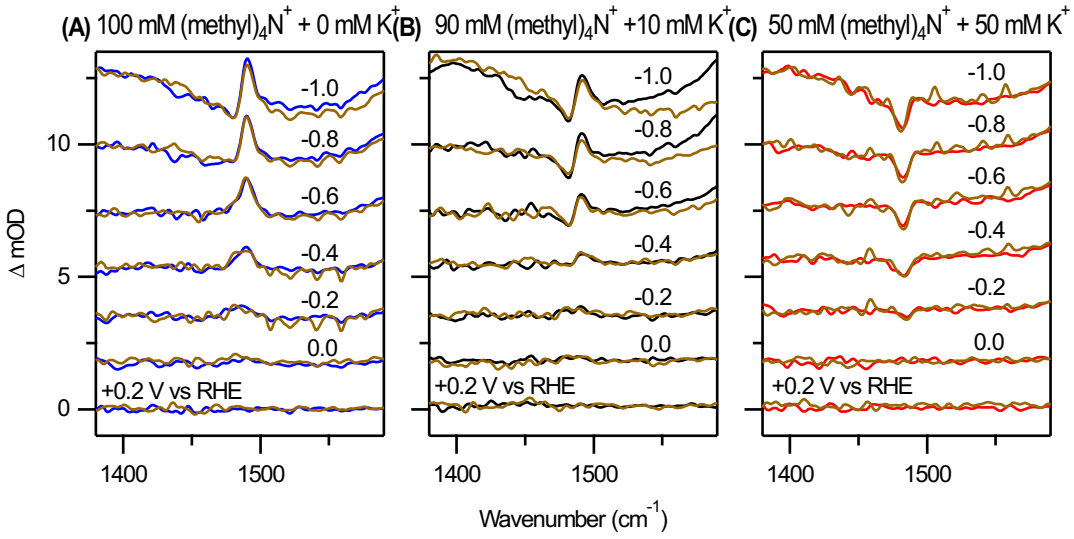

Figure A6.2: Comparison of the spectra shown in Figure 6.1 (shown in blue, black, and red) with other sets of spectra obtained in independent, repeated experiments (brown spectra) on freshly prepared Au electrodes. +0.2 V was used as the reference potential. Spectra are offset from the baseline for clarity. (A) 100 mM methyl$_4$N$^+$, (B) 90 mM methyl$_4$N$^+$ and 10 mM K$^+$, and (C) 50 mM methyl$_4$N$^+$ and 50 mM K$^+$.

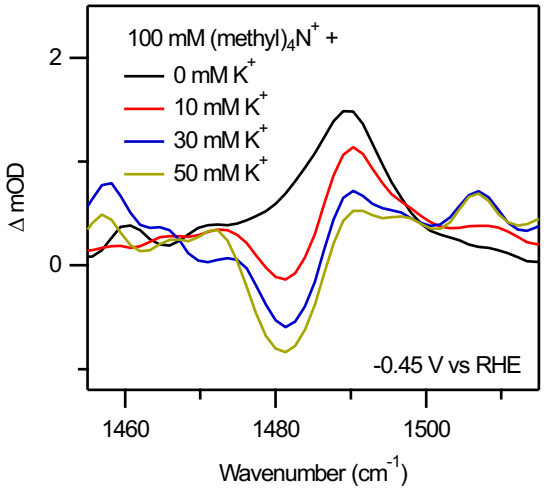

Figure A6.3: Spectra obtained in a duplicate experiment as the one shown in Figure 6.4, demonstrating reproducibility of the results.

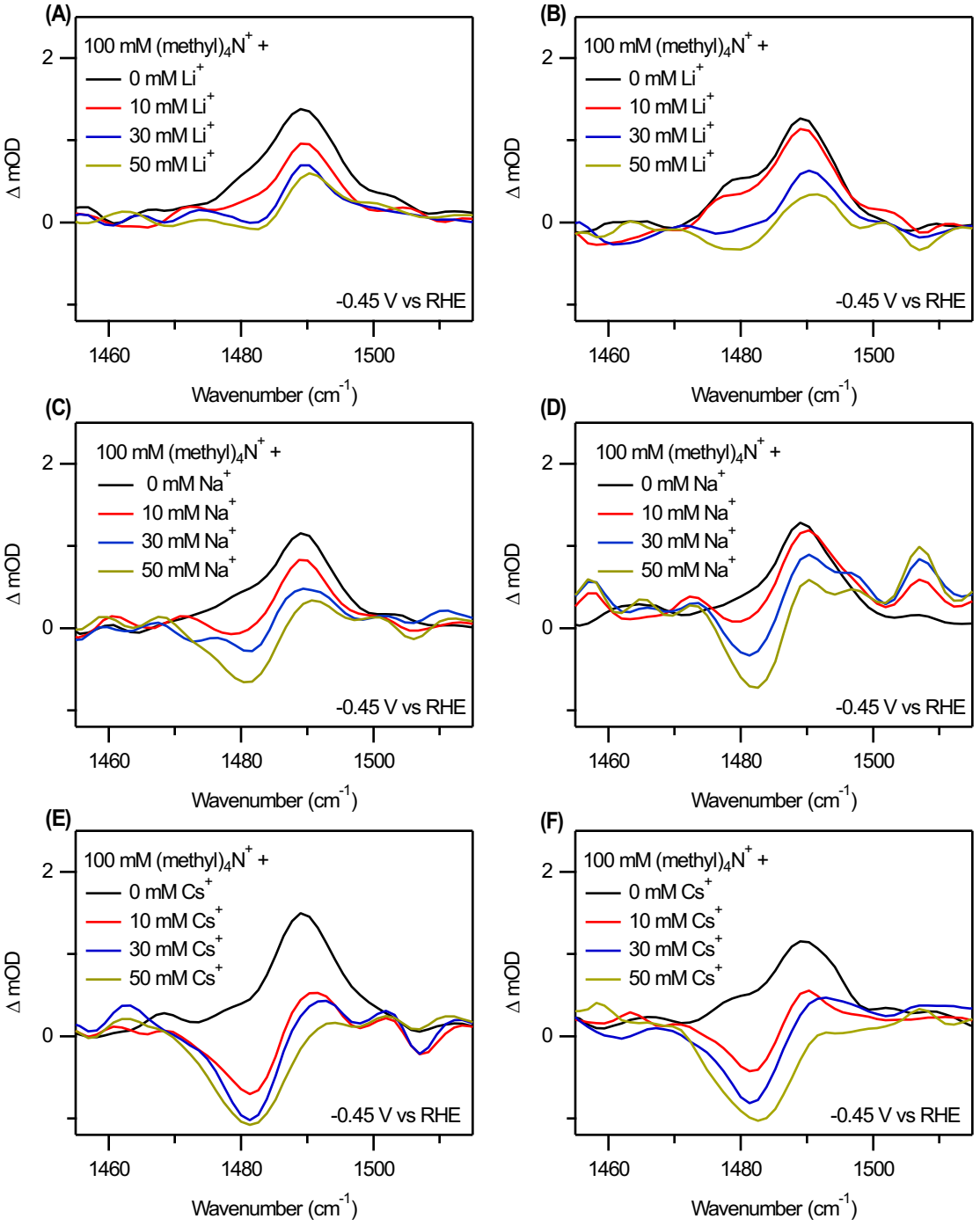

Figure A6.4: Spectra obtained in experiments as the one shown in Figure 6.4, but with Li^+, Na^+, and Cs^+. For each cation, spectra were obtained in two independent experiments conducted on freshly prepared Au electrodes are shown.

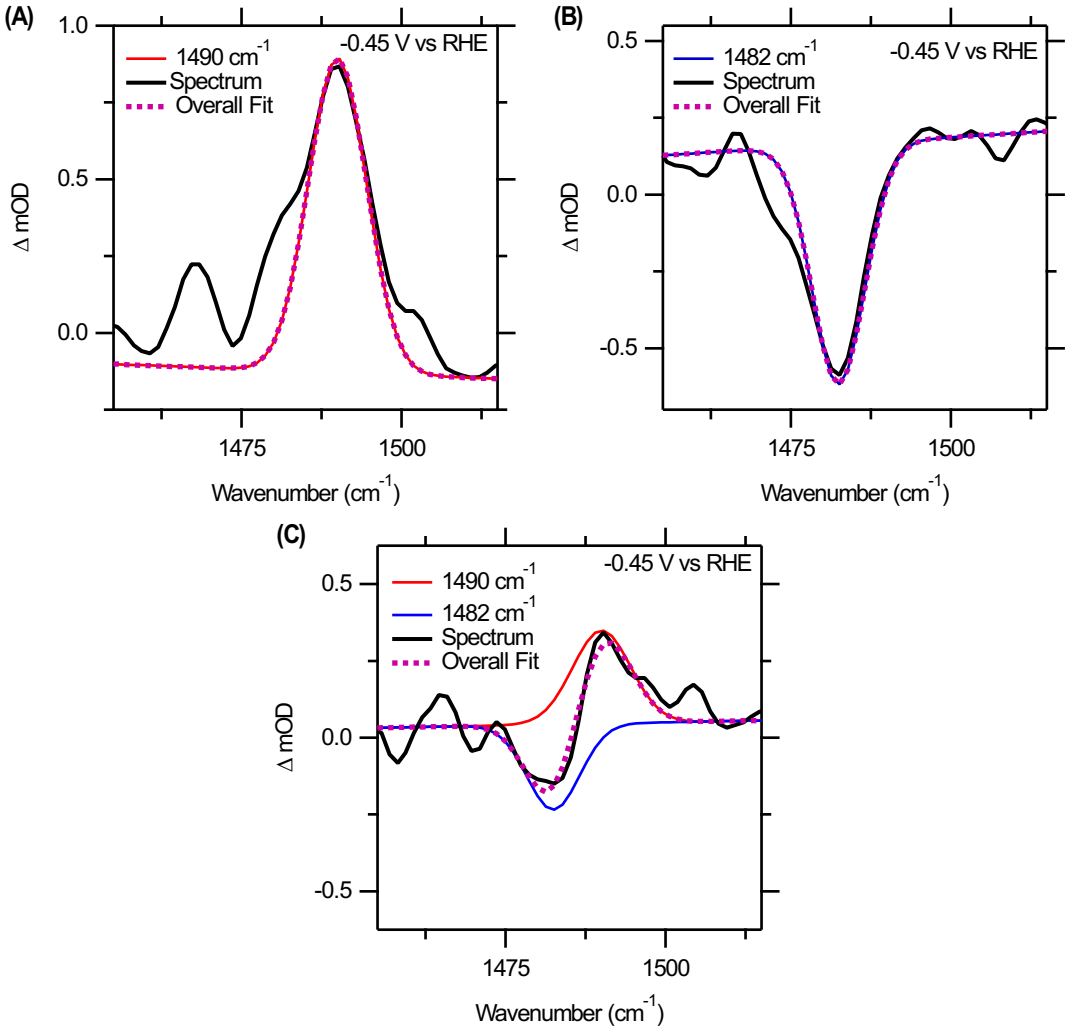

Figure A6.5: Representative spectra and the corresponding fits for (A) 100 mM methyl$_4$N$^+$, (B) 50 mM methyl$_4$N$^+$ and 50 mM K$^+$, and (C) 90 mM methyl$_4$N$^+$ and 10 mM K$^+$. The center frequencies of the Gaussian fits were held constant at 1482.4 and 1490.0 with widths of 9.6 and 10.6, respectively.

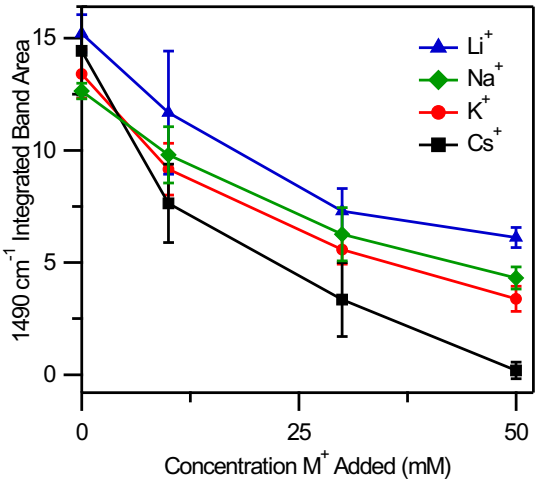

Figure A6.6: Displacement of hydrated methyl$_4$N$^+$ at -0.45 V as measured by the integrated band area of the 1490 cm^{-1} band as a function of alkali metal cation concentration in the bulk. All electrolytes contained 100 mM methyl$_4$N$^+$. Error bars ($\pm$ 1 standard deviation) were calculated on the basis of at least 3 independent experiments.

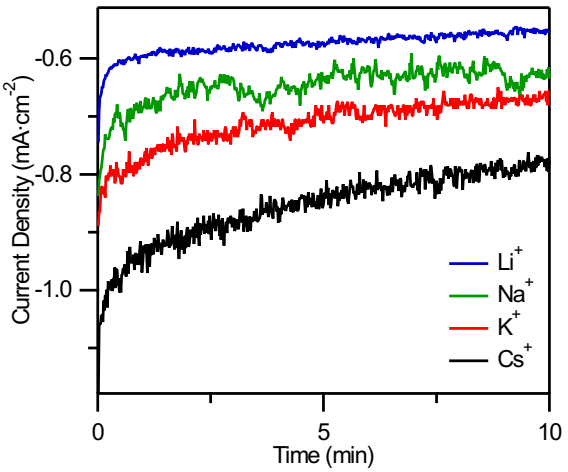

Figure A6.7: Representative chronoamperometric measurements conducted at an electrode potential of -0.45 V. The electrolyte contained 100 mM methyl$_4$N$^+$ and 30 mM of the designated alkali metal cation. A sample of the head space for product analysis was taken at 10 minutes.

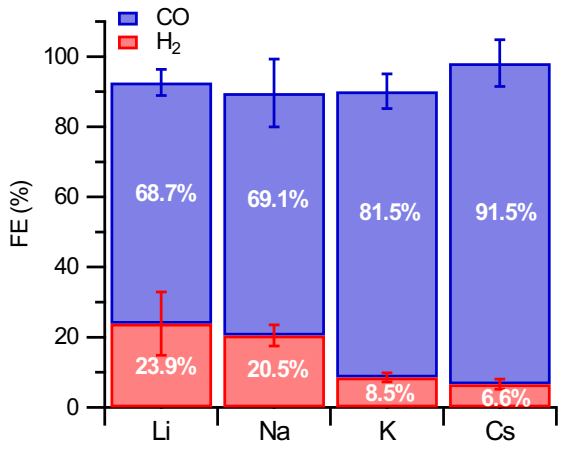

Figure A6.8: Average Faradaic efficiencies (FE%) corresponding to the measured partial current densities for (blue) CO and (red) H_2 in Figure 6.7. The FE% were calculated by dividing the partial current densities of the individual products by the total current density and multiplying by 100%. Error bars ($\pm$ 1 standard deviation) were calculated on the basis of at least 3 independent experiments.

Table A 6.1: Electrosorption valency calculations for specifically adsorbed cations on the Au(111) surface.

Evaluated Property	Li^+	Na^+	K^+	Cs^+	$methyl_4N^+$ with vdW
Bader charge on ads. cation	0.89	0.81	0.83	0.81	0.72
Surface dipole with cation ads. (eÅ)	-0.62	-0.77	-1.03	-0.97	-1.46
Electrosorption valency (e_v)	0.79	0.74	0.66	0.68	0.51

6.6 Acknowledgements

We acknowledge the financial support received through a CAREER award from the National Science Foundation (award no.:CHE-1847841). V. J. O. expresses gratitude to Yu-Shen Hsu for help collecting SEIRAS data.

Chapter 7

Summary and Future Perspective

In this dissertation, we demonstrated that the molecular components of the electrolyte side of the electrochemical interface can be be systematically studied to determine their unique impacts on electrocatalysis. This electrode/electrolyte interface where electrocatalysis takes place is a dynamic environment. Therefore, we employed *in situ* surface enhanced infrared absorption spectroscopy (SEIRAS), allowing us to capture the molecular make-up of the electrochemical double layer as a function of time, potential, and electrolyte species. This powerful technique facilitated the study CO_2 reduction on Cu and Au electrodes under *operando* conditions. Fundamentally, we gained a better understanding of how the supporting electrolyte 'supports' electrode interfacial processes.

On Cu, this was centered around the key intermediate for CO_2 reduction, adsorbed CO. In Chapter 3, we investigated how an alkaline electrolyte environment influences the relative coverages of CO_{atop} and CO_{bridge} on polycrystalline Cu. We showed that CO_{atop} can convert to CO_{bridge} when the total CO coverage dips below saturation values. The coverage of CO_{bridge} is found to increase with the interfacial pH and applied potential, likely due to an alkaline-pH induced reconstruction of the Cu surface that occurs during electrode polarization. Unlike CO_{atop}, CO_{bridge} was found to be inert to electrochemical reduction. Using DFT calculations, we determined that, relative to atop-bound CO, the stability of multiply-bonded CO increases with the increasing electric field under cathodic potentials,

raising the activation barrier to further reduction. While CO_{bridge} is not electrochemically active, it may still modulate the electrode surface properties during catalysis.

In Chapter 4, we uncovered how different organic thin-films derived from various N-arylpyridinium compounds drastically change the CO_2 reduction product selectivity on Cu. The (T-Pyr) organic film that increases the $C_{\geq 2}$ products selectivity does so not by changing the CO adsorption environment, but by limiting buffering near the electrode surface and increasing the interfacial pH as a result of its unique porous morphology. This was revealed by the increase in the interfacial carbonate IR band. In the presence of the (P-Pyr) organic film containing a nitrogen lone-pair functional group, hydrocarbon production is shutdown. This was observed to be a direct result of changes in the CO adsorption environment. The pyridyl group containing the nitrogen lone-pair was found to poison CO_{atop} sites on undercoordinated Cu, lending credence to these sites being the most active for further reduction adsorbed CO.

Chapter 5 revealed an interplay between anions of the supporting electrolyte and CO_{atop}. Under high aqueous concentrations (1 M), specifically (co-)adsorbed Cl^- was found to destabilize CO_{atop} binding, while non-specifically adsorbing SO_4^{-2} and ClO_4^- directly blocked a fraction of CO_{atop} sites. However, the blocking ability of the latter anions is dependent on the CO coverage, with a CO-induced stabilization with inreased coverage requiring more positive potentials to displace CO_{atop}. At low anion concentrations (10 mM), the anion identity does not change CO adsorption behavior. Regardless of anion identity and concentration, the onset potential for CO adsorption is relatively similar.

In Chapter 6, we pushed the boundaries of SEIRAS to probe the surface concentration of alkali cations under catalytic conditions in the electrolyte. To achieve this, we introduced a novel IR probe based on the CH_3 deformation band of the organic cation tetramethylammonium ($methyl_4N^+$). We observed that $methyl_4N^+$ specifically adsorbed on the Au electrode can be directly displaced by alkali cations. The degree of this displacement is

an experimental measure of the surface concentration of alkali cations under catalytically relevant potentials. For the same bulk concentration of alkali metal cations, their relative surface concentrations during CO_2-to-CO reduction follows the order of $Li^+ < Na^+ < K^+ < Cs^+$. Interestingly, the observed surface cation concentration correlates with the alkali cation's free energy of hydration. Coupled with product determination studies, the rate of CO_2-to-CO conversion increases as a function of the alkali cation surface concentration. This chapter established the hydration energy of a cation and the ability to undergo partial dehydration at the electrode/electrolyte interface as a critical descriptors in the ability of a cation to promote CO_2-to-CO reduction.

The work presented in this thesis attempts to provide a broad understanding of the electrochemical double layer under catalytically relevant conditions through spectroscopic insights into the effects of the electrolyte, including IR-inactive anions and cations. With SEIRAS, there are still some limitations in the applications of this technique in general and its application to advance the further study of CO_2 reduction.

- The study of IR-inactive electrolyte components with SEIRAS inherently requires a probe. With the introduction of a probe, there is always a liability that the probe alters catalysis. For our anion studies, tracking the local anion concentration in the electrochemical double layer was limited by the small amplitude of the O-D stretch band: anions could only be directly probed under 1 M concentrations. The cation studies required the presence of methyl$_4N^+$. This probe is powerful in determining the surface cation concentration, however it may disturb the some of the more subtle cation effects. For Cu electrodes, surface adsorbed CO is powerful probe, especially when applied towards CO_2 reduction. However, the analysis of this CO_{ads} is non-trivial, as the overall IR band is a complex mixture of CO coordination environment, dynamical dipole coupling, coordination to electrolyte species, and local electric fields[50]. The application CO_{ads} on other electrodes like Au and Ag can

also be challenging as the coverages tend to be very low during catalytically relevant conditions. Recent advances in plasmon-resonant vibrational sum frequency generation have made the detection and analysis of CO_{ads} generated from CO_2 reduction on Au more feasible.[263].

- Like with CO detection during CO_2 reduction on Au, the utility of SEIRAS to study reaction intermediates with low coverages can be held back by the signal intensities. The further signal enhancement of low-coverage intermediates could potentially come about with highly ordered nano-structures. Different patterns and shapes of nano-structures have been demonstrated to generate significant electromagnetic fields [285]. The resulting signals can achieve enhancement factors for SEIRAS on the order of 10^5.

- In Chapters 3 and 4 we observed a crucial role of alkaline pH environments on the electrode and double layer structure. The initial motivation for the work in Chapters 3 was the observed increase in selectivity for CO_2/CO reduction under alkaline pH conditions. While the selectivity may be improved, CO_2 reduction under alkaline conditions results in the consumption of CO_2 in homogeneous side reactions, significantly lowering the single-pass conversion of CO_2[276, 286]. Recently, CO_2 reduction has been carried out under acidic conditions at significant reaction rates [280, 287, 288], greatly improving the single-pass conversion. Therefore, it would be of great interest to study CO_2 reduction under acidic electrolyte conditions. This is possible with chemically deposited Au thin-film electrodes, but highly unlikely with Cu thin-film electrodes due to its dissolution under open circuit conditions in acidic electrolytes.

- While SEIRAS studies like the ones presented in this work have helped advance the field of CO_2 reduction, they may be limited in developing the field further for

industrially relevant conditions. This is due to the fundamental limitations of CO_2 reduction in an H-cell type setup. During CO_2 reduction, gaseous CO_2 must be dissolved in the electrolyte in order to be reduced at the electrode surface. Therefore, at high reaction rates, this process is limited by the solubility and mass transport of CO_2. To overcome this, gas diffusion electrodes (GDE) have been successfully employed to enhance the current density during CO_2 conversion to industrially relevant rates[289, 290]. However, the engineering of the GDE design is fundamentally inapplicable to our current SEIRAS setup. Thus, spectroscopic studies of GDE setups requires other *in situ* techniques, like Raman spectroscopy [291] and/or electrochemical atomic force microscopy (EC-AFM) [292], for example.

Even with some of these current limitations previously discussed, the future is still bright for the application of SEIRAS and the study of the CO_2 reduction mechanism. In combination with online product detection techniques like differential electrochemical mass spectrometry (DEMS), interfacial structures as measured with SEIRAS can be directly linked to the product output as measured with DEMS. This technique has been previously demonstrated by our group [25, 62], however further upgrades to the electrochemical cell to include a thin-layer flow cell configuration will further maximize its potential. With SEIRAS on its own, there is opportunities to enhance the information available in each spectrum. By rapidly polarizing the incoming light to the Si prism, structural information such as the angle of adsorbed intermediates and the orientation of interfacial water may be accessed. This technique, known as polarization modulation, has been used to characterize air/water interfaces in high detail [293]. It can be directly added to an IR spectrometer without significant alterations of the current SEIRAS electrochemical cell designs.

Even without these instrumental modifications, our SEIRAS investigations are ongoing. While the modification of metal electrodes with organic films like those derived from

N-arylpyridinium compounds can be messy, the use of porous crystalline materials can allow the modification of electrode surfaces in a purposeful and reproducible manner. This could be achieved by growing thin layers of metal organic frameworks (MOFs) and covalent organic frameworks (COFs) directly on the electrode surface. On Au, with our methyl$_4$N$^+$ probe, we can expand the spectroscopic studies of surface cation concentration to include other cations such as alkaline earth metal cations or ionic liquids. It will also be interesting to see if the phenomena observed on Au electrodes can be recreated on Cu electrodes.

Bibliography

1. Crippa, M., Guizzardi, D, Muntean, M, Schaaf, E, Solazzo, E, Monforti-Ferrario, F, Olivier, J. & Vignati, E. *Fossil CO_2 and GHG emissions of all world countries: 2020 report.* 2020.

2. Masson-Delmotte, V, Zhai, P, Pirani, A, Connors, S., Péan, C, Berger, S, Caud, N, Chen, Y, Goldfarb, L, Gomis, M., Huang, M, Leitzell, K, Lonnoy, E, Matthews, J. B. R, K, T. M. T., Waterfield, T, Yelekçi, O, Yu, R & Zhou, B. *IPCC, 2021: Climate Change 2021: The Physical Science Basis. Contribution of Working Group I to the Sixth Assessment Report of the Intergovernmental Panel on Climate Change* 2021.

3. Agency, I. E. *The Future of Petrochemicals* 2018.

4. Rosen, B. R., Werner, E. W., O'Brien, A. G. & Baran, P. S. Total synthesis of dixiamycin B by electrochemical oxidation. *J. Am. Chem. Soc.* **136,** 5571–5574 (2014).

5. Kingston, C., Palkowitz, M. D., Takahira, Y., Vantourout, J. C., Peters, B. K., Kawamata, Y. & Baran, P. S. A Survival Guide for the "Electro-curious". *Acc. Chem. Res.* **53,** 72–83. ISSN: 0001-4842 (Jan. 2020).

6. Möhle, S., Zirbes, M., Rodrigo, E., Gieshoff, T., Wiebe, A. & Waldvogel, S. R. Modern Electrochemical Aspects for the Synthesis of Value-Added Organic Products. *Angew. Chem. Inter. Ed.* **57,** 6018–6041 (2018).

7. Xu, K., Chen, P., Li, X., Tong, Y., Ding, H., Wu, X., Chu, W., Peng, Z., Wu, C. & Xie, Y. Metallic Nickel Nitride Nanosheets Realizing Enhanced Electrochemical Water Oxidation. *J. Am. Chem. Soc.* **137,** 4119–4125 (2015).

8. Yan, Y., Xia, B. Y., Zhao, B. & Wang, X. A Review on Noble-Metal-Free Bifunctional Heterogeneous Catalysts for Overall Electrochemical Water Splitting. *J. Mater. Chem. A* **4,** 17587–17603 (45 2016).

9. Utley, J. H. in *Fundamentals of Thermochemical Biomass Conversion* 1087–1102 (Springer, 1985).

10. Vuyyuru, K. R. & Strasser, P. Oxidation of Biomass Derived 5-Hydroxymethylfurfural using Heterogeneous and Electrochemical Catalysis. *Catal. Today* **195,** 144–154 (2012).

11. Hori, Y. & Suzuki, S. Electrolytic Reduction of Carbon Dioxide at Mercury Electrode in Aqueous Solution. *Bull. Chem. Soc. Jpn.* **55,** 660–665 (1982).

12. Kuhl, K. P., Cave, E. R., Abram, D. N. & Jaramillo, T. F. New Insights into the Electrochemical Reduction of Carbon Dioxide on Metallic Copper Surfaces. *Energ. Environ. Sci.* **5,** 7050–7059 (5 2012).

13. De Arquer, F. P. G., Dinh, C.-T., Ozden, A., Wicks, J., McCallum, C., Kirmani, A. R., Nam, D.-H., Gabardo, C., Seifitokaldani, A., Wang, X., Li, Y. C., Li, F., Edwards, J., Richter, L. J., Thorpe, S. J., Sinton, D. & Sargent, E. H. CO_2 electrolysis to multicarbon products at activities greater than 1 A cm^{-1}. *Science* **367,** 661–666 (2020).

14. Schouten, K. J. P., Kwon, Y., van der Ham, C. J. M., Qin, Z. & Koper, M. T. M. A New Mechanism for the Selectivity to C1 and C2 Species in the Electrochemical Reduction of Carbon Dioxide on Copper Electrodes. *Chem. Sci.* **2,** 1902–1909 (10 2011).

15. Kortlever, R., Shen, J., Schouten, K. J. P., Calle-Vallejo, F. & Koper, M. T. M. Catalysts and Reaction Pathways for the Electrochemical Reduction of Carbon Dioxide. *J. Phys. Chem. Lett.* **6,** 4073–4082 (2015).

16. Ruckenstein, E. & Wang, H. Carbon Deposition and Catalytic Deactivation during CO_2 Reforming of CH_4 over Co/γ-Al_2O_3 Catalysts. *J. Catal.* **205,** 289–293 (2002).

17. Popović, S., Smiljanić, M., Jovanovič, P., Vavra, J., Buonsanti, R. & Hodnik, N. Stability and Degradation Mechanisms of Copper-Based Catalysts for Electrochemical CO_2 Reduction. *Angew. Chem. Int. Ed.* **59,** 14736–14746 (2020).

18. Park, S., Wijaya, D. T., Na, J. & Lee, C. W. Towards the Large-Scale Electrochemical Reduction of Carbon Dioxide. *Catalysts* **11,** 253 (2021).

19. Danilovic, N., Subbaraman, R., Strmcnik, D., Paulikas, A. P., Myers, D., Stamenkovic, V. R. & Markovic, N. M. The Effect of Noncovalent Interactions on the HOR, ORR, and HER on Ru, Ir, and $Ru_{0.50}Ir_{0.50}$ Metal Surfaces in Alkaline Environments. *Electrocatalysis* **3,** 221–229 (2012).

20. Koper, M. T. M. Theory of Multiple Proton-Electron Transfer Reactions and Its Implications for Electrocatalysis. *Chem. Sci.* **4,** 2710–2723 (2013).

21. Remsing, R. C., McKendry, I. G., Strongin, D. R., Klein, M. L. & Zdilla, M. J. Frustrated Solvation Structures Can Enhance Electron Transfer Rates. *J. Phys. Chem. Lett.* **6,** 4804–4808 (2015).

22. Varela, A. S., Kroschel, M., Reier, T. & Strasser, P. Controlling the Selectivity of CO_2 Electroreduction on Copper: The Effect of the Electrolyte Concentration and the Importance of the Local pH. *Catal. Today* **260,** 8–13 (2016).

23. Waegele, M. M., Gunathunge, C. M., Li, J. & Li, X. How Cations Affect the Electric Double Layer and the Rates and Selectivity of Electrocatalytic Processes. *J. Chem. Phys.* **151,** 160902 (2019).

24. Ovalle, V. J. & Waegele, M. M. Understanding the Impact of N-Arylpyridinium Ions on the Selectivity of CO_2 Reduction at the Cu/Electrolyte Interface. *J. Phys. Chem. C* **123,** 24453–24460 (2019).

25. Li, J., Li, X., Gunathunge, C. M. & Waegele, M. M. Hydrogen Bonding Steers the Product Selectivity of Electrocatalytic CO Reduction. *Proc. Natl. Acad. Sci. USA* **116,** 9220–9229 (2019).

26. Ovalle, V. J. & Waegele, M. M. Impact of Electrolyte Anions on the Adsorption of CO on Cu Electrodes. *J. Phys. Chem. C* **124,** 14713–14721 (2020).

27. Zhang, Z.-Q., Banerjee, S., Thoi, V. S. & Shoji Hall, A. Reorganization of Interfacial Water by an Amphiphilic Cationic Surfactant Promotes CO_2 Reduction. *J. Phys. Chem. Lett.* **11,** 5457–5463 (2020).

28. Zhang, F. & Co, A. C. Direct Evidence of Local pH Change and the Role of Alkali Cation during CO_2 Electroreduction in Aqueous Media. *Angew. Chem. Inter. Ed.* **59,** 1674–1681 (2020).

29. Ryu, J. & Surendranath, Y. Polarization-Induced Local pH Swing Promotes Pd-Catalyzed CO_2 Hydrogenation. *J. Am. Chem. Soc.* **142,** 13384–13390 (2020).

30. Thevenon, A., Rosas-Hernández, A., Fontani Herreros, A. M., Agapie, T. & Peters, J. C. Dramatic HER Suppression on Ag Electrodes via Molecular Films for Highly Selective CO_2 to CO Reduction. *ACS Catal.* **11,** 4530–4537 (Apr. 2021).

31. Gunathunge, C. M., Li, X., Li, J., Hicks, R. P., Ovalle, V. J. & Waegele, M. M. Spectroscopic Observation of Reversible Surface Reconstruction of Copper Electrodes under CO_2 Reduction. *J. Phys. Chem. C* **121,** 12337–12344 (2017).

32. Medina-Ramos, J., Zhang, W., Yoon, K., Bai, P., Chemburkar, A., Tang, W., Atifi, A., Lee, S. S., Fister, T. T., Ingram, B. J., Rosenthal, J., Neurock, M., van Duin,

A. C. T. & Fenter, P. Cathodic Corrosion at the Bismuth-Ionic Liquid Electrolyte Interface under Conditions for CO_2 Reduction. *Chem. Mater.* **30,** 2362–2373 (2018).

33. Yan, B., Krishnamurthy, D., Hendon, C. H., Deshpande, S., Surendranath, Y. & Viswanathan, V. Surface Restructuring of Nickel Sulfide Generates Optimally Coordinated Active Sites for Oxygen Reduction Catalysis. *Joule* **1,** 600–612 (2017).

34. Hori, Y., Takahashi, I., Koga, O. & Hoshi, N. Selective Formation of C2 Compounds from Electrochemical Reduction of CO_2 at a Series of Copper Single Crystal Electrodes. *J. Phys. Chem. B* **106,** 15–17 (2002).

35. Durand, W. J., Peterson, A. A., Studt, F., Abild-Pedersen, F. & Nørskov, J. K. Structure Effects on the Energetics of the Electrochemical Reduction of CO_2 by Copper Surfaces. *Surf. Sci.* **605,** 1354–1359 (2011).

36. Schouten, K. J. P., Qin, Z., Pérez Gallent, E. & Koper, M. T. M. Two Pathways for the Formation of Ethylene in CO Reduction on Single-Crystal Copper Electrodes. *J. Am. Chem. Soc.* **134,** 9864–9867 (2012).

37. Huang, Y., Handoko, A. D., Hirunsit, P. & Yeo, B. S. Electrochemical Reduction of CO_2 Using Copper Single-Crystal Surfaces: Effects of CO* Coverage on the Selective Formation of Ethylene. *ACS Catal.* **7,** 1749–1756 (2017).

38. Scholten, F., Nguyen, K.-L. C., Bruce, J. P., Heyde, M. & Roldan Cuenya, B. Identifying Structure–Selectivity Correlations in the Electrochemical Reduction of CO_2: A Comparison of Well-Ordered Atomically Clean and Chemically Etched Copper Single-Crystal Surfaces. *Angew. Chem., Int. Ed.* **60,** 19169–19175. ISSN: 1433-7851 (Aug. 2021).

39. Kim, Y.-G., Baricuatro, J. H., Javier, A., Gregoire, J. M. & Soriaga, M. P. The Evolution of the Polycrystalline Copper Surface, First to Cu(111) and Then to Cu(100),

at a Fixed CO_2RR Potential: A Study by *Operando* EC-STM. *Langmuir* **30,** 15053–15056 (2014).

40. Kim, Y.-G. & Soriaga, M. P. Cathodic Regeneration of a Clean and Ordered Cu(100)-(1×1) Surface from an Air-Oxidized and Disordered Electrode: An Operando STM Study. *J. Electroanal. Chem* **734,** 7–9. ISSN: 1572-6657 (2014).

41. Eren, B., Zherebetskyy, D., Patera, L. L., Wu, C. H., Bluhm, H., Africh, C., Wang, L.-W., Somorjai, G. A. & Salmeron, M. Activation of Cu(111) Surface by Decomposition into Nanoclusters Driven by CO Adsorption. *Science* **351,** 475–478 (2016).

42. Eren, B., Liu, Z., Stacchiola, D., Somorjai, G. A. & Salmeron, M. Structural Changes of Cu(110) and Cu(110)-(2 $\times$ 1)-O Surfaces under Carbon Monoxide in the Torr Pressure Range Studied with Scanning Tunneling Microscopy and Infrared Reflection Absorption Spectroscopy. *J. Phys. Chem. C* **120,** 8227–8231 (2016).

43. Handoko, A. D., Wei, F., Jenndy, Yeo, B. S. & Seh, Z. W. Understanding heterogeneous electrocatalytic carbon dioxide reduction through operando techniques. *Nature Catalysis* **1,** 922–934. ISSN: 2520-1158 (Dec. 2018).

44. Li, X., Gunathunge, C. M., Agrawal, N., Montalvo-Castro, H., Jin, J., Janik, M. J. & Waegele, M. M. Impact of Alkali Metal Cations and Iron Impurities on the Evolution of Hydrogen on Cu Electrodes in Alkaline Electrolytes. *J. Electrochem. Soc.* **167,** 106505 (2020).

45. Svintsitskiy, D. A., Kardash, T. Y., Stonkus, O. A., Slavinskaya, E. M., Stadnichenko, A. I., Koscheev, S. V., Chupakhin, A. P. & Boronin, A. I. In situ XRD, XPS, TEM, and TPR study of highly active in CO oxidation CuO nanopowders. *J. Phys. Chem. C* **117,** 14588–14599 (2013).

46. Choi, Y.-W., Scholten, F., Sinev, I. & Roldan Cuenya, B. Enhanced Stability and CO/Formate Selectivity of Plasma-Treated SnO x/AgO x Catalysts during CO_2 Electroreduction. *J. Am. Chem. Soc.* **141,** 5261–5266 (2019).

47. Weng, Z., Wu, Y., Wang, M., Jiang, J., Yang, K., Huo, S., Wang, X.-F., Ma, Q., Brudvig, G. W., Batista, V. S., Liang, Y., Feng, Z. & Wang, H. Active Sites of Copper-complex Catalytic Materials for Electrochemical Carbon Dioxide Reduction. *Nat. Commun.* **9,** 415 (2018).

48. Baricuatro, J. H., Kim, Y.-G., Korzeniewski, C. L. & Soriaga, M. P. Seriatim ECSTM-ECPMIRS of the adsorption of carbon monoxide on Cu(100) in alkaline solution at CO2-reduction potentials. *Electrochem. commun.* **91,** 1–4. ISSN: 1388-2481 (June 2018).

49. Zhu, S., Li, T., Cai, W.-B. & Shao, M. CO_2 Electrochemical Reduction As Probed through Infrared Spectroscopy. *ACS Energy Lett.* **4,** 682–689 (Mar. 2019).

50. Gunathunge, C. M., Li, J., Li, X. & Waegele, M. M. Surface-Adsorbed CO as an Infrared Probe of Electrocatalytic Interfaces. *ACS Catalysis* **10,** 11700–11711 (Oct. 2020).

51. Osawa, M. Dynamic Processes in Electrochemical Reactions Studied by Surface-Enhanced Infrared Absorption Spectroscopy (SEIRAS). *Bull. Chem. Soc. Jpn.* **70,** 2861–2880 (1997).

52. Hoffmann, F. M. Infrared Reflection-Absorption Spectroscopy of Adsorbed Molecules. *Surf. Sci. Rep.* **3,** 107–192. ISSN: 0167-5729 (1983).

53. König, M., Vaes, J., Klemm, E. & Pant, D. Solvents and Supporting Electrolytes in the Electrocatalytic Reduction of CO_2. *iScience* **19,** 135–160. ISSN: 2589-0042 (Sept. 2019).

54. Resasco, J., Lum, Y., Clark, E., Zeledon, J. Z. & Bell, A. T. Effects of Anion Identity and Concentration on Electrochemical Reduction of CO_2. *ChemElectroChem* **5,** 1064–1072. ISSN: 2196-0216 (Apr. 2018).

55. Ringe, S., Clark, E. L., Resasco, J., Walton, A., Seger, B., Bell, A. T. & Chan, K. Understanding Cation Effects in Electrochemical CO_2 Reduction. *Energy Environ. Sci.* **12,** 3001–3014 (10 2019).

56. Monteiro, M. C. O., Dattila, F., Hagedoorn, B., García-Muelas, R., López, N. & Koper, M. T. M. Absence of CO_2 Electroreduction on Copper, Gold and Silver Electrodes without Metal Cations in Solution. *Nature Catalysis* **4,** 654–662. ISSN: 2520-1158 (Aug. 2021).

57. Varela, A. S., Ju, W., Reier, T. & Strasser, P. Tuning the Catalytic Activity and Selectivity of Cu for CO_2 Electroreduction in the Presence of Halides. *ACS Catal.* **6,** 2136–2144 (2016).

58. Huang, Y., Ong, C. W. & Yeo, B. S. Effects of Electrolyte Anions on the Reduction of Carbon Dioxide to Ethylene and Ethanol on Copper (100) and (111) Surfaces. *ChemSusChem* **11,** 3299–3306 (2018).

59. Gao, D., Sinev, I., Scholten, F., Arán-Ais, R. M., Divins, N. J., Kvashnina, K., Timoshenko, J. & Roldan Cuenya, B. Selective CO_2 Electroreduction to Ethylene and Multicarbon Alcohols via Electrolyte-Driven Nanostructuring. *Angew. Chem. Inter. Ed.* **58,** 17047–17053 (2019).

60. Yang, Y., Li, K., Ajmal, S., Feng, Y., Bacha, A.-U.-R., Nabi, I. & Zhang, L. Interplay between Halides in the Electrolyte and the Chemical States of Cu in Cu-based Electrodes Determines the Selectivity of the C2 Product. *Sus. Energy Fuels* **4,** 2284–2292 (5 2020).

61. Ma, W., Xie, S., Liu, T., Fan, Q., Ye, J., Sun, F., Jiang, Z., Zhang, Q., Cheng, J. & Wang, Y. A. Electrocatalytic Reduction of CO_2 to Ethylene and Ethanol Through Hydrogen-assisted C-C Coupling over Fluorine-modified Copper. *Nat. Catal.,* 2520–1158 (2020).

62. Gunathunge, C. M., Li, J., Li, X., Hong, J. J. & Waegele, M. M. Revealing the Predominant Surface Facets of Rough Cu Electrodes under Electrochemical Conditions. *ACS Catal.* **10,** 6908–6923 (2020).

63. Hori, Y., Murata, A. & Takahashi, R. Formation of Hydrocarbons in the Electrochemical Reduction of Carbon Dioxide at a Copper Electrode in Aqueous Solution. *J. Chem. Soc., Faraday Trans. 1* **85,** 2309–2326 (8 1989).

64. Kas, R., Kortlever, R., Yf±lmaz, H., Koper, M. T. M. & Mul, G. Manipulating the Hydrocarbon Selectivity of Copper Nanoparticles in CO_2 Electroreduction by Process Conditions. *ChemElectroChem* **2,** 354–358 (2015).

65. Tornow, C. E., Thorson, M. R., Ma, S., Gewirth, A. A. & Kenis, P. J. A. Nitrogen-Based Catalysts for the Electrochemical Reduction of CO_2 to CO. *J. Am. Chem. Soc.* **134,** 19520–19523 (2012).

66. Xie, M. S., Xia, B. Y., Li, Y., Yan, Y., Yang, Y., Sun, Q., Chan, S. H., Fisher, A. & Wang, X. Amino Acid Modified Copper Electrodes for the Enhanced Selective Electroreduction of Carbon Dioxide Towards Hydrocarbons. *Energy Environ. Sci.* **9,** 1687–1695 (2016).

67. Fang, Y. & Flake, J. C. Electrochemical Reduction of CO_2 at Functionalized Au Electrodes. *J. Am. Chem. Soc.* **139,** 3399–3405 (2017).

68. Hoang, T. T. H., Ma, S., Gold, J. I., Kenis, P. J. A. & Gewirth, A. A. Nanoporous Copper Films by Additive-Controlled Electrodeposition: CO_2 Reduction Catalysis. *ACS Catal.* **7,** 3313–3321 (2017).

69. Han, Z., Kortlever, R., Chen, H.-Y., Peters, J. C. & Agapie, T. CO_2 Reduction Selective for $C_{\geq 2}$ Products on Polycrystalline Copper with N-Substituted Pyridinium Additives. *ACS Cent. Sci.* **3,** 853–859 (2017).

70. Wuttig, A., Ryu, J. & Surendranath, Y. Electrolyte Competition Controls Surface Binding of CO Intermediates to CO_2 Reduction Catalysts. *J. Phys. Chem. C* **125,** 17042–17050. ISSN: 1932-7447 (Aug. 2021).

71. Chen, L. D., Urushihara, M., Chan, K. & Nørskov, J. K. Electric Field Effects in Electrochemical CO_2 Reduction. *ACS Catal.* **6,** 7133–7139 (2016).

72. Akhade, S. A., McCrum, I. T. & Janik, M. J. The Impact of Specifically Adsorbed Ions on the Copper-Catalyzed Electroreduction of CO_2. *J. Electrochem. Soc.* **163,** F477 (2016).

73. Chen, X., McCrum, I. T., Schwarz, K. A., Janik, M. J. & Koper, M. T. M. Co-adsorption of Cations as the Cause of the Apparent pH Dependence of Hydrogen Adsorption on a Stepped Platinum Single-Crystal Electrode. *Angew. Chem. Int. Ed.* **56,** 15025–15029 (2017).

74. Malkani, A. S., Li, J., Oliveira, N. J., He, M., Chang, X., Xu, B. & Lu, Q. Understanding the Electric and Nonelectric Field Components of the Cation Effect on the Electrochemical CO Reduction Reaction. *Sci. Adv.* **6,** eabd2569 (Nov. 2020).

75. Feaster, J. T., Jongerius, A. L., Liu, X., Urushihara, M., Nitopi, S. A., Hahn, C., Chan, K., Nørskov, J. K. & Jaramillo, T. F. Understanding the Influence of [EMIM]Cl on the Suppression of the Hydrogen Evolution Reaction on Transition Metal Electrodes. *Langmuir* **33,** 9464–9471 (2017).

76. Bhargava, S. S., Cofell, E. R., Chumble, P., Azmoodeh, D., Someshwar, S. & Kenis, P. J. Exploring Multivalent Cations-Based Electrolytes for CO_2 Electroreduction. *Electrochim. Acta* **394,** 139055 (Oct. 2021).

77. Singh, M. R., Kwon, Y., Lum, Y., Ager, J. W. & Bell, A. T. Hydrolysis of Electrolyte Cations Enhances the Electrochemical Reduction of CO_2 over Ag and Cu. *J. Am. Chem. Soc.* **138,** 13006–13012 (2016).

78. Ayemoba, O. & Cuesta, A. Spectroscopic Evidence of Size-Dependent Buffering of Interfacial pH by Cation Hydrolysis during CO_2 Electroreduction. *ACS Appl. Mater. Interfaces* **9,** 27377–27382 (2017).

79. Zhang, F. & Co, A. C. Direct Evidence of Local pH Change and the Role of Alkali Cation during CO_2 Electroreduction in Aqueous Media. *Angew. Chem. Inter. Ed.* **58,** 2–10 (2019).

80. Murata, A. & Hori, Y. Product Selectivity Affected by Cationic Species in Electrochemical Reduction of CO_2 and CO at a Cu Electrode. *Bull. Chem. Soc. Jpn.* **64,** 123–127 (1991).

81. Thorson, M. R., Siil, K. I. & Kenis, P. J. A. Effect of Cations on the Electrochemical Conversion of CO_2 to CO. *J. Electrochem. Soc.* **160,** F69–F74 (2013).

82. Gunathunge, C. M., Ovalle, V. J. & Waegele, M. M. Probing Promoting Effects of Alkali Cations on the Reduction of CO at the Aqueous Electrolyte/Copper Interface. *Phys. Chem. Chem. Phys.* **19,** 30166–30172 (44 2017).

83. Faulkner, L. R. & Bard, A. J. *Electrochemical Methods: Fundamentals and Applications* chap. 13 (John Wiley and Sons, 2002).

84. Helmholtz, H. Ueber einige Gesetze der Vertheilung elektrischer Ströme in körperlichen Leitern mit Anwendung auf die thierisch-elektrischen Versuche. *Annalen der Physik* **165,** 211–233 (1853).

85. Helmholtz, H. Studien über electrische Grenzschichten. *Annalen der Physik* **243,** 337–382. ISSN: 0003-3804 (Jan. 1879).

86. Grahame, D. C. The Electrical Double Layer and the Theory of Electrocapillarity. *Chem. Rev.* **41,** 441–501 (1947).

87. Gouy, M. Sur la constitution de la charge électrique à la surface d'un électrolyte. *J. Phys. Radium* **9,** 457–468 (1910).

88. Chapman, D. L. A contribution to the theory of electrocapillarity. *Phil. Mag.* **25,** 475–481 (1913).

89. Iwasita, T. & Nart, F. C. In situ infrared spectroscopy at electrochemical interfaces. *Prog. Surf. Sci.* **55,** 271–340. ISSN: 0079-6816 (Aug. 1997).

90. Osawa, M. *In-situ Surface-Enhanced Infrared Spectroscopy of the Electrode/Solution Interface* 269–314. ISBN: 9783527616817 (John Wiley & Sons, Ltd, 2006).

91. Milosevic, M. *Internal Reflection and ATR Spectroscopy* (John Wiley & Sons, 2012).

92. Hartstein, A., Kirtley, J. R. & Tsang, J. C. Enhancement of the Infrared Absorption from Molecular Monolayers with Thin Metal Overlayers. *Phys. Rev. Lett.* **45,** 201–204 (3 1980).

93. Osawa, M. & Ikeda, M. Surface-Enhanced Infrared Absorption of p-Nitrobenzoic Acid Deposited on Silver Island Films: Contributions of Electromagnetic and Chemical Mechanisms. *J. Phys. Chem.* **95,** 9914–9919 (1991).

94. Skibbe, O., Binder, M., Otto, A. & Pucci, A. Electronic Contributions to Infrared Spectra of Adsorbate Molecules on Metal Surfaces: Ethene on Cu(111). *J. Chem. Phys.* **128,** 194703 (2008).

95. Lu, G.-Q., Sun, S.-G., Chen, S.-P. & Cai, L.-R. Novel Properties of Dispersed Pt and Pd Thin Layers Supported on GC for CO Adsorption Studied Using In Situ MS-FTIR Reflection Spectroscopy. *J. Electroanal. Chem.* **421,** 19–23 (1997).

96. Aroca, R. & Price, B. A New Surface for Surface-Enhanced Infrared Spectroscopy: Tin Island Films. *J. Phys. Chem. B* **101,** 6537–6540 (1997).

97. Lu, G.-Q., Sun, S.-G., Cai, L.-R., Chen, S.-P., Tian, Z.-W. & Shiu, K.-K. In Situ FTIR Spectroscopic Studies of Adsorption of CO, SCN^-, and Poly(o-phenylenediamine) on Electrodes of Nanometer Thin Films of Pt, Pd, and Rh: Abnormal Infrared Effects (AIREs). *Langmuir* **16,** 778–786 (2000).

98. Kraack, J. P., Kaech, A. & Hamm, P. Surface Enhancement in Ultrafast 2D ATR IR Spectroscopy at the Metal-Liquid Interface. *J. Phy. Chem. C* **120,** 3350–3359 (2016).

99. Osawa, M. Surface-Enhanced Infrared Absorption. *Topics Appl. Phys.* **81,** 163–187 (2001).

100. Osawa, M. & Ataka, K.-I. Electromagnetic Mechanism of Enhanced Infrared Absorption of Molecules Adsorbed on Metal Island Films. *Surf. Sci.* **262,** L118–L122 (1992).

101. Merklin, G. T. & Griffiths, P. R. Influence of Chemical Interactions on the Surface-Enhanced Infrared Absorption Spectrometry of Nitrophenols on Copper and Silver Films. *Langmuir* **13,** 6159–6163 (1997).

102. Blyholder, G. Molecular Orbital View of Chemisorbed Carbon Monoxide. *J. Phys. Chem.* **68,** 2772–2777 (1964).

103. Föhlisch, A., Nyberg, M., Hasselström, J., Karis, O., Pettersson, L. G. M. & Nilsson, A. How Carbon Monoxide Adsorbs in Different Sites. *Phys. Rev. Lett.* **85,** 3309–3312 (15 2000).

104. Hammer, B., Morikawa, Y. & Nørskov, J. K. CO Chemisorption at Metal Surfaces and Overlayers. *Phys. Rev. Lett.* **76,** 2141–2144 (12 1996).

105. Kuhl, K. P., Cave, E. R., Abram, D. N. & Jaramillo, T. F. New Insights into the Electrochemical Reduction of Carbon Dioxide on Metallic Copper Surfaces. *Energy Environ. Sci.* **5,** 7050–7059 (2012).

106. Reske, R., Mistry, H., Behafarid, F., Roldan Cuenya, B. & Strasser, P. Particle Size Effects in the Catalytic Electroreduction of CO_2 on Cu Nanoparticles. *J. Am. Chem. Soc.* **136,** 6978–6986 (2014).

107. Roberts, F. S., Kuhl, K. P. & Nilsson, A. High Selectivity for Ethylene from Carbon Dioxide Reduction over Copper Nanocube Electrocatalysts. *Angew. Chem. Int. Ed.* **54,** 5179–5182 (2015).

108. Verdaguer-Casadevall, A., Li, C. W., Johansson, T. P., Scott, S. B., McKeown, J. T., Kumar, M., Stephens, I. E. L., Kanan, M. W. & Chorkendorff, I. Probing the Active Surface Sites for CO Reduction on Oxide-Derived Copper Electrocatalysts. *J. Am. Chem. Soc.* **137,** 9808–9811 (2015).

109. Loiudice, A., Lobaccaro, P., Kamali, E. A., Thao, T., Huang, B. H., Ager, J. W. & Buonsanti, R. Tailoring Copper Nanocrystals towards C_2 Products in Electrochemical CO_2 Reduction. *Angew. Chem. Int. Ed.* **55,** 5789–5792 (2016).

110. Feng, X., Jiang, K., Fan, S. & Kanan, M. W. A Direct Grain-Boundary-Activity Correlation for CO Electroreduction on Cu Nanoparticles. *ACS Cent. Sci.* **2,** 169–174 (2016).

111. Ma, S., Sadakiyo, M., Luo, R., Heima, M., Yamauchi, M. & Kenis, P. J. One-Step Electrosynthesis of Ethylene and Ethanol from CO_2 in an Alkaline Electrolyzer. *J.Power Sources* **301,** 219–228 (2016).

112. Mistry, H., Varela, A. S., Bonifacio, C. S., Zegkinoglou, I., Sinev, I., Choi, Y.-W., Kisslinger, K., Stach, E. A., Yang, J. C., Strasser, P. & Cuenya, B. R. Highly Selec-

tive Plasma-Activated Copper Catalysts for Carbon Dioxide Reduction to Ethylene. *Nat. Commun.* **7,** 12123 (June 2016).

113. Kim, D., Kley, C. S., Li, Y. & Yang, P. Copper Nanoparticle Ensembles for Selective Electroreduction of CO_2 to C_2-C_3 Products. *Proc. Natl. Acad. Sci. U. S. A.* **114,** 10560–10565 (2017).

114. Hahn, C., Hatsukade, T., Kim, Y.-G., Vailionis, A., Baricuatro, J. H., Higgins, D. C., Nitopi, S. A., Soriaga, M. P. & Jaramillo, T. F. Engineering Cu Surfaces for the Electrocatalytic Conversion of CO_2: Controlling Selectivity Toward Oxygenates and Hydrocarbons. *Proc. Nat. Acad. Sci. U. S. A.* **114,** 5918–5923 (2017).

115. Reller, C., Krause, R., Volkova, E., Schmid, B., Neubauer, S., Rucki, A., Schuster, M. & Schmid, G. Selective Electroreduction of CO_2 toward Ethylene on Nano Dendritic Copper Catalysts at High Current Density. *Adv. Energy Mater.* **7,** 1602114 (2017).

116. De Luna, P., Quintero-Bermudez, R., Dinh, C.-T., Ross, M. B., Bushuyev, O. S., Todorović, P., Regier, T., Kelley, S. O., Yang, P. & Sargent, E. H. Catalyst Electro-Redeposition Controls Morphology and Oxidation State for Selective Carbon Dioxide Reduction. *Nat. Catal.* **1,** 103–110 (2018).

117. Bertheussen, E., Hogg, T. V., Abghoui, Y., Engstfeld, A. K., Chorkendorff, I. & Stephens, I. E. L. Electroreduction of CO on Polycrystalline Copper at Low Overpotentials. *ACS Energy Lett.* **3,** 634–640 (2018).

118. Jeon, H. S., Kunze, S., Scholten, F. & Roldan Cuenya, B. Prism-Shaped Cu Nanocatalysts for Electrochemical CO_2 Reduction to Ethylene. *ACS Catal.* **8,** 531–535 (2018).

119. Dinh, C.-T., Burdyny, T., Kibria, M. G., Seifitokaldani, A., Gabardo, C. M., García de Arquer, F. P., Kiani, A., Edwards, J. P., De Luna, P., Bushuyev, O. S., Zou, C., Quintero-Bermudez, R., Pang, Y., Sinton, D. & Sargent, E. H. CO_2 Electroreduction to Ethylene via Hydroxide-Mediated Copper Catalysis at an Abrupt Interface. *Science* **360,** 783–787 (2018).

120. Hori, Y. in *Modern Aspects of Electrochemistry* (eds Vayenas, C. G., White, R. E. & Gamboa-Aldeco, M. E.) 89–189 (Springer New York, New York, NY, 2008). ISBN: 978-0-387-49489-0.

121. Gattrell, M., Gupta, N. & Co, A. A Review of the Aqueous Electrochemical Reduction of CO_2 to Hydrocarbons at Copper. *J. Electroanal. Chem.* **594,** 1–19 (2006).

122. Hori, Y., Murata, A., Takahashi, R. & Suzuki, S. Electrochemical Reduction of Carbon Monoxide to Hydrocarbons at Various Metal Electrodes in Aqueous Solution. *Chem. Lett.* **16,** 1665–1668 (1987).

123. Hori, Y., Takahashi, R., Yoshinami, Y. & Murata, A. Electrochemical Reduction of CO at a Copper Electrode. *J. Phys. Chem. B* **101,** 7075–7081 (1997).

124. Peterson, A. A., Abild-Pedersen, F., Studt, F., Rossmeisl, J. & Nørskov, J. K. How Copper Catalyzes the Electroreduction of Carbon Dioxide into Hydrocarbon Fuels. *Energy Environ. Sci.* **3,** 1311–1315 (9 2010).

125. Nie, X., Esopi, M. R., Janik, M. J. & Asthagiri, A. Selectivity of CO_2 Reduction on Copper Electrodes: The Role of the Kinetics of Elementary Steps. *Angew. Chem., Int. Ed.* **52,** 2459–2462 (2013).

126. Goodpaster, J. D., Bell, A. T. & Head-Gordon, M. Identification of Possible Pathways for C-C Bond Formation during Electrochemical Reduction of CO_2: New Theoretical Insights from an Improved Electrochemical Model. *J. Phys. Chem. Lett.* **7,** 1471–1477 (2016).

127. Xiao, H., Cheng, T. & Goddard, W. A. Atomistic Mechanisms Underlying Selectivities in C_1 and C_2 Products from Electrochemical Reduction of CO on Cu(111). *J. Am. Chem. Soc.* **139,** 130–136 (2017).

128. Tang, W., Peterson, A. A., Varela, A. S., Jovanov, Z. P., Bech, L., Durand, W. J., Dahl, S., Nørskov, J. K. & Chorkendorff, I. The Importance of Surface Morphology in Controlling the Selectivity of Polycrystalline Copper for CO_2 Electroreduction. *Phys. Chem. Chem. Phys.* **14,** 76–81 (1 2012).

129. Calle-Vallejo, F. & Koper, M. T. M. Theoretical Considerations on the Electroreduction of CO to C_2 Species on Cu(100) Electrodes. *Ange. Chem. Int. Ed.* **52,** 7282–7285 (2013).

130. Zhang, Y.-J., Sethuraman, V., Michalsky, R. & Peterson, A. A. Competition between CO_2 Reduction and H_2 Evolution on Transition-Metal Electrocatalysts. *ACS Catal.* **4,** 3742–3748 (2014).

131. Samjeské, G., Komatsu, K.-i. & Osawa, M. Dynamics of CO Oxidation on a Polycrystalline Platinum Electrode: A Time-Resolved Infrared Study. *J. Phys. Chem. C* **113,** 10222–10228 (2009).

132. Wuttig, A., Yaguchi, M., Motobayashi, K., Osawa, M. & Surendranath, Y. Inhibited Proton Transfer Enhances Au-Catalyzed CO_2-to-Fuels Selectivity. *Proc. Natl. Acad. Sci. U.S.A.* **113,** E4585–E4593 (2016).

133. Pérez-Gallent, E., Figueiredo, M. C., Calle-Vallejo, F. & Koper, M. T. M. Spectroscopic Observation of a Hydrogenated CO Dimer Intermediate During CO Reduction on Cu(100) Electrodes. *Angew. Chem. Int. Ed.* **56,** 3621–3624. ISSN: 1521-3773 (2017).

134. Salimon, J, Hernández-Romero, R. & Kalaji, M. The Dynamics of the Conversion of Linear to Bridge Bonded CO on Cu. *J. Electroanal. Chem.* **538-539,** 99–108 (2002).

135. Shaw, S. K., Berná, A., Feliu, J. M., Nichols, R. J., Jacob, T. & Schiffrin, D. J. Role of Axially Coordinated Surface Sites for Electrochemically Controlled Carbon Monoxide Adsorption on Single Crystal Copper Electrodes. *Phys. Chem. Chem. Phys.* **13,** 5242–5251 (12 2011).

136. Wuttig, A., Liu, C., Peng, Q., Yaguchi, M., Hendon, C. H., Motobayashi, K., Ye, S., Osawa, M. & Surendranath, Y. Tracking a Common Surface-Bound Intermediate During CO_2-to-Fuels Catalysis. *ACS Cent. Sci.* **2,** 522–528 (2016).

137. Sheppard, N. & Nguyen, T. T. in *Advances in Infrared and Raman Spectroscopy: v. 5* (eds Clark, R. J. H. & Hester, R. E.) 67–148 (Heyden, 1978). ISBN: 978-0855011857.

138. Hayden, B., Kretzschmar, K. & Bradshaw, A. An Infrared Spectroscopic Study of CO on Cu(111): The Linear, Bridging and Physisorbed Species. *Surf. Sci.* **155,** 553–566 (1985).

139. Hori, Y., Murata, A., Tsukamoto, T., Wakebe, H., Koga, O. & Yamazaki, H. Adsoprtion of Carbon Monoxide at a Copper Electrode Accompanied by Electron Transfer Observed by Voltammetry and IR Spectroscopy. *Electrochim.Acta* **39,** 2495–2500 (1994).

140. Hori, Y., Koga, O., Yamazaki, H. & Matsuo, T. Infrared Spectroscopy of Adsorbed CO and Intermediate Species in Electrochemical Reduction of CO_2 to Hydrocarbons on a Cu Electrode. *Electrochim. Acta* **40,** 2617–2622 (1995).

141. Smith, B. D., Irish, D. E., Kedzierzawski, P. & Augustynski, J. A Surface Enhanced Roman Scattering Study of the Intermediate and Poisoning Species Formed during the Electrochemical Reduction of CO_2 on Copper. *J. Electrochem. Soc.* **144,** 4288–4296 (1997).

142. Koga, O., Teruya, S., Matsuda, K., Minami, M., Hoshi, N. & Hori, Y. Infrared Spectroscopic and Voltammetric Study of Adsorbed CO on Stepped Surfaces of Copper Monocrystalline Electrodes. *Electrochim. Acta* **50,** 2475–2485 (2005).

143. Wang, H.-F., Yan, Y.-G., Huo, S.-J., Cai, W.-B., Xu, Q.-J. & Osawa, M. Seeded Growth Fabrication of Cu-on-Si Electrodes for *in situ* ATR-SEIRAS Applications. *Electrochim. Acta* **52,** 5950–5957 (2007).

144. Heyes, J., Dunwell, M. & Xu, B. CO_2 Reduction on Cu at Low Overpotentials with Surface-Enhanced in Situ Spectroscopy. *J. Phys. Chem. C* **120,** 17334–17341 (2016).

145. Zhu, S., Jiang, B., Cai, W.-B. & Shao, M. Direct Observation on Reaction Intermediates and the Role of Bicarbonate Anions in CO_2 Electrochemical Reduction Reaction on Cu Surfaces. *J. Am. Chem. Soc.* **139,** 15664–15667 (2017).

146. Oda, I., Ogasawara, H. & Ito, M. Carbon Monoxide Adsorption on Copper and Silver Electrodes During Carbon Dioxide Electroreduction Studied by Infrared Reflection Absorption Spectroscopy and Surface-Enhanced Raman Spectroscopy. *Langmuir* **12,** 1094–1097 (1996).

147. Wuttig, A., Liu, C., Peng, Q., Yaguchi, M., Hendon, C. H., Motobayashi, K., Ye, S., Osawa, M. & Surendranath, Y. Tracking a Common Surface-Bound Intermediate During CO_2-to-Fuels Catalysis. *ACS Cent. Sci.* **2,** 522–528 (2016).

148. Hori, Y., Murata, A. & Yoshinami, Y. Adsorption of CO, Intermediately Formed in Electrochemical Reduction of CO_2, at a Copper Electrode. *J. Chem. Soc., Faraday Trans.* **87,** 125–128 (1991).

149. Lobaccaro, P., Singh, M. R., Clark, E. L., Kwon, Y., Bell, A. T. & Ager, J. W. Effects of Temperature and Gas-Liquid Mass Transfer on the Operation of Small Electrochemical Cells for the Quantitative Evaluation of CO_2 Reduction Electrocatalysts. *Phys. Chem. Chem. Phys.* **18,** 26777–26785 (38 2016).

150. Tornquist, W., Guillaume, F. & Griffin, G. L. Vibrational Behavior of Carbon Monxide Adsorbed on Platinum in Nonacidic Electrolytes. *Langmuir* **3,** 477–483 (1987).

151. Cuesta, A. & Gutiérrez, C. Study by Fourier Transform Infrared Spectroscopy of the Adsorption of Carbon Monoxide on a Nickel Electrode at pH 3-14. *Langmuir* **14,** 3397–3404 (1998).

152. Cuesta, A. & Gutiérrez, C. Study by Fourier Transform Infrared Spectroscopy of the Adsorption of Carbon Monoxide on a Cobalt Electrode at pH 3-14. *Langmuir* **14,** 3390–3396 (1998).

153. Couto, A., Rincón, A., Pérez, M. & Gutiérrez, C. Adsorption and Electrooxidation of Carbon Monoxide on Polycrystalline Platinum at pH 0.3-13. *Electrochim. Acta* **46,** 1285–1296 (2001).

154. Yau, S. L., Gao, X., Chang, S. C., Schardt, B. C. & Weaver, M. J. Atomic-Resolution Scanning Tunneling Microscopy and Infrared Spectroscopy as Combined In Situ Probes of Electrochemical Adlayer Structure: Carbon Monoxide on Rhodium (111). *J. Am. Chem. Soc.* **113,** 6049–6056 (1991).

155. Jiang, X. & Weaver, M. J. The Role of Interfacial Potential in Adsorbate Bonding: Electrode Potential-Dependent Infrared Spectra for Saturated CO Adlayers on

Pt(110) and Related Electrochemical Surfaces in Varying Solvent Environments. *Surf. Sci.* **275,** 237–252 (1992).

156. Cuesta, A. & Gutiérrez, C. Study by Fourier Transform Infrared Spectroscopy of the Adsorption of Carbon Monoxide on a Nickel Electrode at pH 3-14. *Langmuir* **14,** 3397–3404 (1998).

157. Cuesta, A. & Gutiérrez, C. Study by Fourier Transform Infrared Spectroscopy of the Adsorption of Carbon Monoxide on a Cobalt Electrode at pH 3-14. *Langmuir* **14,** 3390–3396 (1998).

158. Gileadi, E., Argade, S. D. & Bockris, J. O. The Potential of Zero Charge of Platinum and Its pH Dependence. *J. Phys. Chem.* **70,** 2044–2046 (1966).

159. Broekmann, P., Wilms, M., Spaenig, A. & Wandelt, K. Morphological Aspects of Sulfate-Induced Reconstruction of Cu(111) in Sulfuric Acid Solution: In Situ STM Study. *Prog. Surf. Sci.* **67,** 59–77 (2001).

160. Jović, V. & Jović, B. EIS and Differential Capacitance Measurements onto Single Crystal Faces in Different Solutions: Part II: Cu(111) and Cu(100) in 0.1 M NaOH. *J. Electroanal. Chem.* **541,** 13–21. ISSN: 1572-6657 (2003).

161. Matsushima, H., Taranovskyy, A., Haak, C., Gründer, Y. & Magnussen, O. M. Reconstruction of Cu(100) Electrode Surfaces During Hydrogen Evolution. *J. Am. Chem. Soc.* **131,** 10362–10363 (2009).

162. Matsushima, H., Haak, C., Taranovskyy, A., Gründer, Y. & Magnussen, O. M. In Situ Video STM Studies of the Hydrogen-Induced Reconstruction of Cu(100): Potential and pH Dependence. *Phys. Chem. Chem. Phys.* **12,** 13992–13998 (42 2010).

163. Kim, Y.-G., Javier, A., Baricuatro, J. H., Torelli, D., Cummins, K. D., Tsang, C. F., Hemminger, J. C. & Soriaga, M. P. Surface Reconstruction of Pure-Cu Single-

Crystal Electrodes Under CO-Reduction Potentials in Alkaline Solutions: A Study by Seriatim ECSTM-DEMS. *J. Electroanal. Chem.* **780,** 290–295 (2016).

164. Beverskog, B. & Puigdomenech, I. Revised Pourbaix Diagrams for Copper at 25 to 300°C. *J. Electrochem. Soc.* **144,** 3476–3483 (1997).

165. Eilert, A., Roberts, F. S., Friebel, D. & Nilsson, A. Formation of Copper Catalysts for CO_2 Reduction with High Ethylene/Methane Product Ratio Investigated with In Situ X-ray Absorption Spectroscopy. *J. Phys. Chem. Lett.* **7,** 1466–1470 (2016).

166. Eilert, A., Cavalca, F., Roberts, F. S., Osterwalder, J., Liu, C., Favaro, M., Crumlin, E. J., Ogasawara, H., Friebel, D., Pettersson, L. G. M. & Nilsson, A. Subsurface Oxygen in Oxide-Derived Copper Electrocatalysts for Carbon Dioxide Reduction. *J. Phys. Chem. Lett.* **8,** 285–290 (2017).

167. Lum, Y. & Ager, J. W. Stability of Residual Oxides in Oxide-Derived Copper Catalysts for Electrochemical CO_2 Reduction Investigated with ^{18}O Labeling. *Angew. Chem. Int. Ed.* **57,** 551–554. ISSN: 1521-3773 (2018).

168. Chou, T.-C., Chang, C.-C., Yu, H.-L., Yu, W.-Y., Dong, C.-L., Velasco-Vélez, J.-J., Chuang, C.-H., Chen, L.-C., Lee, J.-F., Chen, J.-M. & Wu, H.-L. Controlling the Oxidation State of the Cu Electrode and Reaction Intermediates for Electrochemical CO_2 Reduction to Ethylene. *J. Am. Chem. Soc.* **142,** 2857–2867 (2020).

169. Kim, Y.-G., Baricuatro, J. H. & Soriaga, M. P. *Electrocatalysis* **9,** 526–530. ISSN: 1868-5994 (July 2018).

170. Rodriguez, P., Garcia-Araez, N., Koverga, A., Frank, S. & Koper, M. T. M. CO Electroxidation on Gold in Alkaline Media: A Combined Electrochemical, Spectroscopic, and DFT Study. *Langmuir* **26,** 12425–12432 (2010).

171. Waszczuk, P., Zelenay, P. & Sobkowski, J. Surface Interaction of Benzoic Acid with a Copper Electrode. *Electrochim. Acta* **40,** 1717–1721 (1995).

172. Li, C. W., Ciston, J. & Kanan, M. W. Electroreduction of Carbon Monoxide to Liquid Fuel on Oxide-Derived Nanocrystalline Copper. *Nature* **508,** 504–507 (2014).

173. Jouny, M., Luc, W. & Jiao, F. High-Rate Electroreduction of Carbon Monoxide to Multi-carbon Products. *Nat. Catal.* **1,** 748–755 (2018).

174. Barton, E. E., Rampulla, D. M. & Bocarsly, A. B. Selective Solar-Driven Reduction of CO_2 to Methanol Using a Catalyzed p-GaP Based Photoelectrochemical Cell. *J. Am. Chem. Soc.* **130,** 6342–6344 (2008).

175. Gong, M., Cao, Z., Liu, W., Nichols, E. M., Smith, P. T., Derrick, J. S., Liu, Y.-S., Liu, J., Wen, X. & Chang, C. J. Supramolecular Porphyrin Cages Assembled at Molecular-Materials Interfaces for Electrocatalytic CO Reduction. *ACS Cent. Sci.* **3,** 1032–1040 (2017).

176. Ahn, S., Klyukin, K., Wakeham, R. J., Rudd, J. A., Lewis, A. R., Alexander, S., Carla, F., Alexandrov, V. & Andreoli, E. Poly-Amide Modified Copper Foam Electrodes for Enhanced Electrochemical Reduction of Carbon Dioxide. *ACS Catal.* **8,** 4132–4142 (2018).

177. Kauffman, D. R., Alfonso, D. R., Tafen, D. N., Wang, C., Zhou, Y., Yu, Y., Lekse, J. W., Deng, X., Espinoza, V., Trindell, J., Ranasingha, O. K., Roy, A., Lee, J.-S. & Xin, H. L. Selective Electrocatalytic Reduction of CO_2 into CO at Small, Thiol-Capped Au/Cu Nanoparticles. *J. Phys. Chem. C* **122,** 27991–28000 (2018).

178. Wang, Z., Wu, L., Sun, K., Chen, T., Jiang, Z., Cheng, T. & Goddard, W. A. Surface Ligand Promotion of Carbon Dioxide Reduction through Stabilizing Chemisorbed Reactive Intermediates. *J. Phys. Chem. Lett.* **9,** 3057–3061 (2018).

179. Iijima, G., Kitagawa, T., Katayama, A., Inomata, T., Yamaguchi, H., Suzuki, K., Hirata, K., Hijikata, Y., Ito, M. & Masuda, H. CO_2 Reduction Promoted by Imida-

zole Supported on a Phosphonium-Type Ionic-Liquid-Modified Au Electrode at a Low Overpotential. *ACS Catal.* **8,** 1990–2000 (2018).

180. Buckley, A. K., Lee, M., Cheng, T., Kazantsev, R. V., Larson, D. M., Goddard III, W. A., Toste, F. D. & Toma, F. M. Electrocatalysis at Organic-Metal Interfaces: Identification of Structure-Reactivity Relationships for CO_2 Reduction at Modified Cu Surfaces. *J. Am. Chem. Soc.* **141,** 7355–7364 (2019).

181. Banerjee, S., Han, X. & Thoi, V. S. Modulating the Electrode-Electrolyte Interface with Cationic Surfactants in Carbon Dioxide Reduction. *ACS Catal.* **9,** 5631–5637 (2019).

182. Wang, J., Zhang, F., Kang, X. & Chen, S. Organic Functionalization of Metal Catalysts: Enhanced Activity Towards Electroreduction of Carbon Dioxide. *Curr. Opin. Electrochem.* **13,** 40 –46. ISSN: 2451-9103 (2019).

183. Nam, D.-H., De Luna, P., Rosas-Hernández, A., Thevenon, A., Li, F., Agapie, T., Peters, J. C., Shekhah, O., Eddaoudi, M. & Sargent, E. H. Molecular enhancement of heterogeneous CO_2 reduction. *Nature Materials* **19,** 266–276. ISSN: 1476-4660 (Mar. 2020).

184. Thevenon, A., Rosas-Hernández, A., Fontani Herreros, A. M., Agapie, T. & Peters, J. C. Dramatic HER Suppression on Ag Electrodes via Molecular Films for Highly Selective CO_2 to CO Reduction. *ACS Catal.* **11,** 4530–4537 (Apr. 2021).

185. Vasilyev, D. V. & Dyson, P. J. The Role of Organic Promoters in the Electroreduction of Carbon Dioxide. *ACS Catal.* **11,** 1392–1405 (Feb. 2021).

186. Schmitt, K. G. & Gewirth, A. A. In Situ Surface-Enhanced Raman Spectroscopy of the Electrochemical Reduction of Carbon Dioxide on Silver with 3,5-Diamino-1,2,4-Triazole. *J. Phys. Chem. C* **118,** 17567–17576 (2014).

187. Larkin, P. J. *Infrared and Raman Spectroscopy; Principles and Spectral Interpretation* (Elsevier, 2011).

188. Hori, Y., Koga, O., Watanabe, Y. & Matsuo, T. FTIR Measurements of Charge Displacement Adsorption of CO on Poly- and Single Crystal (100) of Cu Electrodes. *Electrochim. Acta* **44,** 1389–1395 (1998).

189. Rudolph, W. W., Fischer, D. & Irmer, G. Vibrational Spectroscopic Studies and Density Functional Theory Calculations of Speciation in the CO_2-Water System. *Appl. Spectrosc.* **60,** 130–144 (2006).

190. Baldassarre, M. & Barth, A. The Carbonate/Bicarbonate System as a pH Indicator for Infrared Spectroscopy. *Analyst* **139,** 2167–2176 (Jan. 2014).

191. Dunwell, M., Yang, X., Setzler, B. P., Anibal, J., Yan, Y. & Xu, B. Examination of Near-Electrode Concentration Gradients and Kinetic Impacts on the Electrochemical Reduction of CO_2 using Surface-Enhanced Infrared Spectroscopy. *ACS Catal.* **8,** 3999–4008 (2018).

192. Stancik, A. L. & Brauns, E. B. A Simple Asymmetric Lineshape for Fitting Infrared Absorption Spectra. *Vib. Spectrosc.* **47,** 66–69. ISSN: 0924-2031 (2008).

193. Schouten, K. J. P., Pérez Gallent, E. & Koper, M. T. M. The Influence of pH on the Reduction of CO and CO_2 to Hydrocarbons on Copper Electrodes. *J. Electroanal. Chem.* **716,** 53–57 (2014).

194. Hall, A. S., Yoon, Y., Wuttig, A. & Surendranath, Y. Mesostructure-Induced Selectivity in CO_2 Reduction Catalysis. *J. Am. Chem. Soc.* **137,** 14834–14837 (2015).

195. Ma, M., Djanashvili, K. & Smith, W. A. Controllable Hydrocarbon Formation from the Electrochemical Reduction of CO_2 Over Cu Nanowire Arrays. *Angew. Chem. Int. Ed.* **55,** 6680–6684. ISSN: 1521-3773 (2016).

196. Yoon, Y., Hall, A. S. & Surendranath, Y. Tuning of Silver Catalyst Mesostructure Promotes Selective Carbon Dioxide Conversion into Fuels. *Angew. Chem., Int. Ed.* **55,** 15282–15286 (2016).

197. Schreier, M., Yoon, Y., Jackson, M. N. & Surendranath, Y. Competition between H and CO for Active Sites Governs Copper-Mediated Electrosynthesis of Hydrocarbon Fuels. *Angew. Chem. Int. Ed.* **57,** 10221–10225 (2018).

198. Hollins, P., Davies, K. J. & Pritchard, J. Infrared Spectra of CO Chemisorbed on a Surface Vicinal to Cu(110): The Influence of Defect Sites. *Surf. Sci.* **138,** 75–83. ISSN: 0039-6028 (1984).

199. Borguet, E. & Dai, H.-L. Site-Specific Properties and Dynamical Dipole Coupling of CO Molecules Adsorbed on a Vicinal Cu(100) Surface. *J. Chem. Phys.* **101,** 9080–9095 (1994).

200. Borguet, E. & Dai, H.-L. Probing Surface Short Range Order and Inter-Adsorbate Interactions through IR Vibrational Spectroscopy: CO on Cu(100). *J. Phys. Chem. B* **109,** 8509–8512 (2005).

201. Cheng, T., Xiao, H. & Goddard, W. A. Nature of the Active Sites for CO Reduction on Copper Nanoparticles; Suggestions for Optimizing Performance. *J. Am. Chem. Soc.* **139,** 11642–11645 (2017).

202. Zeghbib, N., Thelliere, P., Rivard, M. & Martens, T. Microwaves and Aqueous Solvents Promote the Reaction of Poorly Nucleophilic Anilines with a Zincke Salt. *J. Org. Chem.* **81,** 3256–3262 (2016).

203. Huang, Y., Handoko, A. D., Hirunsit, P. & Yeo, B. S. Electrochemical Reduction of CO_2 Using Copper Single-Crystal Surfaces: Effects of CO* Coverage on the Selective Formation of Ethylene. *ACS Catal.* **7,** 1749–1756 (2017).

204. Li, J., Wang, Z., McCallum, C., Xu, Y., Li, F., Wang, Y., Gabardo, C. M., Dinh, C.-T., Zhuang, T.-T., Wang, L., Howe, J. Y., Ren, Y., Sargent, E. H. & Sinton, D. Constraining CO Coverage on Copper Promotes High-efficiency Ethylene Electroproduction. *Nat. Catal.* **2,** 1124–1131 (2019).

205. Kuhl, K. P., Hatsukade, T., Cave, E. R., Abram, D. N., Kibsgaard, J. & Jaramillo, T. F. Electrocatalytic Conversion of Carbon Dioxide to Methane and Methanol on Transition Metal Surfaces. *J. Am. Chem. Soc.* **136,** 14107–14113 (2014).

206. Akhade, S. A., Luo, W., Nie, X., Bernstein, N. J., Asthagiri, A. & Janik, M. J. Poisoning Effect of Adsorbed CO During CO_2 Electroreduction on Late Transition Metals. *Phys. Chem. Chem. Phys.* **16,** 20429–20435 (38 2014).

207. Hammer, B., Morikawa, Y & Nørskov, J. K. CO Chemisorption at Metal Surfaces and Overlayers. *Phys. Rev. Lett.* **76,** 2141–2144 (1996).

208. Hori, Y., Kikuchi, K. & Suzuki, S. Production of CO and CH_4 in Electrochemical Reduction of CO_2 at Metal Electrodes in Aqueous Hydrogencarbonate Solution. *Chem. Lett.* **14,** 1695–1698 (1985).

209. Ross, M. B., Dinh, C. T., Li, Y., Kim, D., De Luna, P., Sargent, E. H. & Yang, P. Tunable Cu Enrichment Enables Designer Syngas Electrosynthesis from CO_2. *J. Am. Chem. Soc.* **139,** 9359–9363 (2017).

210. Hoang, T. T. H., Verma, S., Ma, S., Fister, T. T., Timoshenko, J., Frenkel, A. I., Kenis, P. J. A. & Gewirth, A. A. Nanoporous Copper–Silver Alloys by Additive-Controlled Electrodeposition for the Selective Electroreduction of CO_2 to Ethylene and Ethanol. *J. Am. Chem. Soc.* **140,** 5791–5797 (2018).

211. Chen, X., Henckel, D., Nwabara, U., Li, Y., Frenkel, A. I., Fister, T. T., Kenis, P. J. A. & Gewirth, A. A. Controlling Speciation during CO_2 Reduction on Cu-Alloy Electrodes. *ACS Catal.* **10,** 672–682 (2020).

212. Malkani, A. S., Dunwell, M. & Xu, B. Operando Spectroscopic Investigations of Copper and Oxide-Derived Copper Catalysts for Electrochemical CO Reduction. *ACS Catal.* **9,** 474–478 (2019).

213. Jiang, K., Huang, Y., Zeng, G., Toma, F. M., Goddard, W. A. & Bell, A. T. Effects of Surface Roughness on the Electrochemical Reduction of CO_2 over Cu. *ACS Energy Lett.* **5,** 1206–1214 (2020).

214. Mason, S. E., Grinberg, I. & Rappe, A. M. Adsorbate-Adsorbate Interactions and Chemisorption at Different Coverages Studied by Accurate ab initio Calculations: CO on Transition Metal Surfaces. *J. Phys. Chem. B* **110,** 3816–3822 (2006).

215. Garfunkel, E. L., Crowell, J. E. & Somorjai, G. A. The Strong Influence of Potassium on the Adsorption of Carbon Monoxide on Platinum Surfaces: a TDS and HREELS Study. *J. Phys. Chem.* **86,** 310–313 (1982).

216. Rodriguez, J. A. & Campbell, C. T. Quantum Chemical Studies of the Effects of Electron-transferring Ligands Upon Carbon Monoxide Chemisorption on Copper(100). *J. Phys. Chem.* **91,** 2161–2171 (1987).

217. Ovalle, V. J. & Waegele, M. M. Understanding the Impact of N-Arylpyridinium Ions on the Selectivity of CO_2 Reduction at the Cu/Electrolyte Interface. *J. of Phys. Chem. C* **123,** 24453–24460 (2019).

218. Li, F., Thevenon, A., Rosas-Hernandez, A., Wang, Z., Li, Y., Gabardo, C. M., Ozden, A., Dinh, C. T., Li, J., Wang, Y., Edwards, J. P., Xu, Y., McCallum, C., Tao, L., Liang, Z.-Q., Luo, M., Wang, X., Li, H., O'Brien, C. P., Tan, C.-S., Nam, D.-H., Quintero-Bermudez, R., Zhuang, T.-T., Li, Y. C., Han, Z., Britt, R. D., Sinton, D., Agapie, T., Peters, J. C. & Sargent, E. H. Molecular Tuning of CO_2-to-Ethylene Conversion. *Nature* **577,** 509–513 (2019).

219. Koga, O., Watanabe, Y., Tanizaki, M. & Hori, Y. Specific Adsorption of Anions on a Copper (100) Single Crystal Electrode Studied by Charge Displacement by CO Adsorption and Infrared Spectroscopy. *Electrochim. Acta* **46,** 3083 –3090. ISSN: 0013-4686 (2001).

220. Sartin, M. M., Yu, Z., Chen, W., He, F., Sun, Z., Chen, Y.-X. & Huang, W. Effect of Particle Shape and Electrolyte Cation on CO Adsorption to Copper Oxide Nanoparticle Electrocatalysts. *J. Phys. Chem. C* **122,** 26489–26498 (2018).

221. Blizanac, B. B., Lucas, C. A, Gallagher, M. E., Arenz, M., Ross, P. N. & Marković, N. M. Anion Adsorption, CO Oxidation, and Oxygen Reduction Reaction on a Au(100) Surface: The pH Effect. *J. Phys. Chem. B* **108,** 625–634 (2004).

222. Sundararaman, R., Figueiredo, M. C., Koper, M. T. M. & Schwarz, K. A. Electrochemical Capacitance of CO-Terminated Pt(111) Dominated by the CO-Solvent Gap. *J. Phys. Chem. Lett.* **8,** 5344–5348 (2017).

223. Brown, G. & Hope, G. A SERS Study of SO_4^{2-}/Cl^- Ion Adsorption at a Copper Electrode In-Situ. *J. Electroanal. Chem.* **405,** 211 –216. ISSN: 1572-6657 (1996).

224. Niaura, G. & Malinauskas, A. Surface-enhanced Raman Spectroscopy of ClO_4^- and SO_4^{2-} Anions Adsorbed at a Cu Electrode. *J. Chem. Soc., Faraday Trans.* **94,** 2205–2211 (15 1998).

225. Bagger, A., Arán-Ais, R. M., Halldin Stenlid, J., Campos dos Santos, E., Arnarson, L., Degn Jensen, K., Escudero-Escribano, M., Cuenya, B. R. & Rossmeisl, J. Ab Initio Cyclic Voltammetry on Cu (111), Cu (100) and Cu (110) in Acidic, Neutral and Alkaline Solutions. *ChemPhysChem* **20,** 3096–3105 (2019).

226. Conway, B. E. Kinetics of Electrolytic Hydrogen and Deuterium Evolution. *Proc. R. Soc. London, Ser. A* **256,** 128–144 (1960).

227. Łukomska, A. & Sobkowski, J. Potential of Zero Charge of Monocrystalline Copper Electrodes in Perchlorate Solutions. *J. Electroanal. Chem.* **567,** 95–102. ISSN: 1572-6657 (2004).

228. Mills, J. N., McCrum, I. T. & Janik, M. J. Alkali Cation Specific Adsorption onto fcc(111) Transition Metal Electrodes. *Phys. Chem. Chem. Phys.* **16,** 13699–13707 (27 2014).

229. Niaura, G. & Jakubenas, R. The Alkali Metal Cation Effect on the Surface-enhanced Raman Spectra of Phosphate Anions Adsorbed at Silver Electrodes. *J. Electroanal. Chem.* **510,** 50 –58. ISSN: 1572-6657 (2001).

230. Mostany, J., Herrero, E., Feliu, J. M. & Lipkowski, J. Thermodynamic Studies of Anion Adsorption at Stepped Platinum(hkl) Electrode Surfaces in Sulfuric Acid Solutions. *J. Phys. Chem. B* **106,** 12787–12796 (2002).

231. Pérez-Gallent, E., Marcandalli, G., Figueiredo, M. C., Calle-Vallejo, F. & Koper, M. T. M. Structure- and Potential-Dependent Cation Effects on CO Reduction at Copper Single-Crystal Electrodes. *J. Am. Chem. Soc.* **139,** 16412–16419 (2017).

232. Motobayashi, K., Minami, K., Nishi, N., Sakka, T. & Osawa, M. Hysteresis of Potential-Dependent Changes in Ion Density and Structure of an Ionic Liquid on a Gold Electrode: In Situ Observation by Surface-Enhanced Infrared Absorption Spectroscopy. *J. Phys. Chem. Lett.* **4,** 3110–3114 (2013).

233. Shi, C., Hansen, H. A., Lausche, A. C. & Nørskov, J. K. Trends in Electrochemical CO_2 Reduction Activity for Open and Close-Packed Metal Surfaces. *Phys. Chem. Chem. Phys.* **16,** 4720–4727 (2014).

234. Jackman, T. E., Griffiths, K., Davies, J. A. & Norton, P. R. Absolute Coverages and Hysteresis Phenomena Associated with the CO-induced Pt(100) hex$\leftrightarrow$(1$\times$1) Phase Transition. *J. Chem. Phys.* **79,** 3529–3533 (1983).

235. Zou, S., Gomez, R. & Weaver, M. J. Infrared Spectroscopy of Carbon Monoxide at the Ordered Palladium (110)-Aqueous Interface: Evidence for Adsorbate-Induced Surface Reconstruction. *Surf. Sci.* **399,** 270–283 (1998).

236. Bergstroem, P. A., Lindgren, J. & Kristiansson, O. An IR Study of the Hydration of Perchlorate, Nitrate, Iodide, Bromide, Chloride and Sulfate Anions in Aqueous Solution. *J. Phys. Chem.* **95,** 8575–8580 (1991).

237. Kitamura, F., Ohsaka, T. & Tokuda, K. Infrared Spectroscopic Observation of Water at a Polycrystalline Gold Electrode|Aqueous Halide Solution Interface. *J. Electroanal. Chem.* **412,** 183 –188. ISSN: 1572-6657 (1996).

238. Villegas, I. & Weaver, M. J. Infrared Spectroscopy of Model Electrochemical Interfaces in Ultrahigh Vacuum: Evidence for Coupled Cation-Anion Hydration in the Pt(111)/K^+,Cl^- System. *J. Phys. Chem.* **100,** 19502–19511 (1996).

239. Hollins, P. & Pritchard, J. Infrared Studies of Chemisorbed Layers on Single Crystals. *Prog. Surf. Sci.* **19,** 275–349 (1985).

240. Gao, D., Scholten, F. & Cuenya, B. R. Improved CO_2 Electroreduction Performance on Plasma-Activated Cu Catalysts via Electrolyte Design: Halide Effect. *ACS Catal.* **7,** 5112–5120 (2017).

241. McCrum, I. T., Akhade, S. A. & Janik, M. J. Electrochemical Specific Adsorption of Halides on Cu 111, 100, and 211: A Density Functional Theory Study. *Electrochim. Acta* **173,** 302 –309. ISSN: 0013-4686 (2015).

242. Weitzner, S. E., Akhade, S. A., Varley, J. B., Wood, B. C., Otani, M., Baker, S. E. & Duoss, E. B. Toward Engineering of Solution Microenvironments for the CO_2 Reduction Reaction: Unraveling pH and Voltage Effects from a Combined Density-Functional-Continuum Theory. *J. Phys. Chem. Lett.* **11,** 4113–4118 (2020).

243. Li, W. H., Wang, Y., Ye, J. H. & Li, S. F. Y. In Situ STM Study of Chloride Adsorption on Cu(110) Electrode in Hydrochloric Acid Aqueous Solution. *J. Phys. Chem. B* **105,** 1829–1833 (2001).

244. Bae, S.-E. & Gewirth, A. A. In Situ EC-STM Studies of MPS, SPS, and Chloride on Cu(100): Structural Studies of Accelerators for Dual Damascene Electrodeposition. *Langmuir* **22,** 10315–10321 (2006).

245. Keller, H., Saracino, M., Nguyen, H. M., Huynh, T. M. T. & Broekmann, P. Competitive Anion/Water and Cation/Water Interactions at Electrified Copper/Electrolyte Interfaces Probed by in Situ X-ray Diffraction. *J. Phys. Chem. C* **116,** 11068–11076 (2012).

246. Iijima, G., Inomata, T., Yamaguchi, H., Ito, M. & Masuda, H. Role of a Hydroxide Layer on Cu Electrodes in Electrochemical CO_2 Reduction. *ACS Catal.* **9,** 6305–6319 (2019).

247. Zhao, Y., Chang, X., Malkani, A. S., Yang, X., Thompson, L., Jiao, F. & Xu, B. Speciation of Cu Surfaces During the Electrochemical CO Reduction Reaction. *J. Am. Chem. Soc.* **142,** 9735–9743 (2020).

248. Herasymenko, P. & Šlendyk, I. Wasserstoffüberspannung und Adsorption der Ionen. *Z. Phys. Chem. A* **149,** 123–139 (1930).

249. Frumkin, A. N. Influence of Cation Adsorption on the Kinetics of Electrode Processes. *Trans. Faraday Soc.* **55,** 156–167 (0 1959).

250. Yang, X., Wang, Y., Li, C. M. & Wang, D. Mechanisms of Water Oxidation on Heterogeneous Catalyst Surfaces. *Nano Res.* **14,** 3446–3457. ISSN: 1998-0000 (Oct. 2021).

251. Rosca, V., Duca, M., de Groot, M. T. & Koper, M. T. M. Nitrogen Cycle Electrocatalysis. *Chem. Rev.* **109,** 2209–2244 (2009).

252. McEnaney, J. M., Blair, S. J., Nielander, A. C., Schwalbe, J. A., Koshy, D. M., Cargnello, M. & Jaramillo, T. F. Electrolyte Engineering for Efficient Electrochemical Nitrate Reduction to Ammonia on a Titanium Electrode. *ACS Sustain. Chem. Eng.* **8,** 2672–2681 (Feb. 2020).

253. Thorson, M. R., Siil, K. I. & Kenis, P. J. A. Effect of Cations on the Electrochemical Conversion of CO_2 to CO. *J. Electrochem. Soc.* **160,** F69–F74 (2012).

254. Arán-Ais, R. M., Gao, D. & Roldan Cuenya, B. Structure- and Electrolyte-Sensitivity in CO_2 Electroreduction. *Acc. Chem. Res.* **51,** 2906–2917 (2018).

255. Li, J., Chang, X., Zhang, H., Malkani, A. S., Cheng, M.-j., Xu, B. & Lu, Q. Electrokinetic and In Situ Spectroscopic Investigations of CO Electrochemical Reduction on Copper. *Nat. Commun.* **12,** 3264. ISSN: 2041-1723 (June 2021).

256. Rao, R. R., Huang, B., Katayama, Y., Hwang, J., Kawaguchi, T., Lunger, J. R., Peng, J., Zhang, Y., Morinaga, A., Zhou, H., You, H. & Shao-Horn, Y. pH- and Cation-Dependent Water Oxidation on Rutile RuO_2(110). *J. Phys. Chem. C* **125,** 8195–8207. ISSN: 1932-7447 (Apr. 2021).

257. Resasco, J., Chen, L. D., Clark, E., Tsai, C., Hahn, C., Jaramillo, T. F., Chan, K. & Bell, A. T. Promoter Effects of Alkali Metal Cations on the Electrochemical Reduction of Carbon Dioxide. *J. Am. Chem. Soc.* **139,** 11277–11287 (2017).

258. Zhu, Q., Wallentine, S., Deng, G. & Baker, L. R. Solvation-Induced Onsager Reaction Field Rather than Double Layer Field Controls CO_2 Reduction on Gold. *ChemRxiv,* 10.26434/chemrxiv.14410655.v2 (2021).

259. Liu, H., Liu, J. & Yang, B. Promotional Role of a Cation Intermediate Complex in C_2 Formation from Electrochemical Reduction of CO_2 over Cu. *ACS Catal.* **11,** 12336–12343 (Oct. 2021).

260. Fink, A. G., Lees, E. W., Zhang, Z., Ren, S., Delima, R. S. & Berlinguette, C. P. Impact of Alkali Cation Identity on the Conversion of HCO_3^- to CO in Bicarbonate Electrolyzers. *ChemElectroChem* **8,** 2094–2100. ISSN: 2196-0216 (June 2021).

261. Strmcnik, D., Kodama, K., van der Vliet, D., Greeley, J., Stamenkovic, V. R. & Marković, N. M. The Role of Non-Covalent Interactions in Electrocatalytic Fuel-Cell Reactions on Platinum. *Nat. Chem.* **1,** 466–472 (2009).

262. Hussain, G., Pérez-Martínez, L., Le, J.-B., Papasizza, M., Cabello, G., Cheng, J. & Cuesta, A. How Cations Determine the Interfacial Potential Profile: Relevance for the CO_2 Reduction Reaction. *Electrochim. Acta* **327,** 135055. ISSN: 0013-4686 (Dec. 2019).

263. Wallentine, S., Bandaranayake, S., Biswas, S. & Baker, L. R. Direct Observation of Carbon Dioxide Electroreduction on Gold: Site Blocking by the Stern Layer Controls CO_2 Adsorption Kinetics. *J. Phys. Chem. Lett.* **11,** 8307–8313 (Oct. 2020).

264. Frank, D. G., Katekaru, J. Y., Rosasco, S. D., Salaita, G. N., Schardt, B. C., Soriaga, M. P., Stern, D. A., Stickney, J. L. & Hubbard, A. T. pH and Potential Dependence of the Electrical Double Layer at Well-Defined Electrode Surfaces: Cs^+ and Ca^{2+} Ions at Pt(111) $(2\sqrt{3} \times 2\sqrt{3})$R30°-CN, Pt(111) $(\sqrt{13} \times \sqrt{13})$R14°-CN, and Pt(111) (2×2)-SCN. *Langmuir* **1,** 587–592 (1985).

265. Salaita, G. N., Stern, D. A., Lu, F., Baltruschat, H., Schardt, B. C., Stickney, J. L., Soriaga, M. P., Frank, D. G. & Hubbard, A. T. Structure and Composition of a Platinum(111) Surface as a Function of pH and Electrode Potential in Aqueous Bromide Solutions. *Langmuir* **2,** 828–835 (1986).

266. Pennathur, A. K., Voegtle, M. J., Menachekanian, S. & Dawlaty, J. M. Strong Propensity of Ionic Liquids in Their Aqueous Solutions for an Organic-Modified Metal Surface. *J. Phys. Chem. C* **124,** 7500–7507. ISSN: 1520-6106 (Aug. 2020).

267. Voegtle, M. J., Pal, T., Pennathur, A. K., Menachekanian, S., Patrow, J. G., Sarkar, S., Cui, Q. & Dawlaty, J. M. Interfacial Polarization and Ionic Structure at the Ionic Liquid–Metal Interface Studied by Vibrational Spectroscopy and Molecular Dynamics Simulations. *J. Phys. Chem. C* **125,** 2741–2753. ISSN: 1520-6106 (Mar. 2021).

268. Harmon, K. M., Gennick, I. & Madeira, S. L. Hydrogen Bonding. IV. Correlation of Infrared Spectral Properties with C-H· · ·X Hydrogen Bonding and Crystal Habit in Tetramethylammonium Ion Salts. *J. Phys. Chem.* **78,** 2585–2591. ISSN: 0022-3654 (Dec. 1974).

269. McCrum, I. T., Hickner, M. A. & Janik, M. J. Quaternary Ammonium Cation Specific Adsorption on Platinum Electrodes: A Combined Experimental and Density Functional Theory Study. *J. Electrochem. Soc.* **165,** F114–F121 (2018).

270. Sorenson, S. A., Patrow, J. G. & Dawlaty, J. M. Solvation Reaction Field at the Interface Measured by Vibrational Sum Frequency Generation Spectroscopy. *J. Am. Chem. Soc.* **139,** 2369–2378 (2017).

271. He, F., Chen, W., Zhu, B.-Q., Zhen, E.-f., Cai, J. & Chen, Y.-X. Stability of Quaternary Akyl Ammonium Cations during the Hydrogen Evolution Reduction: A Differential Electrochemical Mass Spectrometry Study. *J. Phys. Chem. C* **125,** 5715–5722. ISSN: 1932-7447 (Mar. 2021).

272. Deng, Z. & Irish, D. E. Potential Dependence of the Orientation of $(CH_3)_4N^+$ Adsorbed on a Silver Electrode. A SERS Investigation. *J. Phys. Chem.* **98,** 9371–9373. ISSN: 0022-3654 (Sept. 1994).

273. Trasatti, S. & Lust, E. (eds White, R. E., Bockris, J. O. & Conway, B. E.) 78 (KluwerAcademic/PlenumPublishers, New York, 1999).

274. Marcus, Y. *Ion Properties; Marcel Dekker, Inc.; New York, NY* (1997).

275. Dong, Q., Zhang, X., He, D., Lang, C. & Wang, D. Role of H_2O in CO_2 Electrochemical Reduction As Studied in a Water-in-Salt System. *ACS Cent. Sci.* **5,** 1461–1467. ISSN: 2374-7943 (Aug. 2019).

276. Zhang, B. A., Ozel, T., Elias, J. S., Costentin, C. & Nocera, D. G. Interplay of Homogeneous Reactions, Mass Transport, and Kinetics in Determining Selectivity of the Reduction of CO_2 on Gold Electrodes. *ACS Cent. Sci.* **5,** 1097–1105. ISSN: 2374-7943 (June 2019).

277. Gambarotta, S., Arena, F., Floriani, C. & Zanazzi, P. F. Carbon Dioxide Fixation: Bifunctional Complexes Containing Acidic and Basic Sites Working As Reversible Carriers. *J. Am. Chem. Soc.* **104,** 5082–5092. ISSN: 0002-7863 (Sept. 1982).

278. Benn, E. E., Gaskey, B. & Erlebacher, J. D. Suppression of Hydrogen Evolution by Oxygen Reduction in Nanoporous Electrocatalysts. *J. Am. Chem. Soc.* **139,** 3663–3668. ISSN: 0002-7863 (Mar. 2017).

279. Chen, W., Liao, L. W., Cai, J., Chen, Y.-X. & Stimming, U. Unraveling Complex Electrode Processes by Differential Electrochemical Mass Spectrometry and the Rotating Ring-Disk Electrode Technique. *J. Phys. Chem. C* **123,** 29630–29637. ISSN: 1932-7447 (Dec. 2019).

280. Bondue, C. J., Graf, M., Goyal, A. & Koper, M. T. M. Suppression of Hydrogen Evolution in Acidic Electrolytes by Electrochemical CO_2 Reduction. *J. Am. Chem. Soc.* **143,** 279–285. ISSN: 0002-7863 (Jan. 2021).

281. Wuttig, A. & Surendranath, Y. Impurity Ion Complexation Enhances Carbon Dioxide Reduction Catalysis. *ACS Catal.* **5,** 4479–4484 (2015).

282. Shang, H., Wallentine, S. K., Hofmann, D. M., Zhu, Q., Murphy, C. J. & Baker, L. R. Effect of Surface Ligands on Gold Nanocatalysts for CO_2 Reduction. *Chem. Sci.* **11,** 12298–12306 (45 2020).

283. Dunwell, M., Yang, X., Yan, Y. & Xu, B. Potential Routes and Mitigation Strategies for Contamination in Interfacial Specific Infrared Spectroelectrochemical Studies. *J. Phys. Chem. C* **122,** 24658–24664. ISSN: 1932-7447 (Nov. 2018).

284. Cave, E. R., Montoya, J. H., Kuhl, K. P., Abram, D. N., Hatsukade, T., Shi, C., Hahn, C., Nørskov, J. K. & Jaramillo, T. F. Electrochemical CO_2 Reduction on Au Surfaces: Mechanistic Aspects Regarding the Formation of Major and Minor Products. *Phys. Chem. Chem. Phys.* **19,** 15856–15863 (24 2017).

285. Neubrech, F., Huck, C., Weber, K., Pucci, A. & Giessen, H. Surface-Enhanced Infrared Spectroscopy Using Resonant Nanoantennas. *Chem. Rev.* **117,** 5110–5145 (2017).

286. Ripatti, D. S., Veltman, T. R. & Kanan, M. W. Carbon Monoxide Gas Diffusion Electrolysis that Produces Concentrated C_2 Products with High Single-Pass Conversion. *Joule* **3,** 240–256. ISSN: 2542-4351 (2019).

287. Erick, H. J., Fengwang, L., Adnan, O., Armin, S. R., de Arquer, F. P. G., Shijie, L., Shuzhen, Z., Mingchuan, L., Xue, W., Yanwei, L., Yi, X., Koen, B., Kai, M. R., Cao-Thang, D., David, S. & H., S. E. CO_2 electrolysis to multicarbon products in strong acid. *Science* **372,** 1074–1078 (June 2021).

288. Monteiro, M. C. O., Philips, M. F., Schouten, K. J. P. & Koper, M. T. M. Efficiency and selectivity of CO_2 reduction to CO on gold gas diffusion electrodes in acidic media. *Nat. Commun.* **12,** 4943. ISSN: 2041-1723 (Aug. 2021).

289. Burdyny, T. & Smith, W. A. CO_2 reduction on gas-diffusion electrodes and why catalytic performance must be assessed at commercially-relevant conditions. *Energy Environ. Sci* **12,** 1442–1453. ISSN: 1754-5692 (2019).

290. Higgins, D., Hahn, C., Xiang, C., Jaramillo, T. F. & Weber, A. Z. Gas-Diffusion Electrodes for Carbon Dioxide Reduction: A New Paradigm. *ACS Energy Lett.* **4,** 317–324 (Jan. 2019).

291. Lu, X., Zhu, C., Wu, Z., Xuan, J., Francisco, J. S. & Wang, H. In Situ Observation of the pH Gradient near the Gas Diffusion Electrode of CO2 Reduction in Alkaline Electrolyte. *J. Am. Chem. Soc.* **142,** 15438–15444. ISSN: 0002-7863 (Sept. 2020).

292. Nesbitt, N. T. & Smith, W. A. Operando Topography and Mechanical Property Mapping of CO2 Reduction Gas-Diffusion Electrodes Operating at High Current Densities. *J. Electrochem. Soc.* **168,** 044505. ISSN: 0013-4651 (Apr. 2021).

293. Blaudez, D., Turlet, J.-M., Dufourcq, J., Bard, D., Buffeteau, T. & Desbat, B. Investigations at the air/water interface using polarization modulation IR spectroscopy. *Journal of the Chemical Society, Faraday Transactions* **92,** 525–530. ISSN: 0956-5000 (1996).